

**Quantum Simulations for Semiconductor
Quantum Dots:
From Artificial Atoms to Wigner Molecules**

I n a u g u r a l - D i s s e r t a t i o n

zur
Erlangung des Doktorgrades der
Mathematisch-Naturwissenschaftlichen Fakultät
der Heinrich-Heine-Universität Düsseldorf

vorgelegt von
Boris Reusch
aus Wiesbaden

Düsseldorf
im März 2003

Referent: Prof. Dr. Reinhold Egger
Korreferent: Prof. Dr. Hartmut Löwen

Tag der mündlichen Prüfung: 21.05.2003

Gedruckt mit der Genehmigung der Mathematisch-Naturwissenschaftlichen
Fakultät der Heinrich-Heine-Universität Düsseldorf

Contents

1	Introduction	1
2	Few-electron quantum dots	5
2.1	The single-electron transistor	6
2.2	Coulomb blockade and capacitance	7
2.3	Model Hamiltonian	10
2.4	Non-interacting eigenstates and shell filling	12
2.5	Hund's rule and ground-state spin	13
2.6	Brueckner parameter r_s	14
2.7	Strongly interacting limit: Wigner molecule	14
2.8	Classical electrons	15
2.9	Impurity	17
2.10	Temperature and thermal melting	18
2.11	Few-electron artificial atoms	19
2.12	Single-electron capacitance spectroscopy	21
2.13	Bunching of addition energies	22
2.14	Theoretical approaches for the bunching phenomenon	24
2.15	Open questions addressed in this thesis	26
3	Path-integral Monte Carlo simulation	27
3.1	Path-integral Monte Carlo	28
3.1.1	Monte Carlo method	28
3.1.2	Markov chain and Metropolis algorithm	29
3.1.3	Discretized path integral	30
3.1.4	Trotter break-up and short-time propagator	31
3.1.5	Path-integral ring polymer	33
3.1.6	Monte Carlo observables	34
3.1.7	Spin contamination	36
3.1.8	Fermionic sign problem	37
3.1.9	Monte Carlo error bars	40
3.2	Tests for the PIMC simulation	43
3.2.1	Isotropic clean quantum-dot Helium	43

3.2.2	Finite temperature, zero interaction	44
3.2.3	Finite temperature, non-zero interaction	45
3.3	Trotter convergence	47
3.3.1	Trotter convergence for clean quantum-dot Helium	47
3.3.2	Trotter convergence for $N = 2$ with impurity	49
3.3.3	Trotter convergence for higher electron numbers	50
3.3.4	Convergence for other quantities	52
3.3.5	General procedure	54
3.4	PIMC study for a quantum dot with a single attractive impurity . . .	55
3.4.1	Ground-state energies and spins	55
3.4.2	Charge and spin densities	60
3.4.3	Impurity susceptibility - finite-size Kondo effect?	68
3.5	Conclusion	69
4	Unrestricted Hartree-Fock for quantum dots	73
4.1	Unrestricted Hartree-Fock method	74
4.1.1	Hartree-Fock Slater determinant	74
4.1.2	Hartree-Fock orbitals	75
4.1.3	Breaking of rotational symmetry	75
4.1.4	Numerical procedure	76
4.1.5	Orientational degeneracy	77
4.2	Unrestricted Hartree-Fock for quantum-dot Helium	78
4.2.1	Two-electron Slater determinant	78
4.2.2	Different HF approximations	78
4.2.3	UHF one-particle densities	80
4.2.4	UHF orbitals	82
4.2.5	UHF two-particle densities	85
4.3	Unrestricted Hartree-Fock for higher electron numbers	86
4.3.1	UHF energies	87
4.3.2	HF densities: Even-odd effect	90
4.3.3	Closer look at three electrons	92
4.3.4	Lattice Hamiltonian and localized orbitals	94
4.3.5	Geometric crossover for six electrons	97
4.3.6	Seven- and eight-electron Wigner molecules	98
4.4	Unrestricted Hartree-Fock with a magnetic field	100
4.4.1	Quantum dot energies with magnetic field	100
4.4.2	UHF densities with magnetic field	102
4.4.3	Relation to other results	103
4.5	Conclusion	105
5	Conclusions	107
	Bibliography	111

1 Introduction

The physics of a few or many identical quantum particles is a fascinating and challenging subject. The interplay of interactions and (anti-)symmetry leads to many unexpected effects. However, the theoretical description of complex systems is difficult. Whereas the one- or two-particle problem can be addressed analytically, for more than two particles, the treatment, i.e. trying to solve the Schrödinger equation for a realistic model, mostly has to be numerical. Here, we have to differentiate: exact methods are often computationally very expensive and their results might be hard to interpret. Approximate methods can be suggestive but also misleading. Their validity has to be checked by comparing them to exact results.

On the other hand, in the experiment there is usually a large number of particles and it is difficult to isolate controllably a system which consists of a few particles. In the last fifteen years progress in semiconductor microfabrication has made it possible to confine a very small number of electrons in so-called nanostructures, e.g. quantum wells or quantum wires. Modern technology allows for defining clean structures with exact confinement which is often reduced in dimensionality. This means that electrons are moving freely only in one or two dimensions. When the confinement is strong in all three spatial dimensions we speak of zero-dimensional systems or *quantum dots*.

These finite electron systems have a lot in common with atoms where the confinement is given by the strong attractive potential of the nucleus. Yet for quantum dots one cannot only control the electron number, but also engineer their shape and, by doping the host material and tiny gate electrodes, their electronic density. This is why quantum dots are also called *artificial atoms*. In real atoms the density is very high, and the effect of the mutual Coulomb repulsion of electrons is rather small against the attractive force from the nucleus. In contrast, the electronic density in quantum dots can be much lower. While electrons are on average further apart from each other, the electron-electron interaction becomes more important in comparison to the confinement strength.

In quantum dots one can thus tune the Coulomb repulsion of a few confined electrons. This makes them very interesting physical systems because they allow us to study correlation effects which cannot be addressed in a controlled way in other physical systems.

In this thesis we investigate a model of interacting electrons which are restricted to move only in two dimensions. Furthermore, they are trapped by a harmonic potential $V \propto r^2$. We illustrate this simple but realistic model for two limiting cases in Fig. 1.1.

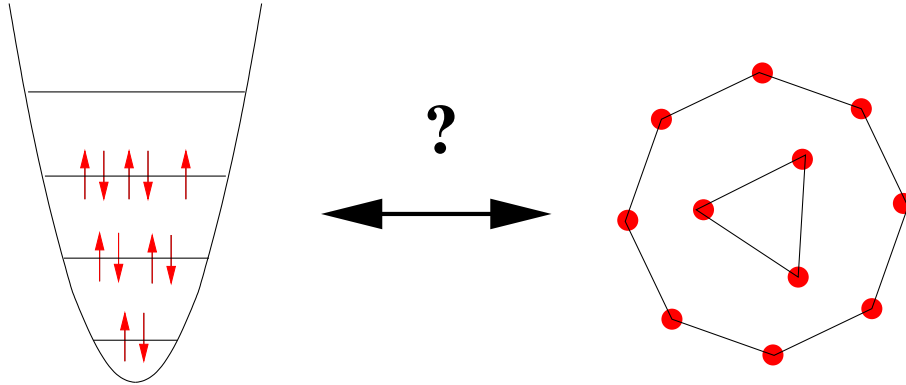


Fig. 1.1: Two-dimensional electrons in an isotropic parabolic potential. For vanishing Coulomb interaction the energetic shells of the harmonic oscillator are filled. Strongly interacting electrons form a small crystal, a so-called Wigner molecule, to minimize their mutual repulsion. In the present thesis we study the crossover between these two pictures.

The left hand side illustrates the situation for negligible interaction (strong confinement). The electrons are filled into the oscillator states according to the degeneracy of the 2D oscillator. Each *orbital* can be occupied with spin up and down. This leads to an energetic shell filling, with open and closed shells. For a small interaction one finds the lifting of some degeneracies and Hund's rule in analogy to conventional atomic physics. Therefore this electron system can be regarded as an *artificial atom* where the external parabolic potential mimics the attraction of the nucleus.

The right hand side depicts the regime of very small density (weak confinement). The electrons have negligible kinetic energy and are strongly correlated due to their mutual Coulomb repulsion. In order to minimize this repulsion they arrange themselves on shells in real space. This small regular structure is called a *Wigner molecule* because it is the finite size counterpart to the infinite 2D Wigner crystal (WIGNER, 1934).

Note that in the first case we have used a one-particle picture, namely electrons occupying orbitals. This description is intimately related to the Hartree-Fock (HF) method. Here, one approximates the full wave function by a single Slater determinant of self-consistent orbitals. HF is a traditional method of atomic and nuclear physics. The application of the symmetry-breaking unrestricted version of HF to quantum dots is one of the main subjects of this thesis. Breaking a symmetry implies that correlations are partly taken into account. In this work, we investigate the validity of HF when we increase the interaction and thereby move towards the picture on the right.

In this second case, we are led to think of electrons as being classical point charges. This is only correct in the limit of infinitely strong interaction. The full quantum-mechanical treatment of the crossover between the two limiting cases is much more difficult. The correct description by a wave function has to include many Slater

determinants and respect the symmetries of the system. The second main method employed in this thesis is to calculate not complete wave functions, but expectation values of physical observables using path-integral Monte Carlo. This numerical method is essentially exact and can reliably describe the full crossover between both regimes.

The previous discussion was rather from the theorist's point of view. We have explained our model of a quantum dot and the mathematical description of the isolated N -electron system. Now, we want to relate the physics of quantum dots to a broader context. For both theorists and experimentalists the relative isolation of the quantum dot from the external world is a very important feature. However, in order to take measurements, one has to contact the dot, for example to measure the energy required to add one electron to it. This corresponds to determining the electron affinity or the ionization energy for real atoms. In so-called transport experiments one measures the conductance for a current through the quantum dot.

This leads to questions like the following (THOULESS, 1977): what happens to a conductor when its size and dimensions are made smaller and smaller? When a metallic wire is made thinner until it finally reaches the limit of a few atoms the situation is similar to the transport process through a quantum dot. This question is not at all purely academic when we think of the immense progress in microelectronics. Computer chips are getting faster and faster because one can integrate more, tinier transistors on a chip. When the size of a transistor reaches the point that quantum effects play a role (e.g. charge and energy quantization), we are in a new regime which is called *mesoscopic* physics. It is a relatively new field in physics, only about 20 years old, and is situated somewhere between the macroscopic every day world and the microscopic world of single atoms or molecules. In mesoscopic systems, the Fermi wavelength is comparable to the dimension of the device. In addition, disorder effects can play an important role. A quantum dot can be viewed as the prototype of a very small transistor: it comprises still many hundreds or thousands of atoms but can act as a single large atom with electronic properties that differ strongly from a normal transistor.

Quantum dots as confined few- or many-particle quantum systems have various interesting analogues in physics. Historically viewed, before the advent of quantum mechanics and the atomic model of Bohr and Rutherford, the English physicist J.J. THOMSON (1904) proposed his plum-pudding model, where (classical) electrons move in the homogeneous positive background charge which is distributed all over the atom. This results in a three-dimensional harmonic confinement and explains why artificial atoms are also called *Thomson atoms*. In real atoms the strong Coulomb potential of the point-like nucleus gives rise to the shell structure of the periodic table of elements. Also for atomic nuclei a shell structure has been found with magic numbers of nucleons for very stable configurations. Clusters are systems of a few to a few thousand atoms that have quite different properties with respect to the bulk and the single atom. Clusters of Alkali atoms can be properly described within the

jellium model which is nothing else than a quantum-mechanical version of the Thomson atom. A more classical example of a confined system are ions in Paul traps for which crystallization at low temperatures has been shown. Finally, a very quantum-mechanical example is the Bose-Einstein condensation of weakly interacting neutral atoms in magneto-optical traps.

In this thesis we investigate a quantum dot as a model of interacting two-dimensional electrons in a harmonic potential. We perform calculations with two methods: exact path-integral Monte Carlo (PIMC) and unrestricted Hartree-Fock (UHF). This work consists of three main parts.

In the first part we give an introduction to the field of few-electron quantum dots and present our model Hamiltonian. We explain the experiments that we want to describe with our simulations: while atomlike properties have been probed in very small dots, signatures of Wigner crystallization have been found in larger dots, so the Wigner molecule is in reach of current technology. It is the purpose of this work to understand better the nature of this crossover from weak to strong correlations.

The second part exposes a comprehensive PIMC study. We explain the method, our implementation, and various checks that we carry out in order to improve the understanding and assess the accuracy of the method. We then perform PIMC simulations for the most difficult, yet most interesting regime of the beginning Wigner-molecule formation. This intermediate regime is not yet completely understood. In these calculations we also include an impurity which deforms the quantum dot and models the influence of disorder in quantum dots. We want to obtain results for ground-state energies and see if the ground-state spin deviates from the expected Hund's rule scheme. Further, we address the question if magic numbers of enhanced stability persist in presence of stronger interaction and deviations from the ideal rotationally symmetric potential. We will quantify the degree of crystallization and correlation by calculating the distributions of electron charge and spin. Another interesting point concerns the formation of a local magnetic moment at the impurity and its effect on the spin structure of the quantum dot.

In the third part we present extensive UHF calculations for clean quantum dots. We briefly recall the method and our numerical implementation. We study the full crossover from weak to strong interaction for zero and small magnetic field. We will elucidate the mechanism of the symmetry-breaking UHF mean field and how far it renders correctly the onset of Wigner crystallization. Fortunately, we can compare our results to exact PIMC data and thereby assert the reliability of the UHF method. Finally, it is an interesting question what happens to the concept of orbitals in the strongly interacting limit. We will look for signatures of the Wigner molecule in the UHF single-particle energies and show the connection between the continuous model and a simple lattice Hamiltonian.

2 Few-electron quantum dots

Quantum dots are low-dimensional nanometer-sized man-made systems where a few or up to several thousands electrons are confined (JACAK ET AL., 1998). Usually they are fabricated by restricting the two-dimensional (2D) electron gas in a semiconductor heterostructure laterally by tiny electrostatic gates or vertically by etching techniques. One can control the confinement, the electron number and thus the density and the interaction strength.

In this chapter we want to give a brief introduction to the field of few-electron quantum dots and motivate our calculations. We start historically with the experiments on very small field-effect transistors which demonstrated nearly equidistant conductance peaks. We explain these peaks with the simplest model of the so-called Coulomb blockade which relies on the quantization of charge.

Then we introduce the Hamiltonian of a quantum dot as a system of interacting 2D electrons in a parabolic potential. The calculations in the present thesis start from this model system. We go on by describing two groups of experiments more specifically: First the experiments of TARUCHA ET AL. (1996) and KOUWENHOVEN ET AL. (2001) who performed measurements on very small dots with only a few electrons starting from zero. They found a shell structure in the Coulomb blockade peaks which shows the importance of energy quantization. Second we illustrate the experiments of ASHOORI (1996) and co-workers: Their experiments were done with larger, more disordered dots where the interaction has a more important role. Surprisingly, they found that Coulomb peaks can coincide, which appears to be a violation of Coulomb blockade.

Our calculations model this experimental situation and we specify what interesting physics we want to address with this work. In the present thesis we adopt a rather microscopic perspective on the behavior of a few interacting confined 2D electrons. We do not explicitly consider the contacts and the tunneling of electrons into the quantum dot. For stronger coupling this tunneling can give rise to the Kondo effect in quantum dots (KOUWENHOVEN and GLAZMAN, 2001). We also do not consider the statistical theory of quantum dots like quantum chaos or statistical mesoscopic physics (ALHASSID, 2000). These theories are rather for larger dots with stronger disorder. Finally we can also only briefly mention here the important research on optical studies of quantum dots that are expected to form the basis of a new generation of lasers (see e.g. GAMMON and STEEL, 2002) or even the basic elements of quantum computing (e.g. LOSS and DIVINCENZO, 1998). For an overview of Thomson atoms, see VORRATH and BLÜMEL (2000).

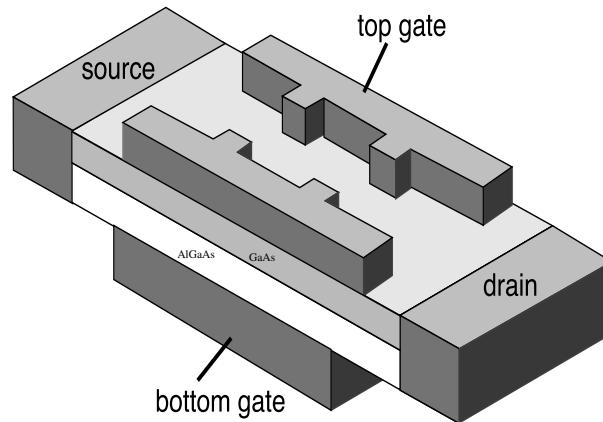


Fig. 2.1: Single-electron transistor (lateral quantum dot) as built by MEIRAV ET AL. (1991). In the GaAs, close to the interface to the insulating AlGaAs, electrons form a 2DEG whose density can be tuned by the positive bottom gate. The electrons are laterally confined by the nano-structured negatively charged top gate which forms a small channel with width of about $0.5\mu\text{m}$ and length $\sim 1\mu\text{m}$ between the two constrictions.

2.1 The single-electron transistor

The discovery of quantum dots took place when experimentalists measured the conductance through very small semiconductor field-effect transistors (KASTNER, 1992). In Fig. 2.1 we show schematically such a device based on GaAs (semiconducting) and AlGaAs (insulating). The active region of the transistor is a two-dimensional electron gas (2DEG): At the interface of AlGaAs/GaAs there is a strong electric field so that electrons are confined in that plane. When a positive voltage is applied to the bottom gate, more and more electrons accumulate. One can therefore tune the density of the 2DEG¹. By application of a negative voltage, electrons are repelled from under the tiny lithographically patterned top gate. In Fig. 2.2 we show the corresponding potential that the 2D electrons are subjected to. There are two strong tunnel barriers due to the constriction in the top gate. The small lake of electrons in the middle forms the quantum dot, their confinement in the plane can be approximated as parabolic. Excitations in this plane have energies about a few meV, therefore the experiments require very low temperature. The Fermi level of the lake can be tuned by the bottom gate voltage. One can measure the conductance through the dot by applying a small voltage between source and drain. A conventional transistor turns on only once, when the gate voltage is raised. Here, the experimentalists found nearly periodic peaks in the conductance when they increased the bottom gate

¹The 2DEG has also become quite famous because in similar devices, for a very strong magnetic field, the integer and fractional Quantum Hall effect have been discovered.

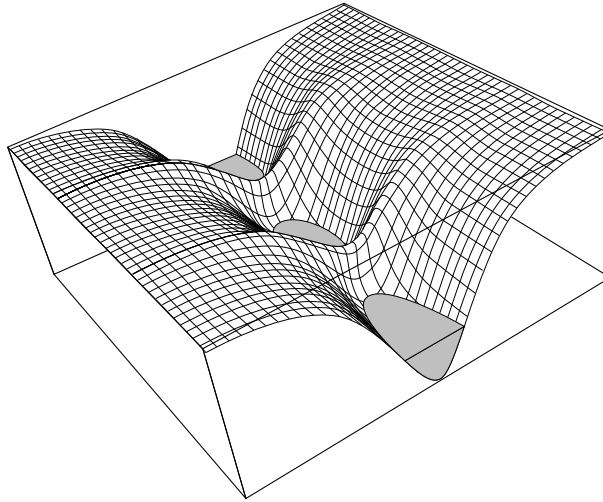


Fig. 2.2: Potential landscape that the 2D electrons feel in the device of Fig. 2.1. The level of the lake can be controlled by the positive bottom gate voltage and the height of the barriers by the negative top gate. The central small lake is the quantum dot, also called 'controlled-barrier atom' (KASTNER, 1993).

voltage (Fig. 2.3). As we will now explain, the transistor turns on and off again every time a single electron is added to it.

2.2 Coulomb blockade and capacitance

The phenomenon of the periodic conductance peaks is known as Coulomb blockade oscillations and it is due to the quantization of charge. A similar behavior was known before for the tunnel conductance through a small metallic particle embedded in an insulator. As shown in Fig. 2.4, such a small metallic Coulomb island can also be viewed as a quantum dot but contains $\sim 10^7$ electrons². The mesoscopic particle is very well isolated by the tunnel barriers and thus the electron number on it is well defined. The tunneling of one extra electron on the island is energetically costly because of the Coulomb repulsion of all electrons on it. One can define a capacitance C for the particle which depends on its dimensions and the geometry with respect to the leads. The level spectrum of the metal particle is almost continuous. Adding one electron to the dot requires an energy $e^2/2C$ above the Fermi energy μ_f and adding a hole requires an energy $e^2/2C$ below μ_f . This results in a gap of width e^2/C in the tunneling density of states.

²The controlled-barrier atom in Fig. 2.1 contains about 30-60 electrons. Naturally, by this we mean the free electrons, not bound to the ion cores. Only recently, experimentalists succeeded in completely emptying a lateral dot defined in a 2DEG (CIORGA ET AL., 2000). We will later show more examples of quantum dots which just contain very few electrons.

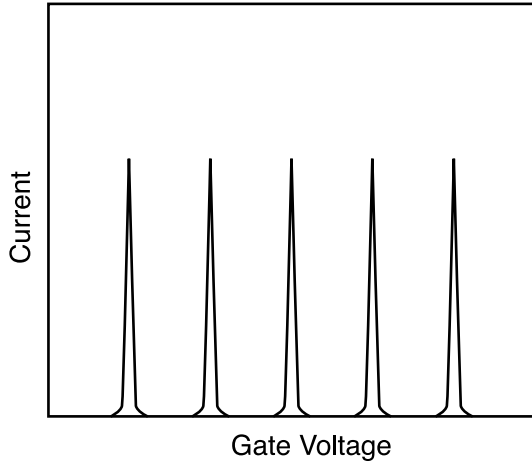


Fig. 2.3: At low temperatures the current from source to drain through the controlled-barrier atom shows distinct nearly periodic peaks. Between the peaks the number of electrons in the dot is well defined.

For the lateral quantum dot in Fig. 2.1, the level spectrum can be shifted by the bottom gate voltage V_g . The energy of the Coulomb island (i.e. the small electron droplet between the constrictions) can be written semiclassically

$$E = QV_g + Q^2/2C . \quad (2.1)$$

The first term is the attractive electrostatic interaction between the island and the positive gate, the second term is the charging energy due to the repulsion of the electrons on the island. Equation (2.1) is a parabola with its minimum at $Q_m = -CV_g$. However, as charge is quantized, $Q = -Ne$, the energy (2.1) can only assume discrete values. This is shown in Fig. 2.5. When $Q_m = -Ne$ the Coulomb interaction results in the same energy difference $e^2/2C$ for increasing or decreasing N by one. Only when the gate voltage is adjusted to $Q_m = -(N + 1/2)e$, the state with N and $N + 1$ electrons are degenerate and the charge fluctuates³. Therefore the peak spacing in Fig. 2.3 is e/C , it thus increases inversely with the length between the two constrictions.

In the all-metal atom of Fig. 2.4 the energy spectrum is effectively continuous. Also in the controlled barrier atom the charging energy e^2/C is much larger than the mean quantum level spacing. We will later illustrate the experiments of TARUCHA ET AL. (1996) who succeeded in building very small quantum dots with very few electrons. There, the single-particle level spacing is comparable to the charging energy. This means that the quantum level structure is discernible in the conductance peak spectrum.

³The capacitance C has also been calculated numerically for a realistic model of the lateral quantum dot in Fig. 2.1 and so it has been assured that one conductance peak in Fig. 2.3 really corresponds to the addition of *one* electron (KASTNER, 1992).

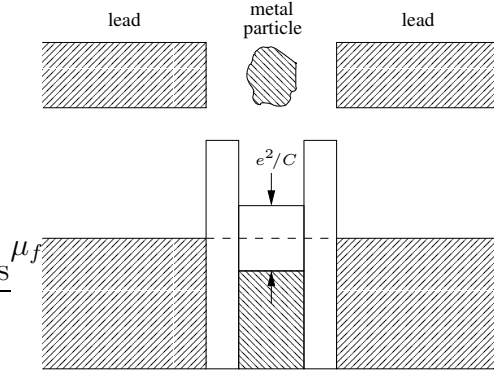


Fig. 2.4: Metal particle in a tunnel junction and energy spectrum for that system. Due to Coulomb repulsion, an electron (hole) from the leads can only tunnel onto the particle if it has an energy $e^2/2C$ above (below) the Fermi energy μ_f .

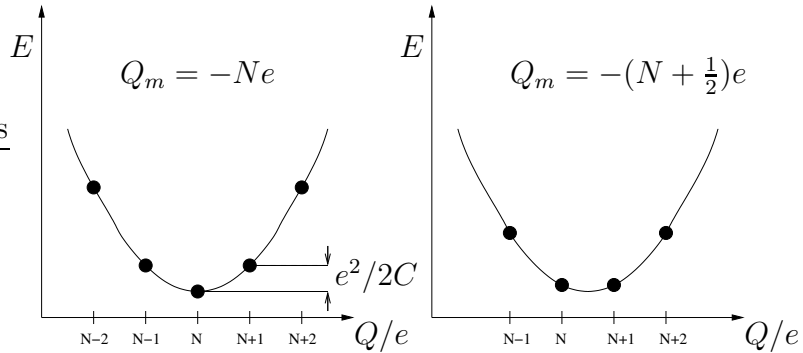


Fig. 2.5: Coulomb blockade parabola, i.e. energy vs. charge on a semiclassical dot.

Actually in a correct quantum-mechanical description, the ground-state energy $E(N)$ enters, which is the energy of N interacting electrons in the quantum dot. The chemical potential of the dot is defined as

$$\mu(N) = E(N) - E(N - 1) . \quad (2.2)$$

A current can only flow through the dot when its chemical potential is between the chemical potentials of source and drain. For small voltages $eV_{sd} = \mu_{\text{source}} - \mu_{\text{drain}} \approx 0$ the N -th Coulomb peak is a direct measure of the chemical potential of the N -electron quantum dot. The spacing between the N -th and $(N + 1)$ -th peak is

$$\Delta(N)/e = [\mu(N + 1) - \mu(N)]/e = \alpha[V_g(N + 1) - V_g(N)] \quad (2.3)$$

where $\Delta(N)$ is the so-called addition energy. It is related to the gate voltage simply by a dimensionless factor α which depends on the geometry of the device. Equation (2.3) is the link between the gate voltages measured in the experiment and the $E(N)$ that we want to calculate.

2.3 Model Hamiltonian

Before we illustrate important experiments in more detail, we present a suitable model Hamiltonian. It describes the quantum dot as a closed system of interacting 2D electrons in an external isotropic parabolic potential. We thus do not model the tunneling and the leads, as we are interested in the case that tunneling is sufficiently weak, so that the dot can be idealized as an isolated system with a well defined electron number and we seek for their interacting ground state.

As one can guess from Fig. 2.2 the confinement potential in the plane can be described as harmonic to a good approximation⁴. This model has also been checked numerically in self-consistent calculations which solved the Poisson and Schrödinger equations iteratively for realistic devices (KUMAR ET AL., 1990; BEDNAREK ET AL., 2000). Our model Hamiltonian for the quantum dot with magnetic field reads

$$\mathcal{H} = \sum_{i=1}^N \left\{ \frac{1}{2m^*} [\mathbf{p}_i + e\mathbf{A}(\mathbf{x}_i)]^2 + \frac{m^*\omega_0^2}{2} \mathbf{x}_i^2 \right\} + \sum_{i<j} \frac{e^2/\kappa}{|\mathbf{x}_i - \mathbf{x}_j|}. \quad (2.4)$$

Here, m^* is the effective mass of the electron, and $e = |e|$ is the electron charge. The harmonic oscillator frequency is ω_0 and $\kappa = 4\pi\epsilon\epsilon_0$ is the Coulomb coupling with the dielectric constant ϵ . The vector potential of a homogeneous magnetic field \mathbf{B} orthogonal to the plane of the quantum dot in symmetric gauge reads $\mathbf{A}(\mathbf{x}) = \frac{B}{2}(-y, x, 0)$ with the corresponding cyclotron frequency $\omega_c = eB/m^*$. In our Hamiltonian we have omitted the Zeeman term, which can be easily included. We also neglect normal spin-orbit coupling (which is very small in GaAs) and the Rashba effect, which is spin-orbit coupling due to the electric field in an asymmetric confining potential in z -direction⁵.

Now we can introduce oscillator units, and describe the system dimensionless: energies in units of the oscillator energy

$$\hbar\omega = \hbar\sqrt{\omega_0^2 + \omega_c^2/4}, \quad \mathcal{H} = \hbar\omega H, \quad (2.5a)$$

and lengths in units of oscillator lengths

$$l_0 = \sqrt{\frac{\hbar}{m^*\omega}}, \quad \mathbf{x} = l_0 \mathbf{r}. \quad (2.5b)$$

⁴This is not true for self-assembled quantum dots which can have disk, lens, pyramidal or even ring shapes (see e.g. LORKE ET AL., 2000).

⁵Zeeman coupling, $H_Z = g^*\mu_B B\sigma_z$, in GaAs is rather weak and solely tends to polarize the electrons. Rashba coupling, $H_R = k_R(\sigma_x p_y - \sigma_y p_x)$, can be tuned via externally applied voltages and breaks the spin invariance (2.8). GOVERNALE (2002) has shown by a spin-density functional study that it can affect the addition energies of a quantum dot by a suppression of Hund's rule.

Then the Hamiltonian is formally the same as without magnetic field

$$\begin{aligned}
 H &= \sum_{i=1}^N \left\{ -\frac{1}{2} \Delta_i + \frac{1}{2} \mathbf{r}_i^2 - \frac{\omega_c}{2\omega} L_z^{(i)} \right\} + \sum_{i<j} \frac{\lambda}{|\mathbf{r}_i - \mathbf{r}_j|} \\
 &\equiv \sum_{i=1}^N h_i + \sum_{i<j=1}^N w_{ij},
 \end{aligned} \tag{2.6}$$

apart from an additional term proportional to the total angular momentum which scales with the dimensionless cyclotron frequency $\Omega_c := \omega_c/\omega$. Here, we have introduced the dimensionless coupling constant which tunes the electron interaction⁶

$$\lambda = \frac{l_0}{a_B^*} = \frac{e^2/\kappa l_0}{\hbar\omega}, \tag{2.7}$$

with the effective Bohr radius of the host material $a_B^* = \frac{\kappa\hbar^2}{m^*e^2} = \frac{\epsilon m_e}{m^*} a_B$. Since this Hamiltonian is spin-independent and invariant under rotation about the z -axis,

$$[H, L_z^{\text{tot}}] = [H, \mathbf{S}_{\text{tot}}^2] = [H, S_z^{\text{tot}}] = 0, \tag{2.8}$$

the exact eigenfunctions can be chosen as simultaneous eigenfunctions of the total angular momentum L_z^{tot} , the total spin $\mathbf{S}_{\text{tot}}^2$ and its z -component S_z^{tot} . These eigenfunctions and the corresponding densities are then rotationally invariant (cf. Sec. 4.1.3). Later we also include an impurity to break the rotational symmetry of the 2D harmonic oscillator.

To illustrate the parameters, we give some material constants (SZE, 1981) and the corresponding λ for two different confinement strengths at zero magnetic field.

	m^*/m_e	ϵ	a_B^*/nm	l_0/nm	$\lambda = l_0/a_B^*$ [$\hbar\omega_0 = 3\text{meV}$]	l_0/nm	$\lambda = l_0/a_B^*$ [$\hbar\omega_0 = 0.7\text{meV}$]
GaAs	0.067	13	10	19	1.9	40	4
InSb	0.015	18	60	41	0.7	85	1.4
Si	0.3	12	2	9	4.5	13	6.5

We see that the interaction can be widely tuned by varying the material and the confinement strength. Later we will also return to the point how λ is related to the density and the Brueckner parameter r_s . Experiments are mostly done with AlGaAs-GaAs based dots which allows for very clean structures. Our task is now to calculate the ground-state properties of this closed quantum dot, especially the ground-state energy $E(N)$.

⁶Note that $\Omega_c \leq 2$. In other words, for a given material with effective Bohr radius a_B^* and given magnetic field ω_c , there is a maximal coupling constant $\lambda \leq \lambda_m := \sqrt{2}l_m/a_B^*$, where $l_m = \sqrt{\hbar/m^*\omega_c}$. In particular, $\lambda \rightarrow 0$ for $\omega_c \rightarrow \infty$.

2.4 Non-interacting eigenstates and shell filling

As a starting point we introduce the non-interacting eigenstates of the isotropic 2D harmonic oscillator which are not changed by the magnetic field. Since L_z is a constant of motion we give the angular momentum basis of the 2D harmonic oscillator and a visualization of the eigenenergies. The Hartree-Fock calculation is performed in this basis. The single-particle Hamiltonian of Eq. (2.6) reads

$$h = -\frac{1}{2} (\Delta - \mathbf{r}^2 - \Omega_c L_z) . \quad (2.9)$$

The normalized eigenfunctions of h are the Fock-Darwin states (FOCK, 1928; DARWIN, 1930)

$$\langle \mathbf{r} | nM \rangle = \sqrt{\frac{n!}{\pi(n+m)!}} e^{iM\phi} r^m \mathcal{L}_n^{(m)}(r^2) e^{-r^2/2} , \quad (2.10)$$

where n is the non-negative integer radial quantum number. The angular momentum quantum number M is integer, and $m = |M|$. $\mathcal{L}_n^{(m)}$ are generalized Laguerre polynomials (GRADSTEIN and RYSHIK, 1965)

$$\mathcal{L}_n^{(m)}(x) = \sum_{k=0}^n (-1)^k \binom{n+m}{n-k} \frac{x^k}{k!} \quad (2.11)$$

The common eigenstates of h and L_z then fulfill

$$h |nM\rangle = \varepsilon_{nM} |nM\rangle \quad \text{and} \quad L_z |nM\rangle = M |nM\rangle \quad (2.12)$$

with eigenenergies

$$\varepsilon_{nM} = (2n + m + 1) + M\Omega_c/2 . \quad (2.13)$$

We show a graphical illustration of these energy levels for zero magnetic field in Fig. 2.6. In analogy to the hydrogen atom, their degeneracy leads to the energetic shell structure for weak interaction. The degeneracy of the k -th level with energy $E_k = \hbar\omega(k+1)$ is $2k+2$ for spinful electrons. This gives the so-called *magic numbers* which are total numbers of electrons in closed shells $N(k) = (k+1)(k+2) = 2, 6, 12, 20, 30, \dots$ and correspond to energetically very stable fillings.

With these one-particle states one can now make the so-called constant interaction approximation for the addition energies (2.3). One assumes that the total energy is given by the sum over the occupied oscillator states plus the Coulomb interaction which is parametrized by a constant capacity C . The addition energies (2.3) then read

$$\Delta(N) = E(N+1) - 2E(N) + E(N-1) = \begin{cases} e^2/C + \hbar\omega_0 & \text{if } N = 2, 6, 12, \dots, \\ e^2/C & \text{else,} \end{cases} \quad (2.14)$$

and are maximal for closed shells. This is the 'atomic' shell-structure of quantum dots which relies on the symmetry of the 2D harmonic oscillator.

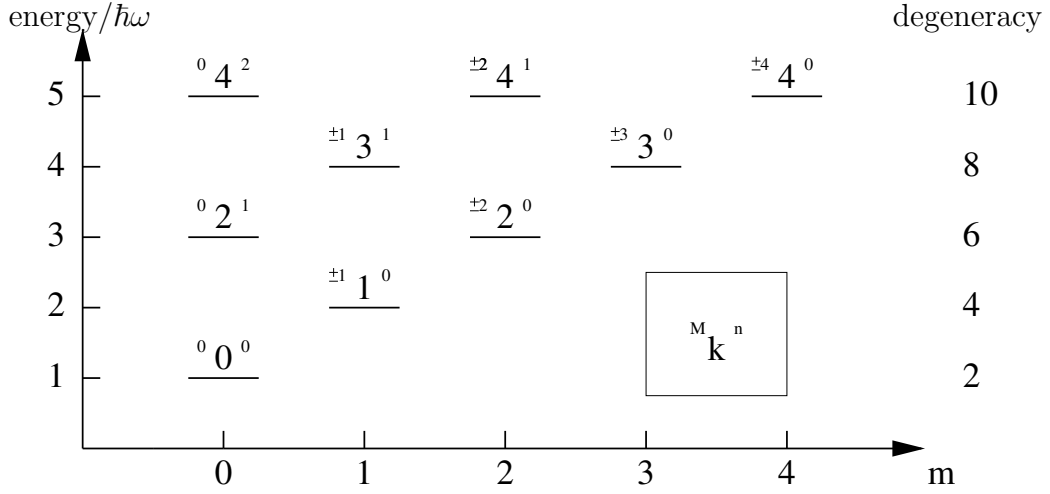


Fig. 2.6: Energy levels $E_k = E_{nM} = \hbar\omega(2n + |M| + 1) = \hbar\omega(k + 1)$ of the 2D isotropic harmonic oscillator at zero magnetic field; $m = |M|$. The inset shows the spectroscopic notation: k is the energy quantum number, n and M are the radial and angular momentum quantum numbers.

2.5 Hund's rule and ground-state spin

In addition to the ground-state energy, we are interested in the ground-state total spin whose proper determination is a difficult task. For weak interaction, one expects Hund's rule for the shell filling of the orbitals in Fig. 2.6: Degenerate orbitals are singly occupied with parallel spin which minimizes the Coulomb repulsion. Therefore, half-filled shells are exceptionally stable⁷. This Hund's rule shell filling is in complete analogy to conventional atomic physics and has indeed been found in the experiment for small few-electron dots (see Fig. 2.10).

On the theoretical side, we have to precise that approximative methods often work in the subspace of fixed S_z^{tot} and break the $\mathbf{S}_{\text{tot}}^2$ symmetry. Sub-Hund's rule spin was predicted in a spin-density functional (SDFT) calculation by HIROSE and WINGREEN (1999) for $N > 22$ and $\lambda = 1.9$. In general, restricted Hartree-Fock (HF) calculations give unphysically high values for the spin of the interacting ground state, whereas unrestricted HF can also underestimate the spin for small interaction. We note also that a diffusion Monte Carlo calculation based on SDFT trial wave functions (PEDERIVA ET AL., 2000) gave the wrong ground-state spin for $N = 4$ (cf. REIMANN and MANNINEN, 2002). Thus essentially exact methods are necessary to obtain the correct spin ordering. A quantum Monte Carlo (QMC) study (EGGER

⁷For stronger interaction however, there might be a competing mechanism: Orbitals in the same shell with higher angular momentum are lower in energy because they are further apart from the center. This would favor double occupancy of orbitals with higher angular momentum, e.g. for nine electrons.

ET AL., 1999) found for strong correlations several cases ($N = 6, 7, 8$) of spins larger than the Hund's rule value.

2.6 Brueckner parameter r_s

Another parameter to characterize the interaction strength of the 2D electrons is the so-called Brueckner or Wigner-Seitz dimensionless density parameter r_s . In homogeneous systems it is defined by the radius of the circle that every electron occupies effectively in units of a_B^* , so the homogeneous density is $n_0 = 1/[\pi(a_B^*r_s)^2]$.

For few-electron quantum dots, it is difficult to define an overall density, but there are many ways to define r_s . EGGER ET AL. (1999) determined r_s numerically from the first maximum of the two-particle correlation function. KOSKINEN ET AL. (1997) used the formula $r_s^3 = \lambda^4/\sqrt{N}$ and FILINOV ET AL. (2001) obtained $r_s^3 = 2\lambda^4$. For $N < 10$ and $\lambda \leq 10$ all these dependencies agree qualitatively (apart from a trivial factor of two because some authors define r_s as the nearest-neighbor distance). We define r_s as half the nearest-neighbor distance. In Sec. 2.8 we also give the values of r_s for classical electrons.

2.7 Strongly interacting limit: Wigner molecule

Now we consider the limit of very strong correlations. For the case of the homogeneous electron gas, WIGNER (1934, 1938) has shown that for low density ($r_s \rightarrow \infty$), one can minimize the energy of the system by allowing the electrons to *crystallize* in a so-called Wigner crystal. Accordingly, 2D interacting electrons form a hexagonal lattice. This situation occurs because the zero-point energy associated with localizing the electrons eventually becomes negligible in comparison to the electrostatic energy of a classical lattice (FETTER and WALECKA, 1971). QMC studies have predicted the critical value of r_s for the Wigner crystallization of the 2DEG as $r_c^{cl} \approx 37 \pm 5$ for clean systems (TANATAR and CEPERLEY, 1989) and $r_c^{dis} \approx 7.5$ for disordered systems (CHUI and TANATAR, 1995). Wigner crystallization is also thought to be related to the experimentally found apparent 2D metal-insulator transition (ABRAHAMS ET AL., 2001). Wigner crystallization is a typical example for a quantum phase transition. At zero temperature the melting of the crystal is driven by quantum fluctuations, i.e. the oscillatory motion of the electrons about their lattice points.

In few-electron quantum dots, the crossover to the so-called Wigner molecule, i.e. the small finite-size counterpart to the Wigner crystal, has been analyzed by many authors with various methods in the last years. BRYANT (1987) investigated the behavior of two electrons in rectangular quantum-well boxes with hard-wall confinement. He found signatures of Wigner crystallization in the electronic structure and the spatial correlation function. Polygonal dots without rotational symmetry

have been considered in a recent SDFT study by RÄSÄNEN ET AL. (2003) and also by CREFFIELD ET AL. (1999), who showed that for low densities, the continuous problem [analog to (2.6) with two electrons] can be mapped on a lattice model.

In the isotropic parabolic potential, there is no preferential orientation for crystallization. The electrons form a Wigner molecule that consists of various spatial shells, corresponding to electrons arranged on concentric circles. With path-integral Monte Carlo (PIMC) simulations EGGER ET AL. (1999) have determined the critical parameter $r_c \approx 2$ for the formation of the Wigner molecule. In a subsequent PIMC study for stronger interaction and higher electron number, FILINOV ET AL. (2001) have found that the crystallization is actually a two-stage process: After the radial ordering of the electrons into shells, the freezing of inter-shell rotation proceeds at a much higher r_s .

Naturally, the exact value for the critical r_s depends on the criterion which one chooses to discriminate the Wigner crystallization. EGGER ET AL. (1999) have considered the spin sensitivity of the two-particle correlation function, whereas FILINOV ET AL. (2001) used a Lindemann criterion for the radial and angular fluctuations. Another interesting option for small dots or quantum rings is to seek for signatures of rotations and vibrations of the molecule in the many-electron spectra (YANNOULEAS and LANDMAN, 2000a; KOSKINEN ET AL., 2001). Obviously, one can have a direct look at the one- or two-particle densities which gives a qualitative impression of the stage of crystallization. Here, however, mean-field methods have to be regarded with care because of the symmetry breaking. In the following, we will cite other works when we directly compare them with our calculations and refer to a recent review article on the electronic structure of quantum dots by REIMANN and MANNINEN (2002).

2.8 Classical electrons

We are interested in the crossover to the strongly interacting regime and the charge distribution in this case. Therefore, to understand the structure of the wave function, we give the classical rest positions and energies for up to seven 2D electrons in a parabolic confinement potential in Table 2.1. Here, r_a is the distance of the outer electrons from the center measured in oscillator length l_0 , while r_s is half the nearest-neighbor distance measured in effective Bohr radii a_B^* . Energies are given in units of $\hbar\omega_0$. These quantities depend only on N and λ .

For $N = 5$ and 6 we specify two isomers with higher energies. Due to the classical virial theorem (cf. Sec. 3.1.6), there is a simple relationship between the energy and r_a . When we denote the distance of the i -th electron from the center by $r_a(i)$, we have

$$E = \frac{3}{2} \sum_{i=1}^N r_a(i)^2 . \quad (2.15)$$

N	Geometry	r_a^3/λ	$r_s/\lambda^{4/3}$	$E/\lambda^{2/3}$	E/r_a^2
2	dumbbell (2)	$\frac{1}{4}$	≈ 0.630	≈ 1.191	3
3	triangle (3)	$\frac{1}{\sqrt{3}} \approx .577$	≈ 0.721	≈ 3.120	$\frac{9}{2}$
4	square (4)	$\frac{1}{4} + \frac{1}{\sqrt{2}} \approx .957$	≈ 0.697	≈ 5.827	6
5	pentagon (5)	$\sqrt{1 + \frac{2}{\sqrt{5}}} \approx 1.376$	≈ 0.654	≈ 9.280	$\frac{15}{2}$
5*	square (4,1)	$\frac{5}{4} + \frac{1}{\sqrt{2}} \approx 1.957$	≈ 0.625	≈ 9.388	6
6	pentagon (5,1)	$1 + \sqrt{1 + \frac{2}{\sqrt{5}}} \approx 1.827$	≈ 0.667	≈ 13.356	$\frac{15}{2}$
6*	hexagon (6)	$\frac{5}{4} + \frac{1}{\sqrt{3}} \approx 1.827$	≈ 0.611	≈ 13.452	9
7	hexagon (6,1)	$\frac{9}{4} + \frac{1}{\sqrt{3}} \approx 2.827$	≈ 0.707	≈ 17.996	9

Table 2.1: Ground-state configurations and energies for classical point charges in the 2D oscillator. For $N = 5, 6$ particles, we also give the values for isomers with higher energy.

This classical energy is a lower bound for the true quantum-mechanical ground-state energy. The first semiclassical corrections would include vibrations, rotations, and spin effects. The equilibrium configurations for higher electron numbers were obtained by classical MC simulations (BEDANOV and PEETERS, 1994; MARLO ET AL., 2002, e.g.). For $N = 6, 16, 32, \dots$ an electron enters the center and a new spatial shell appears. However, closed spatial shells are not exceptionally stable because isomers with different shell structure are very close in energy. For example, the nine- and ten-electron classical ground-state configurations (2,7) and (2,8) lie energetically only slightly below the (1,8) and (3,7) states⁸. For larger electron number there is an interplay between these onion-like shells and the formation of a hexagonal lattice in the interior of the dot⁹.

⁸Quantum and thermal fluctuations can induce transitions between these spatial shell-fillings (see EGGER ET AL., 1999; FILINOV ET AL., 2001).

⁹For macroscopic realizations of 2D Wigner molecules see MAYER (1878); SAINT JEAN ET AL. (2001). Classical molecular dynamics for a similar system (point charges confined by a magnetic field) were performed by REUSCH and BLÜMEL (1998). Classical configurations for 3D were first obtained analytically for up to $N = 20$ by FÖPPL (1912) who had been inspired by the atomic model of THOMSON (1904).

2.9 Impurity

In our path-integral Monte Carlo study we also include a single attractive impurity which we model by a Gaussian

$$V_{\text{imp}}(\mathbf{r}) = -w \exp \left\{ \frac{-(\mathbf{r} - \mathbf{x})^2}{2\sigma^2} \right\}. \quad (2.16)$$

The impurity is located on the y -axis at $\mathbf{x} = (0, y_0)$. The width of the Gaussian is σ and its depth is controlled by w . It breaks the rotational symmetry of the parabolic confinement but we still have the symmetry with respect to the y -axis. One expects that this should enhance localization because the Wigner molecule is pinned at the impurity. In the GaAs experiments the impurities are given by positively charged Si donors. We state that the detailed form of the defect should not matter as long as rotational symmetry is efficiently broken¹⁰.

For electron numbers $N = 1-10$, we have investigated the following parameters: The coupling constant $\lambda = 4$ corresponds to a nearest-neighbor electron distance of $\approx 8a_B$ ($r_s \approx 4$). The impurity is located at $\mathbf{x} = (0, 1.5)$ with *radius* $2\sigma = 0.75 =: \varsigma$ and strength $w = 4$ (Fig. 2.7). The choice of these parameters has been motivated as follows: We are in an intermediate regime where Wigner crystallization sets in. At this interaction strength only one electron enters the impurity (two classical electrons with distance ς have the Coulomb energy $\lambda/\varsigma \approx 5.3$). The thermal energy (chosen below) $k_B T = 0.125$ is small compared with the impurity depth. The impurity is located not too far away from the center and strong enough so that the electrons feel its influence. The matrix element of the impurity potential with respect to the 2D harmonic oscillator ground state is

$$\langle 00 | V_{\text{imp}} | 00 \rangle = -\frac{w \varsigma^2}{\varsigma^2 + 2} \exp \left\{ \frac{-2y_0^2}{\varsigma^2 + 2} \right\} \approx -0.152, \quad (2.17)$$

of the order of $k_B T$. However, we expect that the influence of the defect is enhanced because of the Coulomb interaction. By integrating the density over the radius ς we obtain that for $N > 1$ about 75% of an electron charge is trapped by our impurity

¹⁰A parabolic quantum dot with up to three repulsive impurities of this form and $N < 4$ has been studied with exact diagonalization by (HALONEN ET AL., 1996). Some of their results seem incorrect to us, when we compare them to first-order perturbation theory in w . Extensive density functional theory studies (HIROSE ET AL. 2001, 2002) have investigated this model with stronger disorder. In the first work they considered spin-polarized dots with 10–20 impurities with $w \in [-6, 6]$ and fixed $\sigma = l_0/(2\sqrt{2})$. They varied $0 \leq \lambda < 4$ (corresponding to $0 < r_s \lesssim 4$) by changing κ and keeping $\hbar\omega_0 = 3\text{meV}$ fixed. They then averaged over ~ 1000 disorder configurations and considered the fluctuations of the addition energy of the tenth electron $\Delta(10)$. They found that these fluctuations are well described by a convolution of a Wigner-Dyson distribution (which is predicted by Random Matrix theory for non-interacting particles) and a Gaussian (for finite interaction).

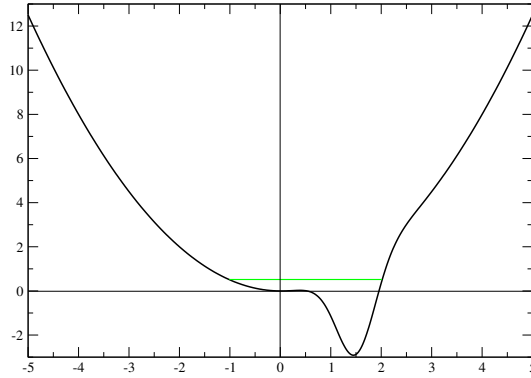


Fig. 2.7: Parabolic confinement potential with impurity along the y -axis of our dot. The lowest single-particle energy is about $\varepsilon_0 \approx 0.51$.

(Sec. 3.4.2). Therefore we have also an interesting model for a localized spin which interacts with the rest of the electrons, similar to the Kondo model. Our primary interest, however, is how the ground-state spin and the addition energies are affected by the impurity.

2.10 Temperature and thermal melting

In our calculations the Hartree-Fock method is for zero temperature. The path-integral Monte Carlo (PIMC) is performed in the canonical ensemble for a given inverse temperature $\beta = 1/k_B T$. Here, as for all other energies, we measure $k_B T$ in units of $\hbar\omega$. We choose $k_B T = 0.125$. With decreasing temperature, PIMC becomes increasingly difficult, because of the fermion sign problem (see Sec. 3.1.8).

The temperature scale is thus directly related to the energy scale that one has chosen: 1 meV corresponds to 11.6 K. On the other hand, for a given value of λ there might be various values of $\hbar\omega_0$ depending on the host material (m^* , κ). For example, $T = 10\text{K}$ and $\hbar\omega_0 = 3\text{meV}$ correspond to $\beta \approx 3.5$ which are the parameters in the PIMC simulation of HARTING ET AL. (2000). At this temperature the fermionic sign problem is still very weak. For our coupling constant $\lambda = 4$ and an energy scale of $\hbar\omega_0 \approx 0.7\text{meV}$ (GaAs), $\beta = 8$ corresponds to $T \approx 8\text{K}$, and the sign problem is quite strong.

In the experiments of ASHOORI (1996) with GaAs based quantum dots the temperature range is $T = 0.05\text{--}0.3\text{K}$ and the oscillator energy is estimated about $\hbar\omega_0 = 0.3\text{--}2.5\text{meV}$ (ASHOORI ET AL., 1992). This yields very high $\beta \approx 11.6\text{--}580$. KOUWENHOVEN-ET AL. (2001) estimate for their experiments $\hbar\omega_0 \approx 3\text{meV}$ and $\beta \approx 170$.

We also want to mention briefly the thermal melting of a Wigner molecule. When the temperature is increased, thermal fluctuations destroy the crystalline shell ordering. It is thus a different process than the quantum melting, where the density is

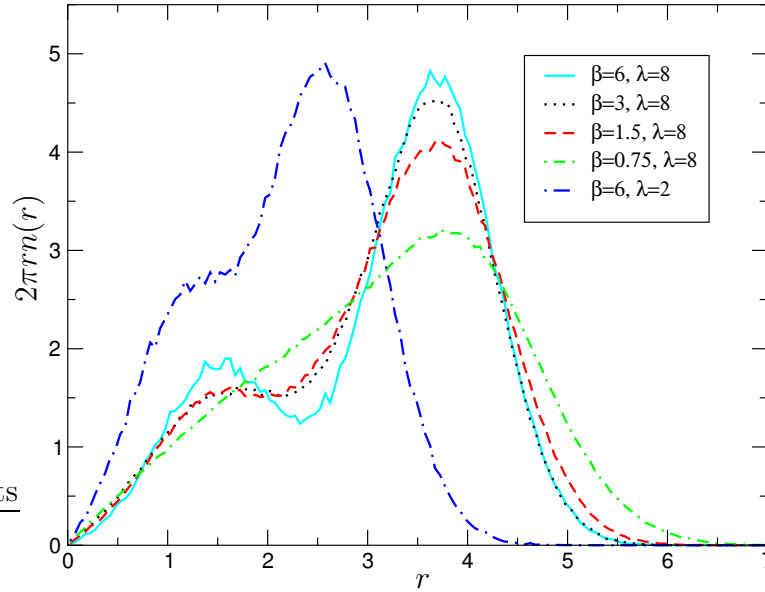


Fig. 2.8: Thermal versus quantum melting as illustrated by the radial charge densities for ten spinless electrons in a clean quantum dot. For strong interaction ($\lambda = 8$) the radial ordering disappears with increasing temperature. For high density ($\lambda = 2$) the spatial shell structure is not yet very pronounced.

increased. We illustrate these two processes in Fig. 2.8 for ten spin-polarized electrons and various couplings and temperatures. The pronounced radial ordering for $\lambda = 8$ vanishes when temperature is increased. On the other hand, for stronger confinement (small λ) the electrons are delocalized and there are no radial shells. However, as we are dealing with a small finite-size system, there seems to be no sharp phase transition in this thermal melting (HARTING ET AL., 2000).

2.11 Few-electron artificial atoms

In this section we describe experiments which have been performed by a cooperation of the University of Delft in the Netherlands and the NTT research laboratories in Japan by KOUWENHOVEN ET AL. (2001). In Fig. 2.9 we show a so-called vertical quantum dot. It consists of a pillar which has been etched from the various layers of a semiconductor heterostructure. The dot's electrons accumulate in the central InGaAs layer which has a thickness of about 12nm. Two insulating AlGaAs layers each about 8 nm thick form the tunnel barriers. Source and drain contacts are made of n-GaAs where the concentration of Si dopants increases away from the tunnel barriers. The top contact is a metal circle which also initially defines the pillar when the structure is etched from the heterostructure. Finally a metallic side gate is evaporated on the pillar and surrounds it. By this side gate, one controls the

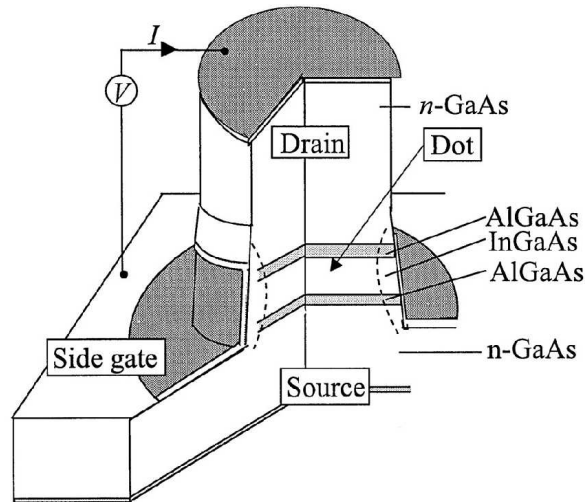


Fig. 2.9: Vertical quantum dot from the experiments of TARUCHA ET AL. (1996). The active InGaAs layer contains from zero to about one hundred confined electrons depending on the strength of the repulsive side gate potential. The diameter of the pillar is $\sim 0.5\mu\text{m}$.

confinement and the number of electrons in the dot. The electronic structure of the system is such that at zero side gate voltage, there are about 80 electrons in the dot. The electrons occupy only the lowest quantum state in vertical direction so that the dot is two-dimensional. By applying an increasingly negative voltage to the side gate, electrons are expelled from the dot one by one until their number is zero. The conductance is measured by applying a very small voltage between source and drain.

In Fig. 2.10 the current is shown in dependence of the side gate voltage. The conductance peaks have very different heights, but, above all, their spacings are not equidistant. The distance between the peaks is (up to a geometric factor) the addition energy which has maxima for the magic numbers of the 2D oscillator (see Sec. 2.4). Further it shows smaller maxima for the half filled shells which is a consequence of Hund's Rule¹¹. The experimentalists estimated the harmonic oscillator level spacing $\hbar\omega_0 = 3\text{meV}$ ($\lambda = 1.9$) and the charging energy of about the same order. This atom-like energetic shell filling for quantum dots was first discovered in 1996 (TARUCHA ET AL., 1996) and it is possible to reproduce these measurements which means that it really has become feasible to produce artificial atoms with precise quantum states in solid-state devices.

¹¹Recently, MATAGNE ET AL. (2002) precised that due to small non-parabolicity effects, these maxima can change even if Hund's rule spin filling is not affected.

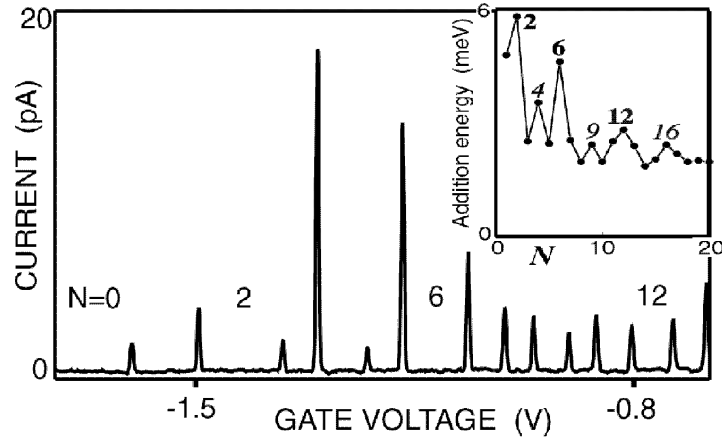


Fig. 2.10: Conductance peaks for the few-electron quantum dots of TARUCHA ET AL. (1996). From the peak spacings, the addition spectrum can be obtained (inset), which shows the shell structure of the 2D harmonic oscillator similar to Eq. (2.14).

2.12 Single-electron capacitance spectroscopy

As a second example, we want to illustrate experiments performed at the MIT by the group of ASHOORI (1996). Their quantum dots are similar to the vertical dots described in the previous chapter. The electrons of the dot are confined in a thin GaAs layer by two AlGaAs tunnel barriers. This vertical structure is sandwiched by a top and a bottom gate which can be considered as two capacitor plates [Fig. 2.11(a)]. The upper plate is made positive and also shaped appropriately in order to confine the electrons in the quantum well laterally. In some experiments also a side gate is included by which the dot is even more strongly squeezed in the lateral direction.

When the top gate voltage is raised electrons enter the dot one by one. In contrast to the experiments in the previous section, here, no conductance is measured, but the capacitance of the structure is determined by measuring the charge induced by the dot on the upper plate. This is done by adding a small AC voltage to the DC top gate voltage V_t . When V_t is adjusted to a value at which an electron can be added to the dot, the AC voltage causes the electron to tunnel back and forth between the dot and the bottom gate. This is symbolized by the double arrow in Fig. 2.11(a). This tunneling corresponds to a strongly enhanced capacitance and can be registered by a synchronous detector.

In Fig. 2.11(c) such a capacitance peak spectrum is depicted in analogy to the conductance peaks shown in the previous section. Many of these quite irregular patterns are combined to one gray-scale plot in Fig. 2.11(b) for varying magnetic field and in (c) for varying side gate voltage. As in the previous section the spacings of these peaks are the addition energies. However, the dots of Ashoori and coworkers are in general larger, with up to $1.2\mu\text{m}$ lithographic diameter and estimated single-

level spacings of $0.3 < \hbar\omega_0 < 2.5\text{meV}$ (ASHOORI ET AL., 1992). For GaAs, this corresponds to $6 \gtrsim \lambda \gtrsim 2$. Therefore the density is lower and interaction effects are more important. Further, in their dots there is disorder caused by Si donors which migrate by diffusion into the quantum well and form attractive impurities. Our PIMC parameters are chosen to describe this situation.

2.13 Bunching of addition energies

In Fig. 2.11(b) the evolution of the addition spectrum for an intermediate sized dot with magnetic field is shown. We consider first the case of zero magnetic field: The first seven electrons enter the dot at largely spaced voltages. These spacing are no longer necessarily equidistant nor do reflect the harmonic oscillator levels. Probably the electrons enter into a single potential minimum or into several local minima that are close enough so that Coulomb repulsion is sufficient to keep the peaks widely spaced. Beyond the seventh electron trace there is a strange phenomenon: Three electrons enter the dot at nearly the same gate voltage. Also the next two electrons enter the dot in a bunch (pair). This behavior was first seen in 1992 (ASHOORI ET AL., 1992). It appears to be a violation of Coulomb blockade and is called bunching (ZHITENEV ET AL., 1997).

After about 40 electrons are added, the bunching develops into a quasi periodic pattern with a bunch appearing every 4th to 6th electron. For $N > 80$ the peaks are spaced equidistantly because the density is already quite high and Coulomb blockade behavior is found. This is connected to a crossover from localization to delocalization: At high density the electronic states are spread out over the whole dot. However, here the bunching reappears when a magnetic field is switched on, probably because then electrons are further localized.

The experimentalists made a systematic study (ASHOORI ET AL., 1998) and tried to establish a phase diagram for the bunching phenomenon. The bunching is not found for high densities, i.e. for small dots or large electron number. With a magnetic field however, the bunching can be extended to regions of higher density. The authors claim that it is an universal effect.

In a modified experiment, ZHITENEV ET AL. (1999) also included a side gate [see Figs. 2.11(a),(c)]. The addition spectra are less affected by the side gate than by the top gate which can be seen when considering the different magnitudes of the voltages in Fig. 2.11(c). The side gate voltage V_s has stronger influence on states which are localized at the perimeter of the dot. It allows to detect these states because they have a very large slope with respect to V_s . Other traces with small slope correspond to interior states. In Fig. 2.11(c) the arrow points to a characteristic edge localized state. It shows interesting 'avoided crossings' with level splittings that are a measure of the 'interaction' of this state with the interior states. The experimentalists deduced that at the bunching points electrons tunnel into different puddles at the center and the

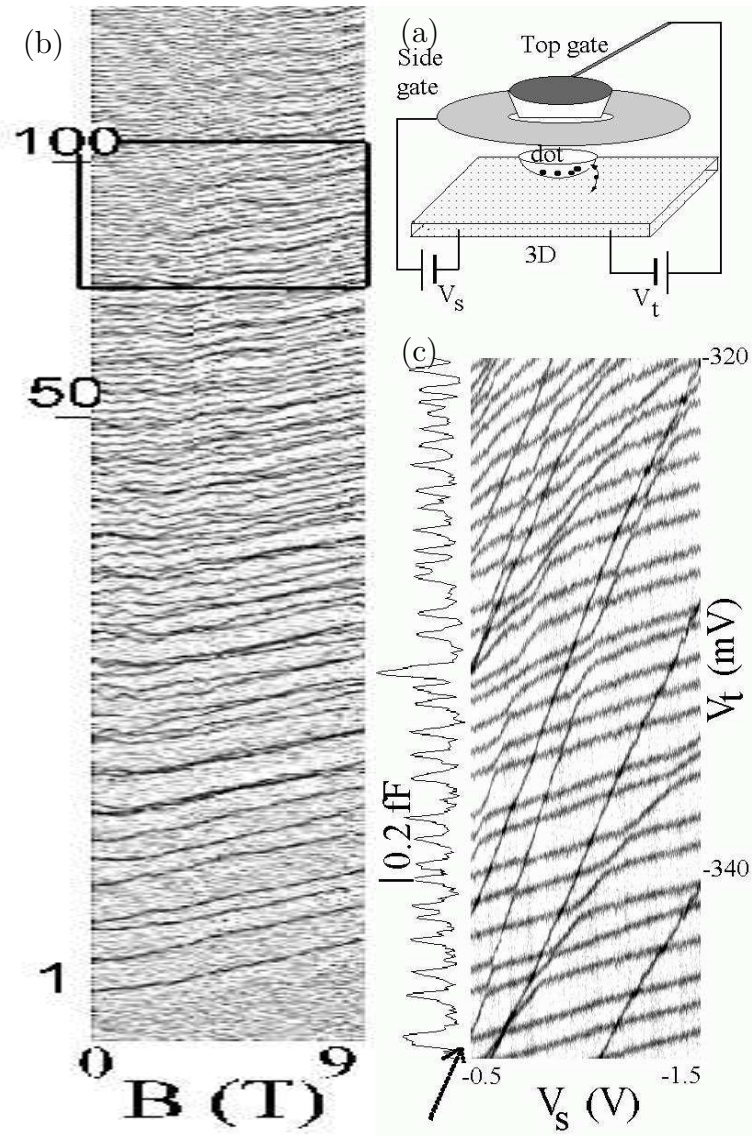


Fig. 2.11: Single-electron capacitance spectroscopy. In (a) schematic picture of the device similar to the one in Fig. 2.9. In (b) gray-scale plot of capacitance vs. top gate voltage or equivalently electron number (from one to ~ 140 electrons) for varying magnetic field (ZHITENEV ET AL., 1997). In (c) capacitance vs. top gate voltage for varying side gate voltage (ZHITENEV ET AL., 1999).

perimeter of the dot. Note that other localized states do not show this anti-crossing splitting. They appear not to interact with the interior states, maybe because they are out of reach.

Ashoori et al. interfered from the pattern of the anti-crossings that there exists an effective attraction between electrons in different localized regions. They concluded that the bunching is intrinsically linked to the localization-delocalization transition and specified the critical density in the experiment at a Brueckner parameter of about $r_c \approx 1.8$. This value is much lower than the values calculated for the crossover to the Wigner crystal in the infinite 2DEG (see Sec. 2.7), instead it is in good agreement with $r_c \approx 2$ as calculated by EGGER ET AL. (1999) for the Wigner crystallization of a few-electron quantum dot.

Finally, in another subsequent experiment with a dumbbell shaped top gate, the same group investigated a quantum dot with two potential minima which represents a system with artificial disorder (BRODSKY ET AL., 2000). They found that pairings of the addition peaks can be controlled by a strong magnetic field which splits up the low-density droplet into two fragments, corresponding to the two local minima. Apparently, once again, there exists a mechanism that cancels the Coulomb repulsion of electrons in these fragments.

2.14 Theoretical approaches for the bunching phenomenon

We have presented two different groups of experiments that mainly inspired our calculations. While the effects for the small few-electron quantum dots of Kouwenhoven et al. are theoretically quite well understood, the phenomenon of bunching is not yet clarified. WAN ET AL. (1995) tried to explain it by a polaronic effect due to electron-phonon interaction. RAIKH ET AL. (1996) found bunching when they analyzed certain geometries of impurities and classical electrons with short-range interaction. However, both approaches imply coherent tunneling while experimentalists found sequential tunneling, i.e. electrons enter the dot independently at very close gate voltages.

A numerical study for a small system has been performed by CANALI (2000). He considered a tight-binding Hamiltonian with random disorder and nearest-neighbor Coulomb repulsion

$$H = \sum_i (\varepsilon_i - eV_g) \hat{a}_i^\dagger \hat{a}_i + t \sum_{\langle i,j \rangle} (\hat{a}_i^\dagger \hat{a}_j + H.c.) + V \sum_{\langle i,j \rangle} \hat{n}_i \hat{n}_j + U \sum_i \hat{n}_{i\uparrow} \hat{n}_{i\downarrow} .$$

Here, $\varepsilon_i \in [-W, W]$ is the random site energy, t is the tunneling constant, $V = e^2/a$ is the nearest-neighbor Coulomb interaction constant with a the lattice constant and U is the Hubbard on-site repulsion. The electron number in the dot is controlled by

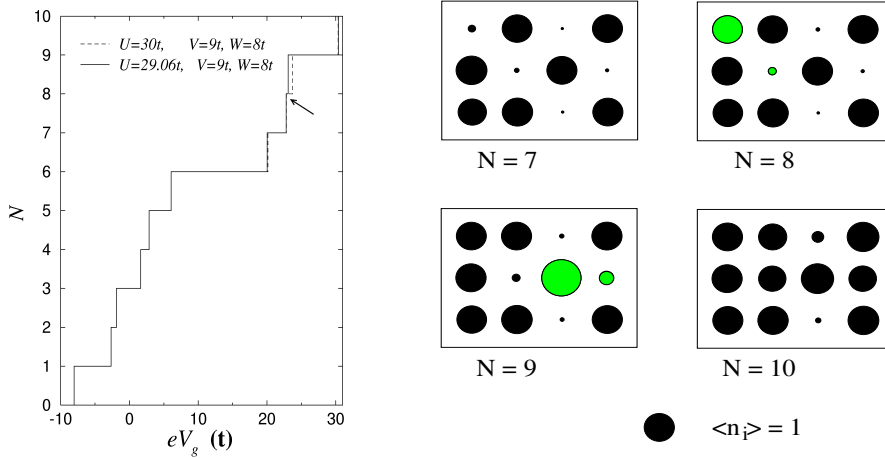


Fig. 2.12: Coulomb staircase, i.e. electron number in the dot versus gate voltage, for one particular disorder realization and two slightly different U . The eighth and ninth electron, are added to the dot at nearly the same V_g , i.e. $\Delta(8)/e = [V_g(9) - V_g(8)] \approx 0$ (arrow). Corresponding ground-state site occupations $\langle \hat{n}_i \rangle$ for $N = 7 - 10$ and $U = 30t$. The gray circles indicate the sites where the largest portion of the incoming electron, participating in the pairing, is distributed (CANALI, 2000).

the gate voltage V_g . With an exact diagonalization for $N < 11$ spinful electrons and a 3×4 lattice he found indeed vanishing addition energies for eight or nine electrons. He interpreted this finding for strong on-site repulsion with two different mechanisms: (i) For intermediate Coulomb interaction two electrons tunnel to different sites in the dot (at $r_s \approx 0.5$)¹². (ii) For stronger Coulomb interaction one electron tunnels to the center and forms a singlet, the other electron tunnels into an edge state (at $r_s \approx 2$, see Fig. 2.12).

However, we find that the lattice model is not entirely convincing. The lattice is quite small and also it does not model the (smooth) external potential. For example there is an artificial maximum in the addition energy for a half filled lattice (large $\Delta(6)$ in Fig. 2.12)¹³. Furthermore, the Coulomb interaction potential in the dot should not show significant screening. In any case, it is not screened in a Hubbard- U way.

¹²He determined $r_s = \frac{2}{\sqrt{\pi n}}(Va/4t)$ by the overall density of the rectangular dot $n = N/(6a^2)$.

¹³Such magic fillings coinciding with the related classical charge model were investigated within the Hartree-Fock approximation for a 16×16 lattice and short-range interaction by WALKER ET AL. (2003). We cite other calculations for lattice models at the end of Sec. 3.4.1.

2.15 Open questions addressed in this thesis

In the present thesis we study the importance of correlations in few-electron quantum dots within the unrestricted Hartree-Fock (UHF) approximation and the exact path-integral Monte Carlo (PIMC) method. For weak correlations, the confined electrons can show atom-like properties. Here, the Hartree-Fock method is expected to give qualitatively correct results. For stronger interaction, the electrons in the dot form a Wigner molecule which shows spatial ordering and correlation. Signatures of the onset of this crystallization have been found in recent experiments.

The formation of the Wigner molecule is expected to be strongly affected by the influence of disorder. We therefore include a defect in the confinement potential for the PIMC study. This single attractive impurity breaks the rotational symmetry of the external oscillator and can localize an electron and thereby pin the Wigner molecule. We underline the importance to study a generic model for weak disorder and interaction in 2D to take into account the experimental situation and note that the localization-delocalization transition has been probed recently in larger quantum dots. so Wigner molecule spectroscopy is within reach of current technology.

We are treating the full continuum problem, and the PIMC allows us to investigate any form of the impurity potential and long-range interaction, though we cannot afford to do the calculation for many disorder configurations. In our realistic model of a quantum dot, electrons arrange in spatial shells and are not restricted to the lattice points of a discrete model. In this context we are especially interested to know if the bunching phenomenon can be found and explained with our model. In general, it is an open question how ground-state energies and spins are influenced by an impurity.

While Hartree-Fock is a traditional method of many-electron quantum mechanics, the application of its spin- and space-unrestricted version for a few strongly correlated 2D electrons is new. We show and explain how the symmetry-violating UHF mean field mirrors the Wigner crystallization in the clean quantum dot. We compare our UHF findings with exact PIMC results, which enables us to assess quantitatively the accuracy of the computationally less demanding mean-field method.

3 Path-integral Monte Carlo simulation

In the present chapter we describe in detail our path-integral Monte Carlo (PIMC) simulations. We start by introducing the basic idea of Monte Carlo integration and the Metropolis algorithm, by which it is often implemented. Then we apply this computation scheme to the many-electron discretized path-integral (PI) which allows us to calculate in an essentially exact numeric way expectation values for the interacting electron system. A serious limitation to quantum Monte Carlo simulations in general is the so-called *sign problem*. It results in a signal-to-noise ratio which vanishes exponentially with increasing electron number and inverse temperature. We show that the expectation value of the sign can be understood as a measure of quantum effects for the many-fermion system.

Having introduced the method, we report various tests and crosschecks that we have performed for our PIMC simulations. We also explain the extrapolation that we use to eliminate the error due to an approximate short-time propagator, the so-called Trotter error. We have obtained analytical results and performed an exact diagonalization for the two-electron quantum dot. These calculations illustrate the temperature dependence and the problem of finite-temperature spin contamination. For three and four electrons in the clean dot, we compare with the results of recent configuration-interaction calculations (MIKHAILOV, 2002a,b). For a dot with impurity, to date, there are no numerically exact results in the literature. We show that we can obtain high precision data for low temperatures with the Trotter extrapolation method and specify the details of our procedure.

Finally, in the last part we present the results of our PIMC study for a parabolic quantum dot with a single attractive impurity. We focus on the case of intermediate interaction where the Wigner crystallization sets in. This crossover regime is very difficult to treat numerically, and PIMC is probably the only method which can reliably resolve the tiny energy differences which determine the spin ordering and the addition energies. We investigate the effect of the impurity on ground-state energies and spins. Remnants of the energetic shell structure, which are seen despite of the relatively strong interaction, are washed out by the impurity. For $N = 8$, we find a new peak in the addition spectrum. Its appearance is accompanied by the transition to a very unexpected sub-Hund's rule spin $S = 0$. We discuss in detail the onset of Wigner crystallization for the six-electron Wigner molecule. The spin sensitivity of this process is significantly enhanced in the presence of the defect. We also consider

the behavior of the impurity's susceptibility which is reminiscent of the Kondo model.

3.1 Path-integral Monte Carlo

3.1.1 Monte Carlo method

The Monte Carlo (MC) technique is probably the most important and powerful computation method in statistical physics. Here, we briefly recall the idea of MC integration and refer to the literature for more complete introductions and reviews.

Often the expectation values that one wants to calculate in statistical or quantum mechanics are integrals of the form

$$I = \int d^d X \rho(\mathbf{X}) A(\mathbf{X}) = \langle A \rangle_\rho. \quad (3.1)$$

Here, \mathbf{X} is a microstate in a d -dimensional configuration space, and A is an observable, or, more generally speaking, a function whose average is calculated. It is calculated with respect to a weight function, a probability density $\rho(\mathbf{X})$ which is non negative $\rho(\mathbf{X}) \geq 0$ and normalized $\int d^d X \rho(\mathbf{X}) = 1$. A typical example is the energy of a classical gas of N particles at temperature $k_B T = 1/\beta$,

$$E = \langle H \rangle = \frac{1}{Z} \int d^3 r_1 \cdots d^3 r_N d^3 p_1 \cdots d^3 p_N H(\mathbf{P}, \mathbf{R}) e^{-\beta H(\mathbf{P}, \mathbf{R})}. \quad (3.2)$$

In order to perform the integration numerically in a direct way, e.g. with the Simpson rule, one has to sum up the integrand at a number of points which grows exponentially with d . This is impossible not only for a gas with $d \sim 10^{23}$ but for any system with many degrees of freedom, say $d \gtrsim 100$.

Also, the weight $\rho(\mathbf{X})$ will be very small in most parts of configuration space and thus give only very small contributions to the integral. Now, the idea of Monte Carlo integration is to sum up the integral (3.1) stochastically: The function A is evaluated at a number of configurations which are supposed to be the most important ones, yielding an estimate for I

$$\langle A \rangle_\rho^{\text{MC}} = \frac{1}{M} \sum_{i=1}^M A(\mathbf{X}_i) =: \mathcal{A}. \quad (3.3)$$

This *importance sampling* means that the $\mathbf{X}_1 \cdots \mathbf{X}_M$ are distributed according to $\rho(\mathbf{X})$. In the next section we will show how we can produce such a stochastic trajectory $\{\mathbf{X}_1, \dots, \mathbf{X}_M\}$ in configuration space.

Obviously, the number of points M should also be quite large and the points \mathbf{X}_i decorrelated. This is important when we want to estimate the error of the MC method: One can consider the \mathbf{X}_i and the $A(\mathbf{X}_i)$ as random variables. \mathcal{A} is an

estimator for I . It can be shown under quite general conditions¹ that \mathcal{A} is distributed according to a Gaussian with expectation value $\langle \mathcal{A} \rangle = I$, i.e.

$$P(\mathcal{A}) = \frac{1}{\sqrt{2\pi\sigma^2}} \exp \left\{ -\frac{(\mathcal{A} - I)^2}{2\sigma^2} \right\}. \quad (3.4)$$

The variance scales like M^{-1} times the variance of A ,

$$\sigma^2 = \frac{1}{M} \left\{ \langle A^2 \rangle_\rho - \langle A \rangle_\rho^2 \right\} = \frac{1}{M} \left\{ \frac{1}{M} \sum_{i=1}^M A(\mathbf{X}_i)^2 - \left(\frac{1}{M} \sum_{i=1}^M A(\mathbf{X}_i) \right)^2 \right\}. \quad (3.5)$$

The MC estimate for the integral (3.1) is therefore $I \approx \langle A \rangle_\rho^{\text{MC}} \pm \sigma$. The one-standard-deviation error bar is σ , thus the probability that the true value lies within this range is $\sim 68\%$. The probability that it lies within a two- σ range is $\sim 95\%$.

3.1.2 Markov chain and Metropolis algorithm

Now, one has to think about how to generate a stochastic trajectory $\{\mathbf{X}_1, \dots, \mathbf{X}_M\}$ where the \mathbf{X}_i are statistically independent and distributed according to $\rho(\mathbf{X})$. It turns out that this random walk through configuration space is basically a Markov process, i.e. a stochastic process where the probability to hop from \mathbf{X}_i to \mathbf{X}_{i+1} as the i -th step does not depend on the history of the process (see e.g. RÖMER and FILK, 1994). The statistical independence is important in order to obtain a correct estimate for the error bar. Furthermore the trajectory should in principle be able to reach every point in the configuration space. This is called ergodicity of the Markov process.

One can show that it is sufficient to require that the transition probabilities $W(\mathbf{X} \rightarrow \mathbf{X}')$ of the Markov process fulfill the condition of detailed balance (also called microreversibility)

$$W(\mathbf{X} \rightarrow \mathbf{X}')\rho(\mathbf{X}) = W(\mathbf{X}' \rightarrow \mathbf{X})\rho(\mathbf{X}'). \quad (3.6)$$

The proof can be found in the literature (e.g. NEGELE and ORLAND, 1988, p.408). Detailed balance means a dynamic equilibrium, namely that the process $\mathbf{X} \rightarrow \mathbf{X}'$ (i.e. being at \mathbf{X} and hopping to \mathbf{X}') has the same probability as the inverse process $\mathbf{X}' \rightarrow \mathbf{X}$.

The most important way to implement this random walk is the Metropolis method (METROPOLIS ET AL., 1953). It consists of two steps:

¹See e.g. NEGELE and ORLAND (1988). The underlying mathematical theorem is the central limit theorem. Actually, it is sufficient to require that the $A_i = A(\mathbf{X}_i)$ which are summed to \mathcal{A} are independent and identically distributed and have non-vanishing first and second momenta.

- First, starting from a configuration \mathbf{X}_i a new configuration \mathbf{X}' is proposed. This is often done in the following way: One chooses a component of \mathbf{X}_i at random, let's say the m -th component. Then $(\mathbf{X}_i)_m$ is updated,

$$(\mathbf{X}')_m = (\mathbf{X}_i)_m + r \Delta x, \quad \text{with } r \in [-1, 1]. \quad (3.7)$$

Here, r is an equally distributed random number² and $\Delta x > 0$ is a step-size which should be chosen appropriately³.

- Second, one decides whether to accept this proposed move. This is done by comparing the weights of \mathbf{X}' and \mathbf{X}_i . The new configuration is then

$$\mathbf{X}_{i+1} = \begin{cases} \mathbf{X}' & \text{if } \rho(\mathbf{X}')/\rho(\mathbf{X}_i) \geq s, \\ \mathbf{X}_i & \text{else.} \end{cases} \quad \text{with } s \in [0, 1], \quad (3.8)$$

One thus compares the ratio of the weights with an equally distributed random number s . Often $\rho(\mathbf{X}_i) \propto \exp(-\beta E_i)$ is just the Boltzmann factor. Then the Metropolis method means that the proposed step is accepted with probability one, if it lowers the energy. Else it is only accepted with probability $\exp[\beta(E_i - E')]$. One can check that this rule fulfills detailed balance.

The step-size Δx controls the ratio of accepted moves which should normally be adjusted to about 30% to make the sampling most effective. However, Δx must always be chosen large enough so that the MC trajectory can explore efficiently the full configuration space. This is important e.g. for tunneling processes.

In the MC simulation, one starts from an arbitrary configuration and iterates the Metropolis algorithm. A number of steps is necessary in order to reach detailed balance. This is called equilibration or thermalization. In general, a badly thermalized MC system can give biased data. In our simulation we checked that the energy has dropped to the expected range, which was typically achieved after a few steps ($\sim 1000d$ simple Metropolis steps).

3.1.3 Discretized path integral

Now we apply the MC method to finite-temperature quantum mechanics. The expectation value of an observable A in the canonical ensemble is given by

$$\langle A \rangle = \frac{1}{Z} \text{Tr}(A e^{-\beta H}) = \frac{1}{Z} \int A(\{\mathbf{x}\}) \langle \{\mathbf{x}\} | e^{-\beta H} | \{\mathbf{x}\} \rangle d\{\mathbf{x}\} \quad (3.9)$$

²In our simulation we use the minimal random generator of Park and Miller combined with a Marsaglia shift (PRESS ET AL., 1996) with a period of about 3×10^{18} .

³In a discrete problem, one for example flips a spin at a random lattice point.

with the partition function $Z = \text{Tr}(e^{-\beta H})$. The trace is performed in position space representation, thus $\{\mathbf{x}\} = \{\mathbf{x}_1, \dots, \mathbf{x}_N\}$ corresponds to the coordinates of all electrons and $d\{\mathbf{x}\} = d^2x_1 \cdots d^2x_N$. Further we have assumed that A is diagonal in that basis. This is the case throughout our simulation, but the approach can be easily generalized for an observable depending also on the momenta.

At this point we have to state an important remark about spin: without loss of generality, we take the first N_\uparrow electrons to have spin up, and the remaining $N_\downarrow = N - N_\uparrow$ to have spin down. We are thus working in the subspace of fixed total spin projection⁴ $S_z = (N_\uparrow - N_\downarrow)/2$. In other words, spin-up electrons are distinguishable from spin-down electrons⁵. This yields the problem of spin contamination: we do not have a true eigenstate of S_{tot} , but at finite temperature, each state with $S_{\text{tot}} \geq S_z$ contributes (see Sec. 3.1.7).

Now, we introduce the Trotter imaginary-time step size $\epsilon = \beta/P$. It holds $e^{-\beta H} = (e^{-\epsilon H})^P$. The construction of a discretized path-integral representation of (3.9) is obtained by inserting the identity operator

$$1_\alpha = \int d\{\mathbf{x}\}^\alpha |\{\mathbf{x}\}^\alpha\rangle\langle\{\mathbf{x}\}^\alpha| \quad (3.10)$$

at each discretization point (*time slice*) $\epsilon_\alpha = \alpha\epsilon$, where $\alpha = 1, \dots, P-1$, yielding

$$\langle A \rangle = \frac{1}{Z} \int d\{\mathbf{x}\}^1 \cdots d\{\mathbf{x}\}^P A(\{\mathbf{x}\}^1) \langle\{\mathbf{x}\}^1| e^{-\epsilon H} |\{\mathbf{x}\}^2\rangle \cdots \langle\{\mathbf{x}\}^P| e^{-\epsilon H} |\{\mathbf{x}\}^1\rangle. \quad (3.11)$$

We can also evaluate A at every time-slice which is done by replacing $A(\{\mathbf{x}\}^1)$ with $A[\mathbf{X}] = \sum_{\alpha=1}^P A(\{\mathbf{x}\}^\alpha)/P$. This improves both statistics and ergodicity. The expectation value (3.11) is a high-dimensional integral over $d = 2PN$ space coordinates in analogy to Eq. (3.1). We will calculate it by stochastic sampling on all the many-particle paths $\mathbf{X} = (\{\mathbf{x}\}^1 \cdots \{\mathbf{x}\}^P)$ with the MC technique.

3.1.4 Trotter break-up and short-time propagator

Unfortunately, in most cases the exact short-time propagator (also called high-temperature propagator) $\langle\{\mathbf{x}\}| e^{-\epsilon H} |\{\mathbf{x}\}'\rangle$ is not known. For sufficiently small ϵ and a Hamiltonian $H = H_1 + H_2$, one may use the following Trotter-Suzuki break-ups as approximants

$$\begin{aligned} \exp(-\epsilon H) &\simeq \exp(-\epsilon H_1) \exp(-\epsilon H_2) + \mathcal{O}(\epsilon^2) \\ &\simeq \exp(-\epsilon H_2/2) \exp(-\epsilon H_1) \exp(-\epsilon H_2/2) + \mathcal{O}(\epsilon^3). \end{aligned} \quad (3.12)$$

⁴Similar to Hartree-Fock but here we are dealing with an exact method for finite temperature.

⁵Another possibility would be to extend the trace in Eq. (3.9) also over all possible spin configurations (LYUBARTSEV and VORONTSOV-VELYAMINOV, 1993). Still another possibility would be to work in an ensemble of fixed total spin. This approach leads to particle statistics that have mixed symmetry (in general neither bosonic nor fermionic). It seems to make the sign problem worse, probably because then spin-up and down electrons are no longer distinguishable.

The first is called 'naive' break-up. We have employed the second which is symmetric and Hermitian⁶. In our case H_2 contains the Coulomb interaction and the impurity potential, and is diagonal in real space [see Eq. (2.6)]. We only need to evaluate the matrix elements of $\exp(-\epsilon H_1)$, where $H_1 = \sum_{i=1}^N h_i$ is the harmonic oscillator part (2.9). Taking into account the indistinguishability of equal-spin electrons and the Pauli principle, they read

$$\begin{aligned} \langle \{\mathbf{x}'\} | \exp(-\epsilon H_1) | \{\mathbf{x}\} \rangle &= \frac{1}{N_\uparrow! N_\downarrow!} \left[\sum_{\mathcal{P}_\uparrow} (-1)^{\text{sgn}(\mathcal{P}_\uparrow)} \prod_{j=1}^{N_\uparrow} \langle \mathbf{x}'_{\mathcal{P}_\uparrow(j)} | \exp(-\epsilon h) | \mathbf{x}_j \rangle \right] \\ &\times \left[\sum_{\mathcal{P}_\downarrow} (-1)^{\text{sgn}(\mathcal{P}_\downarrow)} \prod_{j=N_\uparrow+1}^N \langle \mathbf{x}'_{\mathcal{P}_\downarrow(j)} | \exp(-\epsilon h) | \mathbf{x}_j \rangle \right]. \end{aligned} \quad (3.13)$$

Here, $\mathcal{P}_\uparrow(j)$ denotes a permutation of the indices j associated with the spin-up electrons, and likewise for \mathcal{P}_\downarrow . In these expressions, the so-called Fock-Darwin propagator for zero magnetic field ($\Omega_c = 0$) reads (FEYNMAN, 1972, p.49)

$$\langle \mathbf{x}' | \exp(-\epsilon h) | \mathbf{x} \rangle = \frac{1}{2\pi \sinh(\epsilon)} \exp[-S_0(\mathbf{x}, \mathbf{x}')/\hbar] \quad (3.14)$$

with the classical action⁷

$$S_0 = \frac{\hbar}{2 \sinh(\epsilon)} \left\{ (\mathbf{x}^2 + \mathbf{x}'^2) \cosh(\epsilon) - 2\mathbf{x}\mathbf{x}' \right\}. \quad (3.15)$$

A more compact notation for the non-interacting short-time propagator follows by introducing the $N_\sigma \times N_\sigma$ matrices M^σ , where $\sigma = \uparrow$ and $\sigma = \downarrow$,

$$M_{ij}^\sigma = \langle \mathbf{x}'_i | \exp(-\epsilon h) | \mathbf{x}_j \rangle, \quad (3.16)$$

where the indices i, j run over the allowed labels for spin- σ electrons as defined above. The many-electron propagator is then a product of two determinants for spin up and down

$$\langle \{\mathbf{x}'_j\} | \exp(-\epsilon H_1) | \{\mathbf{x}_j\} \rangle = \det M^\uparrow \det M^\downarrow. \quad (3.17)$$

Since $\det M^\sigma$ can be negative we have to deal with the fermionic sign problem.

At this point two comments are in order: (i) Since the evaluation of determinants for large N becomes computationally rather expensive, one might be tempted to sample the permutations stochastically instead of summing them up analytically

⁶Both expressions are the same when they are put under the trace. A systematic study of the accuracy of different break-ups for simple quantum systems has been carried out by DE RAEDT and DE RAEDT (1983).

⁷Note that in the presence of a magnetic field the action S_0 becomes complex-valued (JONES and PAPADOPOULOS, 1971).

(i.e., computing the determinant). This will however worsen the sign problem. (ii) One does not have to keep the permutations at every time slice. The minimum requirement is to keep them at the time slices where observables are accumulated, and of course at least at one time slice. Unfortunately, it turns out that the sign problem behaves most favorably when the determinants are kept at every single time slice. The computational effort spent with computing determinants at every time slice is therefore worthwhile⁸.

The use of an approximate propagator introduces a systematic error in the PIMC simulation. One can try to make this error very small by choosing a very tiny Trotter discretization ϵ . A better way, however, to eliminate this error is to perform simulations for various rather large ϵ , and then extrapolate $\epsilon \rightarrow 0$, as we will explain in Sec. 3.3.

3.1.5 Path-integral ring polymer

Before we evaluate the many-electron path integral (PI) with the Monte Carlo technique, we want to remember an important interpretational analogy. For this we first forget about anti-symmetrization and consider the discretized PI for *distinguishable* quantum particles. For $\epsilon \rightarrow 0$, the action S_0 in (3.15) coincides with the so-called primitive approximation for the action

$$S_{\text{p.a.}} = \frac{\hbar\epsilon}{4} \left\{ \mathbf{x}^2 + \mathbf{x}'^2 + \frac{2(\mathbf{x} - \mathbf{x}')^2}{\epsilon^2} \right\} \quad (3.18)$$

which is obtained by applying (3.12) to the simple 2D oscillator. In this form it is easy to see that the expression in the exponent of the PI has the form of the potential energy of N interacting classical ring polymers

$$\langle A \rangle = \frac{1}{Z} \int d\{\mathbf{x}\}^1 \cdots d\{\mathbf{x}\}^P A(\{\mathbf{x}\}^1) e^{-\epsilon \sum_{\alpha=1}^P \frac{1}{2\epsilon^2} (\{\mathbf{x}\}^\alpha - \{\mathbf{x}\}^{\alpha+1})^2 + V(\{\mathbf{x}\}^\alpha) + W(\{\mathbf{x}\}^\alpha)}. \quad (3.19)$$

The trace leads to the boundary condition $\{\mathbf{x}\}^{P+1} \equiv \{\mathbf{x}\}^1$. This correspondence is called *quantum-classical isomorphism* (CHANDLER and WOLYNES, 1981). Each quantum particle is represented by a classical ring polymer with P beads. The spread of the ring is of the order of the thermal wavelength of the particle $\lambda_{\text{therm}} \sim \sqrt{\beta}$. The polymers interact in a peculiar way because only beads on the *same* time slice feel their mutual Coulomb repulsion W . All beads are subjected to the external potential V . Beads on *adjacent* time slices which form the ring interact via a harmonic force with spring constant $\propto \epsilon^{-2}$. This term comes from the kinetic energy of the original Hamiltonian. When choosing a very fine discretization, thus a small value for ϵ , the

⁸We use the BLAS and LINPACK routines in FORTRAN, which factor a matrix by Gaussian elimination.

ring polymer becomes very rigid. This can make it hard to sample the path integral ergodically.

Now, for identical particles one has to (anti-)symmetrize at least at one time slice. For example the boundary condition in Eq. (3.19) would be $\{\mathbf{x}\}^{P+1} = \mathcal{P}\{\mathbf{x}\}^1$, where \mathcal{P} is any permutation of N particles and one has to sum over all possible permutations⁹ with the appropriate sign for bosons and fermions. This leads to linked polymers, i.e. ring polymers of length nP , where n means an n -cycle permutation. The weight of these linked polymers in Eq. (3.19) is a measure for the importance of exchange, i.e. a measure of quantum degeneracy. For bosons, this exchange is crucial for superfluidity and Bose-Einstein condensation (see CEPERLEY, 1995). For fermions, the near cancellations of permutations with opposite sign make it difficult to sum up Eq. (3.19) which gives rise to the *fermion sign problem*. Before we explain this in more detail, we describe how important quantities are accumulated.

3.1.6 Monte Carlo observables

Most important is the virial estimator for the energy. It permits us to calculate the total energy as a function of space coordinates only, independent of momenta. Other quantities that we sample are directly accessible, e.g. the charge density,

$$n(\mathbf{r}) = \left\langle \sum_{i=1}^N \delta(\mathbf{r} - \mathbf{r}_i) \right\rangle, \quad (3.20)$$

is simply obtained by sampling the positions of all particles on all time slices. A more complete characterization of the density distribution is possible by means of the two-particle correlation function,

$$g(\mathbf{r}) = \frac{1}{N(N-1)} \left\langle \sum_{i \neq j=1}^N \delta(\mathbf{r} - \mathbf{r}_i + \mathbf{r}_j) \right\rangle, \quad (3.21)$$

which is normalized, $\int d^2r g(\mathbf{r}) = 1$. For the clean quantum dot both quantities (3.20),(3.21) are rotationally symmetric and can be sampled angle averaged in the PIMC. With impurity these densities have to be sampled on a 2D grid which requires very good statistics.

It is even more difficult to sample spin-dependent spatial functions like the spin density and spatial spin correlation functions: By the simple single-particle single-slice moves in our PIMC, spin is not driven very efficiently through configuration

⁹For a large number of particles, e.g. $N \sim 1000$, this summation cannot be done directly by building the determinant or the permanent. The MC random walk then has to go through configuration and permutation space.

space¹⁰. So, when we perform e.g. ten different runs, we get similar results for all observables, except for spatially spin depending ones. To control this error we compute the impurity spin, which is a space dependent observable

$$S_z^{\text{imp}} = \int d^2r S_z^{\text{imp}}(\mathbf{r}) = \int d^2r \delta_{\mathbf{r} \in B_\zeta(\mathbf{x})} S_z, \quad (3.22)$$

or the corresponding quantity for the center, S_z^c . For spin ergodicity, a small error bar for these local spins is mandatory. In particular, for unpolarized spin $S_z = 0$ the spin density should also vanish locally. We precise that we sample these local quantities, like (3.22) or the amount of charge accumulated at the impurity, directly in the MC in order to avoid the error related to the finite discretization size of the 2D grid for the corresponding densities.

Virial estimator for the energy

For the sake of completeness we first recall the Euler theorem (see e.g. COHEN-TANNOUDJI ET AL., 1977). Consider a homogeneous function f of degree s , i.e. $f(\gamma\mathbf{r}_1, \dots, \gamma\mathbf{r}_N) = \gamma^s f(\mathbf{r}_1, \dots, \mathbf{r}_N)$, then for its *virial* holds

$$\sum_{i=1}^N \mathbf{r}_i \cdot \frac{\partial f}{\partial \mathbf{r}_i} = s f(\mathbf{r}_1, \dots, \mathbf{r}_N). \quad (3.23)$$

This identity is very useful in the context of the virial theorem because the Coulomb and the harmonic potential are homogeneous functions.

The basic theorem which underlies the virial estimator is given by the so-called quantum-mechanical Hypervirial theorem of HIRSCHFELDER (1960) [see also HEINZE ET AL. (1997)]: Consider a Hamiltonian H and any linear operator W , both time-independent. The expectation value of the commutator $[H, W]$ in any stationary state vanishes,

$$\langle [H, W] \rangle = 0. \quad (3.24)$$

This is true for a pure state ($T = 0$) as well as for a mixed state (finite T). Now, the usual choice for W is the linear operator

$$W = \sum_{i=1}^N \mathbf{r}_i \cdot \mathbf{p}_i. \quad (3.25)$$

Note that W is not Hermitian. With the help of Eqs. (3.24) and (3.23) we obtain an expression for the ground state kinetic energy of the clean dot which does not

¹⁰In order to enhance spin ergodicity we also tried to include spin swap steps in the Metropolis algorithm by swapping the coordinates of two antiparallel spins on the same time slice. These steps do not change the energy, however, they are hardly ever accepted because they strain the springs of the ring-polymer.

depend on the momenta

$$\frac{1}{2} \left\langle \sum_{i=1}^N \mathbf{p}_i^2 \right\rangle = \frac{1}{2} \left\langle \sum_{i=1}^N \mathbf{r}_i^2 \right\rangle - \frac{1}{2} \left\langle \sum_{i<j}^N \frac{\lambda}{|\mathbf{r}_i - \mathbf{r}_j|} \right\rangle. \quad (3.26)$$

This equation holds also in presence of a transversal magnetic field but is no longer of any use since then there is an additional term proportional to the total angular momentum [see (2.6)] which is not diagonal in real space. In the presence of a Gaussian impurity (2.16), the following term has to be added to the right-hand-side of (3.26):

$$\left\langle \frac{w}{2\sigma^2} \sum_{i=1}^N \mathbf{r}_i \cdot (\mathbf{r}_i - \mathbf{x}) \exp \left\{ \frac{-(\mathbf{r}_i - \mathbf{x})^2}{2\sigma^2} \right\} \right\rangle. \quad (3.27)$$

The advantage of the virial estimator is that we can sample the total energy on a single time slice. We also want to mention that the averages in (3.26) and (3.27) can be formulated with the one- and two-particle densities. For example we can write the expectation value of the Coulomb energy as an integral over the two-particle correlation function (3.21),

$$\left\langle \sum_{i<j}^N \frac{\lambda}{|\mathbf{r}_i - \mathbf{r}_j|} \right\rangle = \frac{N^2 - N}{2} \int d^2r \frac{\lambda}{|\mathbf{r}|} g(\mathbf{r}). \quad (3.28)$$

In this fashion (with spin dependent densities) HARTING ET AL. (2000) formulate their Hypervirial estimator, which is nothing else than the normal virial estimator. For a discretized PI derivation of the virial estimator see CEPERLEY (1995).

Thermodynamic estimator

Another estimator for the energy can be derived from the thermodynamic dependence

$$E(N) = -\frac{\partial}{\partial \beta} \ln Z(N). \quad (3.29)$$

This yields an expression which contains the fermion determinants. Its accumulation is thus computationally more expensive. The thermodynamic estimator has to be employed when a finite magnetic field is included, since there is no virial expression for the kinetic energy in the presence of a magnetic field. For $B=0$, within statistical noise, this estimator yields the same results as the virial estimator. However, its variance is larger because its fluctuations scale $\propto \tau^{-2}$.

3.1.7 Spin contamination

Note that at $T=0$ for a superposition of two energy eigenstates $|\Psi\rangle = \alpha|1\rangle + \beta|2\rangle$, Eq. (3.24) does not hold,

$$\langle \Psi | [H, W] | \Psi \rangle = 2i(E_1 - E_2) \text{Im}(\alpha^* \beta \langle 1 | \mathbf{p} \cdot \mathbf{r} | 2 \rangle). \quad (3.30)$$

Still, we are doing the PIMC in the canonical ensemble and (3.24) does hold for the mixed state

$$\rho = \frac{1}{Z}(e^{-\beta E_1} |1\rangle\langle 1| + e^{-\beta E_2} |2\rangle\langle 2|) . \quad (3.31)$$

This is important in the context of 'spin-contamination': Since the PIMC proceeds at fixed S_z^{tot} , the calculated energy receives contributions from higher spins at finite temperatures [cf. erratum to EGGER ET AL. (1999)]. For example when we want to calculate the two-electron ground state which is a singlet, in (3.31) we have $|1\rangle = |S^{\text{tot}} = 0, S_z^{\text{tot}} = 0\rangle$ and $|2\rangle = |S^{\text{tot}} = 1, S_z^{\text{tot}} = 0\rangle$. In fact not only these two but all the states with higher energy and $S_z^{\text{tot}} = 0$ contribute. This difference to the true singlet (which receives contributions only from the $S^{\text{tot}} = 0$ states) vanishes when T goes to zero. We give a detailed discussion of spin contamination in Sec. 3.2.3 when we compare exact diagonalization at finite T and PIMC. Summarizing, we can say that the virial estimator is exact also for spinful electrons and it has the same spin contamination problem as, e.g., the thermodynamic estimator.

3.1.8 Fermionic sign problem

As already pointed out, due to the anti-symmetry principle for fermions, the weight, i.e. the product of propagators in Eq. (3.11) can be negative. Thus we cannot sample $A[\mathbf{X}]$ directly, but we have to use a reweighting technique. This is in general done as follows. Another normalized positive weight $W(\mathbf{X})$ is inserted in the integral expression (3.1)

$$\langle A \rangle_\rho = \int d^d X W(\mathbf{X}) \frac{\rho(\mathbf{X})}{W(\mathbf{X})} A(\mathbf{X}) = \left\langle A \frac{\rho}{W} \right\rangle_W . \quad (3.32)$$

Now, the importance sampling according to W will be very effective if W and ρ are distributions of a similar form. Otherwise the sampling will be suboptimal with a larger variance for the MC estimate $\langle A \rangle_W^{\text{MC}}$.

Specifically, for the fermionic PIMC, the usual choice for the non-negative weight in order to sample Eq. (3.11), is to take the absolute value of all the propagators¹¹

$$W[\mathbf{X}] = |\langle \{\mathbf{x}\}^1 | e^{-\epsilon H} | \{\mathbf{x}\}^2 \rangle \cdots \langle \{\mathbf{x}\}^P | e^{-\epsilon H} | \{\mathbf{x}\}^1 \rangle| . \quad (3.33)$$

The expectation value (3.11) now reads ($d = 2PN$)

$$\langle A \rangle = \frac{\int d^d X A[\mathbf{X}] \Phi[\mathbf{X}] W[\mathbf{X}]}{\int d^d X \Phi[\mathbf{X}] W[\mathbf{X}]} = \frac{\langle A \Phi \rangle_W}{\langle \Phi \rangle_W} , \quad (3.34)$$

¹¹Actually it is very advantageous that this weight factorizes. So, when we change the electron positions on a single time slice, we do not have to recompute the whole product but only *two* short-time propagators.

where we have also introduced the *sign of the path* \mathbf{X}

$$\Phi[\mathbf{X}] = \text{sgn}(\langle\{\mathbf{x}\}^1| e^{-\epsilon H} |\{\mathbf{x}\}^2\rangle \dots \langle\{\mathbf{x}\}^P| e^{-\epsilon H} |\{\mathbf{x}\}^1\rangle) = \pm 1. \quad (3.35)$$

This is exactly the quotient in Eq. (3.32) and is oscillatory. The MC estimate for A now reads

$$\langle A \rangle^{\text{MC}} = \frac{\sum_i A[\mathbf{X}_i] \Phi[\mathbf{X}_i]}{\sum_i \Phi[\mathbf{X}_i]}, \quad (3.36)$$

where the \mathbf{X}_i are distributed according to W . Note that W is not normalized but the normalization cancels out in Eqs. (3.34), (3.36).

The problem arises now because of the numerator: we will show that the expectation value of the sign (with respect to W) vanishes exponentially with inverse temperature β and electron number N whereas its variance increases exponentially (see e.g. HATANO and SUZUKI, 1993; CEPERLEY, 1996). For this we can introduce a partition function Z' for the system with weight W and the corresponding free energy $F' = -\ln(Z')/\beta$ and write

$$\langle \Phi \rangle_W = \frac{Z}{\int d^d X W[\mathbf{X}]} = \frac{Z}{Z'} = e^{-\beta(F-F')}, \quad (3.37)$$

where F is the free energy for the true fermion system. When permutations are also sampled stochastically and thus W is simply the unsymmetrized propagator for boltzmanons, F' is the free energy of the boson system. Consequently, also the relative error of the sign increases exponentially,

$$\sqrt{\langle \Phi^2 \rangle_W / \langle \Phi \rangle_W^2 - 1} \approx e^{\beta(F-F')} \quad (3.38)$$

with inverse temperature and, due to the extensivity of the free energy, also with particle number.

The sign problem is a serious limitation in many-fermion MC, see e.g. LOH JR. ET AL. (1990) for lattice fermions. The same problem is encountered in $T = 0$ diffusion Monte Carlo for fermion systems. It occurs also in real time dynamical PIMC simulations, where the propagator is complex. Recently, MAK ET AL. (1998) have proposed a Multilevel Blocking (MLB) algorithm to alleviate the sign problem. It relies on the idea that the sign problem is weak for small systems (i.e. small N, β). Blocking paths into small groups and then sampling over these blocks can therefore improve the sign. The MLB method is a hierarchical, recursive implementation of this concept. For a comprehensive introduction to MLB, see DIKOVSKY and MAK (2001). MLB has been used for clean quantum dot by EGGER ET AL. (1999). In the present thesis, however, we use the conventional approach which allows us to choose an arbitrary P for the Trotter extrapolation and to sample the imaginary-time spin correlation function. Other methods avoid the fermion sign problem by making an assumption about the nodes of the wave-function like e.g. the restricted

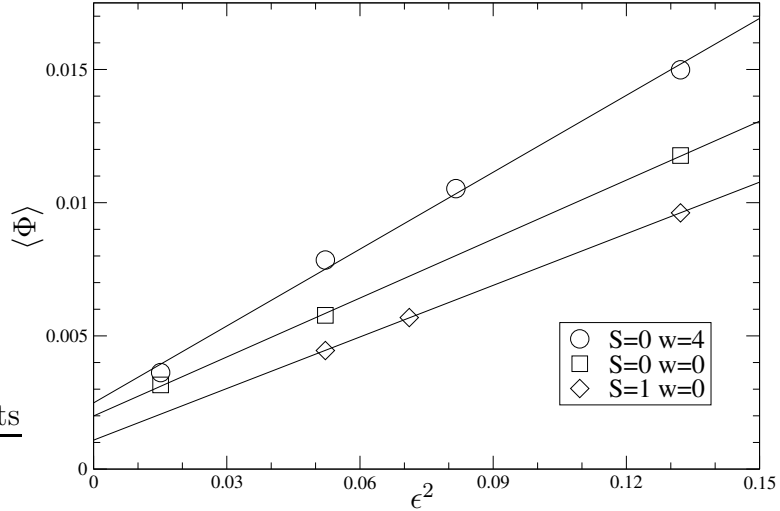


Fig. 3.1: PIMC sign $\langle \Phi \rangle$ of ten interacting electrons in a 2D oscillator at finite temperature $\beta = 8$ versus values of $\epsilon^2 = (\beta/P)^2$ and linear regression fit. Error bars are of symbol size.

PIMC (CEPERLEY, 1996) or the variational and fixed-node diffusion MC (FOULKES ET AL., 2001). By this assumption the methods lose their exactness but still give upper bound limits for the true ground-state energies. In fact QMC methods often give benchmark results for other, computationally less demanding calculations. They are successfully applied in many fields of quantum chemistry and solid state physics, e.g. for the simulation of fundamental systems like the electron gas or condensed Helium (CEPERLEY, 1995).

The sign $\langle \Phi \rangle_W$ has a physical meaning: It measures the difference between bosons and fermions, and so it is also a measure of quantum effects. In Sec. 3.2.2, we derive the partition functions for two non-interacting bosons/fermions in a 2D oscillator. Building the quotient yields the sign

$$\langle \Phi \rangle_W = \frac{Z_F}{Z_B} = \frac{1}{\cosh(\beta)} \quad (3.39)$$

which in fact vanishes exponentially with β . For very high temperatures, there is no difference between bosons and fermions.

In our simulation, however, W is the absolute value of the anti-symmetrized propagator, so our $\langle \Phi \rangle$ does not directly have that meaning. In Fig. 3.1 we show that instead our $\langle \Phi \rangle$ depends strongly on P : it converges $\propto \epsilon^2$ [cf. Sec. 3.3]. In the other case, $\langle \Phi \rangle = Z_F/Z_B$ would be expected to depend rather weakly on P .

Finally, in Fig. 3.2, we illustrate how $\langle \Phi \rangle$ decays exponentially with the number of electrons. One can see that the sign is worse for higher spin because there are more indistinguishable (equal spin) electrons. The impurity slightly improves the behavior of the sign, making the system more classical (cf. Fig. 3.1).

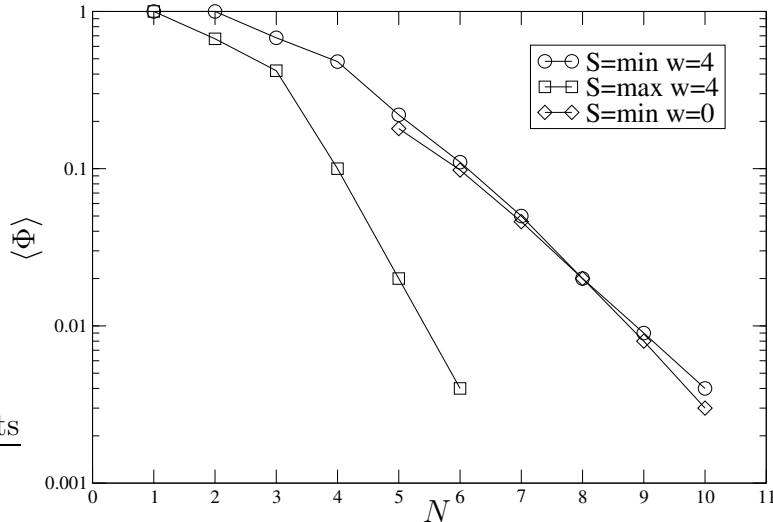


Fig. 3.2: PIMC sign $\langle \Phi \rangle$ of up to ten interacting electrons in a 2D oscillator at finite temperature $\beta = 8$ with and without impurity; $P = 65$. Error bars are of symbol size.

3.1.9 Monte Carlo error bars

Since Monte Carlo integration is a stochastic method, the proper determination of the statistical error is very important. This error bar then tells us up to which degree we can be confident in the numerical precision of the result. The naive error estimate from the variance (3.5) is only correct if the measurement points $A_i = A(\mathbf{X}_i)$ ($i = 1, \dots, M$) of the MC sampling are completely decorrelated, i.e. statistically independent.

In our program the sampling is done as follows: In a single Metropolis sweep, we only change the coordinates of one arbitrary particle on one arbitrary time slice. A single MC sweep then consists of $d = 2PN$ (the dimensionality of configuration space) simple Metropolis sweeps, so that on average we have changed every coordinate of the whole many-electron path. Only after a number M_{out} of MC sweeps the observables are accumulated. The total number of MC steps is thus $M_{\text{tot}} = MM_{\text{out}}$. Thus, if the number of intermediate steps M_{out} between two measurements A_i and A_{i+1} is large enough, one obtains uncorrelated measurements.

It is difficult though to determine the proper decorrelation length M_{out} which also might be depending on the observables under consideration. On the other hand, a too high value for M_{out} means a waste of computation time. This problem of proper determination of error bars is extensively discussed in the literature about statistics and the MC method. For a nice review which is illustrated for the Ising model, see JANKE (2002). Here, we want to present shortly three ways in which we have handled the problem. The first is to analyze the time series A_i and to calculate the

normalized auto-correlation function of the observable,

$$c_k = \frac{1}{\sigma^2} \left\{ \frac{1}{M-k} \sum_{i=1}^{M-k} A_i A_{i+k} - \left(\frac{1}{M} \sum_{i=1}^M A_i \right)^2 \right\}, \quad (3.40)$$

where $c_0 = 1$ and $0 < k \ll M$. It decays roughly exponentially $c_k \sim \exp -k/\tau$ and the so-called integrated auto-correlation time is

$$\tau_{\text{corr}} = \sum_{k=1} c_k + \frac{1}{2} \approx \tau - \frac{1}{2}. \quad (3.41)$$

The naive error estimate (3.5) is correct if $\tau_{\text{corr}} = 1/2$. In general, it can be shown that the corrected variance which takes the correlation length into account is given by

$$\sigma_{\text{corr}}^2 = 2\tau_{\text{corr}} \sigma^2. \quad (3.42)$$

In Fig. 3.3(a) we show a MC time series for the energy of two electrons (singlet) in a quantum dot. The average with the naive error estimate is 3.70(1). Here, the bracketed number stands for the error in the last digits, i.e. 3.70 ± 0.01 . The corresponding auto-correlation function [Fig. 3.3(c)] gives $2\tau_{\text{corr}} \approx 9$, thus the result with correct error bar is 3.70(3).

A second method to obtain correct error bars from correlated data is the blocking or binning technique. For the blocking technique of FLYVBJERG and PETERSEN (1989), the length of the MC trajectory is chosen to be $M = 2^L$. Then, on $L - 1$ levels, new series $\{A_i^{(l)}\}$ with length $M/2, M/4, \dots$ are recursively built by taking the arithmetic mean of two adjacent points as a new point,

$$A_i^{(l+1)} = \frac{1}{2} \left(A_{2i-1}^{(l)} + A_{2i}^{(l)} \right), \quad l = 0, \dots, L - 1. \quad (3.43)$$

These points are more and more decorrelated, and should approach independent Gaussian variables as the blocking level l increases. The mean of the whole series remains the same, but its error can be correctly estimated. In Fig. 3.3(d) the result of such a blocking is shown. From level $l = 5$ on, the standard deviation $\sigma_{\text{corr}}^{(l)}$ is constant. Note that the error bar of the standard deviation is increasing, because the size of the sample is decreasing $M/2, M/4, \dots$. Thus the error bar is also 0.03, in consistence with the previous analysis.

The third method, which is also a kind of block building, has been adopted for most of our calculations. In fact since we have to deal with the sign-problem we are always accumulating the sign Φ and observables $A = A'\Phi$. The final result is the quotient of the estimates for these two. A thorough analysis should investigate the auto-correlation of Φ , A and their cross-correlation. However, we choose a simpler way: We run a number of independent identical simulations (usually ten) in parallel

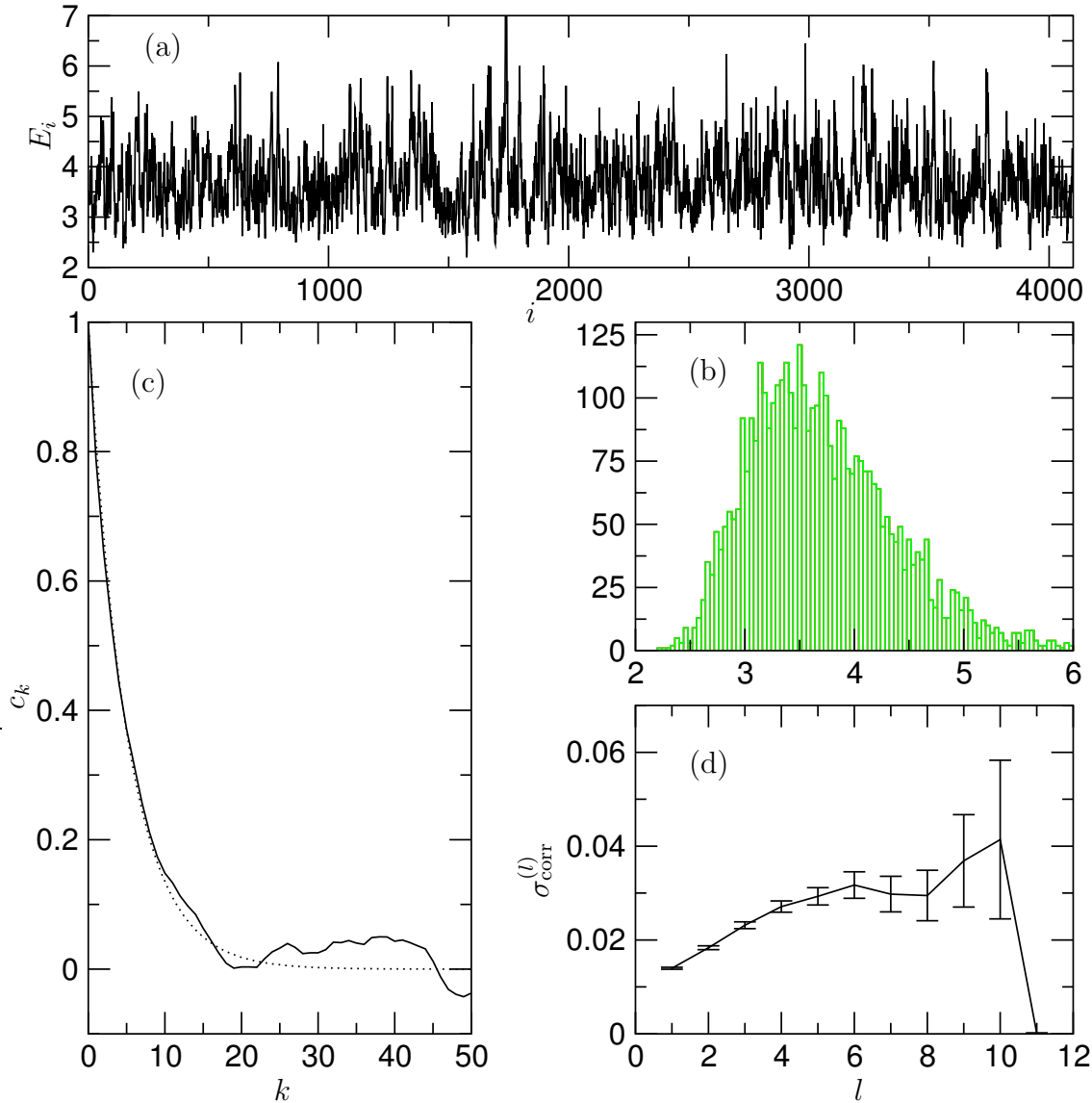


Fig. 3.3: Statistical analysis of MC data obtained for $N = 2$, $S = 0$, $\beta = 6$, $P = 80$ with the permanent propagator (cf. Sec. 3.2.3). The energy was accumulated after every $M_{\text{out}} = 50$ -th step. (a) MC data for the energy E_i with $i = 1, \dots, M = 4096$. (b) Histogram for E_i . (c) Auto-correlation function c_k (straight line), which is roughly exponential $c_k \sim \exp(-k/5)$ (dotted). (d) Standard deviations of blocked data (see text).

and then estimate the error bar from the fluctuations of these uncorrelated results. As the accumulation does not take much computer time, we choose a rather low $M_{\text{out}} = 20$. Also all the accumulated densities are the means of these different runs. We estimate their errors by integrating over a circle at the center or at the impurity and check the error of these integrals.

3.2 Tests for the PIMC simulation

In order to perform a check for the validity of our PIMC simulation we have obtained analytical and independent numerical results. For the isotropic clean two-electron quantum dot, we have first calculated analytically the energies for zero interaction. Furthermore, we have performed an exact diagonalization for finite temperature. These first tests give us a better understanding of our system, e.g. in view of the spin contamination problem, and show that we can produce high accuracy PIMC results for arbitrary interaction and temperature.

3.2.1 Isotropic clean quantum-dot Helium

The Hamiltonian for an isotropic clean quantum dot with two electrons is

$$H_{\text{QHe}} = \sum_{i=1,2} \left(\frac{\mathbf{p}_i^2}{2m^*} + \frac{1}{2}m^*\omega_0^2\mathbf{x}_i^2 \right) + \frac{e^2/\kappa}{|\mathbf{x}_1 - \mathbf{x}_2|}. \quad (3.44)$$

This so-called quantum-dot Helium has been studied by many authors, first by MERKT ET AL. (1991). We will also discuss it later in the (un)restricted Hartree-Fock approximation (Sec. 4.2). Now we transform according to

$$\begin{aligned} \mathbf{r} &= \mathbf{x}_1 - \mathbf{x}_2, & \mathbf{p} &= \frac{1}{2}(\mathbf{p}_1 - \mathbf{p}_2), \\ \mathbf{R} &= \frac{1}{2}(\mathbf{x}_1 + \mathbf{x}_2), & \mathbf{P} &= \mathbf{p}_1 + \mathbf{p}_2. \end{aligned} \quad (3.45)$$

The Hamiltonian separates into two parts which represent the relative and the center-of-mass motion,

$$H_{\text{QHe}} = H_R + H_r. \quad (3.46)$$

Remarkably, the center-of-mass part is a harmonic oscillator

$$H_R = -\frac{\hbar^2}{2M}\Delta_R + \frac{M}{2}\omega_0^2\mathbf{R}^2 \quad (3.47a)$$

with $M = 2m^*$ and for the relative motion we have

$$H_r = -\frac{\hbar^2}{2\mu}\Delta_r + \frac{\mu}{2}\omega_0^2\mathbf{r}^2 + \frac{e^2}{\kappa r} \quad (3.47b)$$

with the reduced mass $\mu = \frac{m^*}{2}$. The problem is thus classically integrable because the angular momenta of relative and c.m. parts are constants of motion. Equation (3.47b) reads in oscillator units [see Eqs. (2.5)]

$$h_r = -\frac{1}{2}\Delta_r + \frac{1}{2}\mathbf{r}^2 + \frac{\lambda_r}{r}, \quad (3.48)$$

where $\lambda_r = \frac{e^2 \mu_r}{\kappa \hbar^2} = \frac{\lambda}{\sqrt{2}}$ is the coupling constant and the oscillator length is $l_r = \sqrt{\frac{\hbar}{\mu\omega_0}} = \sqrt{2}l_0$. The eigenfunctions of (3.48) can be expanded in terms of harmonic oscillator functions (2.10) with fixed angular momentum M^{rel} . Now it is important to think about anti-symmetry: One combines odd $M^{\text{rel}} = \pm 1, \pm 3, \dots$ with a spin singlet and even $M^{\text{rel}} = 0, \pm 2, \pm 4, \dots$ with a spin triplet state. The problem can now be solved by an exact diagonalization¹² of h_r . The matrix elements $\langle nM | r^{-1} | n'M \rangle$ of the Coulomb potential are obtained with a Gauss-Legendre quadrature (REUSCH, 1998). However, before giving results with interaction, we also want to include finite temperatures.

3.2.2 Finite temperature, zero interaction

Here, we want to derive briefly partition functions for two non-interacting electrons in a harmonic potential. These expressions serve as a check for the exact diagonalization at finite temperature and the PIMC. The separation of relative and c.m. motion is also useful in this context. The total partition function factorizes $Z^{\text{tot}} = Z^{\text{c.m.}} Z^{\text{rel}}$. Now $Z^{\text{c.m.}}$ is the partition function of a normal 2D oscillator (2.9)

$$Z^{\text{c.m.}} = \text{Tr}(e^{-\beta h}) = \sum_{\substack{n=0,\infty \\ M=-\infty,\infty}} e^{-\beta(2n+|M|+1)} = [2 \sinh(\beta/2)]^{-2}. \quad (3.49)$$

For the relative motion we have to distinguish the singlet and triplet contributions, thus the sum of the trace extends only over odd or even M which gives

$$Z_{\text{sin}}^{\text{rel}} = \frac{\cosh(\beta)}{2 \sinh^2(\beta)}, \quad Z_{\text{tri}}^{\text{rel}} = \frac{1}{2 \sinh^2(\beta)}. \quad (3.50)$$

These expressions can also be obtained with the Fock-Darwin propagator (3.14) in the (anti)-symmetric two-particle coordinate space. In fact, the two cases correspond to two spinless bosons for the singlet and fermions for the triplet. However, the PIMC for $S_z = 0$ works in the product Hilbert space of two distinguishable particles (boltzmanons). In this third case the total partition function is just the product of two normal 2D oscillators

$$Z^{\text{tot}} = [2 \sinh(\beta/2)]^{-4}. \quad (3.51)$$

The total energy is then given by $E = -\partial/\partial\beta \ln Z^{\text{tot}}$. In Fig. 3.4 we show the analytic dependence of the energies for the three cases and compare with the numerical results of the PIMC. One sees that the PIMC works correctly for zero interaction¹³. The

¹² We mention that for special values of λ_r , exact analytical solutions for the Hamiltonian (3.48) were given by TAUT (1993).

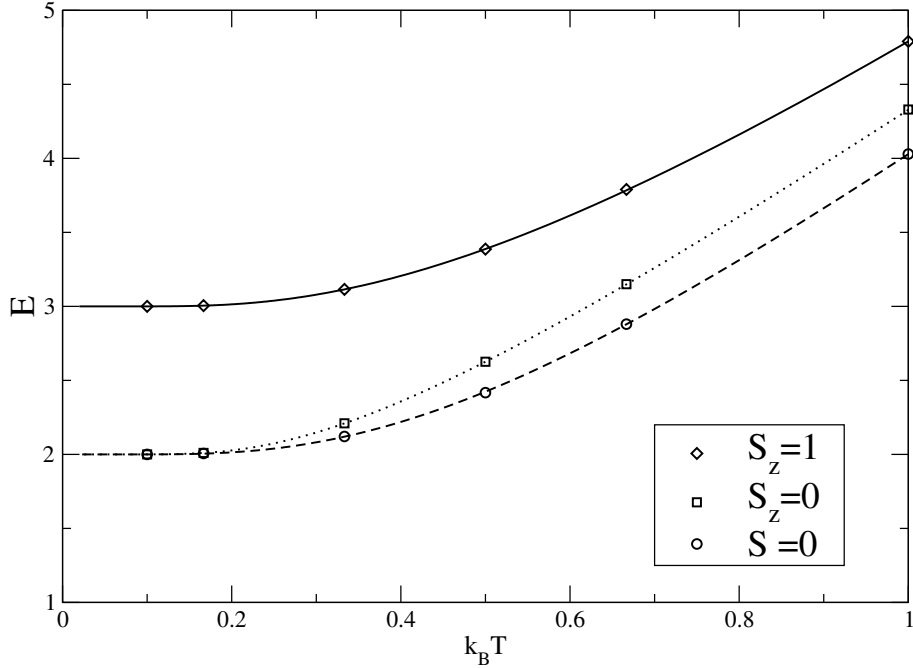


Fig. 3.4: Energies of two non-interacting electrons in a 2D oscillator at finite temperature. We show the analytic dependence (drawn lines) and PIMC results (symbols) for three different spin states. The error bars for the PIMC are smaller than the symbol size.

virial and the thermodynamic energy estimators give the same results in all three cases. At higher temperatures $\beta \lesssim 5$, the $S = 0$ state lies somewhat lower than the $S_z = 0$ state, because the latter receives contributions from the triplet state with $S_z = 0$. This is exactly the problem of spin contamination mentioned above. For two electrons, we can easily obtain the correct $S = 0$ ground state by taking the permanent in the PIMC. For higher electron numbers and not fully polarized spin, e.g. $N = 3$, $S = 1/2$, this approach can be generalized, but has to include a more elaborate group-theoretical analysis (LYUBARTSEV and VORONTSOV-VELYAMINOV, 1993). In our PIMC, we only anti-symmetrize for equal spin electrons [cf. Eq. (3.17)].

3.2.3 Finite temperature, non-zero interaction

The next check for the PIMC is for non-zero interaction. Exact diagonalization data are obtained with the help of the spectrum of the Hamiltonian for the relative motion (3.48). h_r has eigenstates with good relative angular momentum M , thus its eigenenergies can be labeled $\tilde{\epsilon}_{nM}$. The total energy for two interacting electrons then

¹³ Remember that without interaction there is no Trotter discretization error since we are working with the exact propagator for the 2D oscillator.

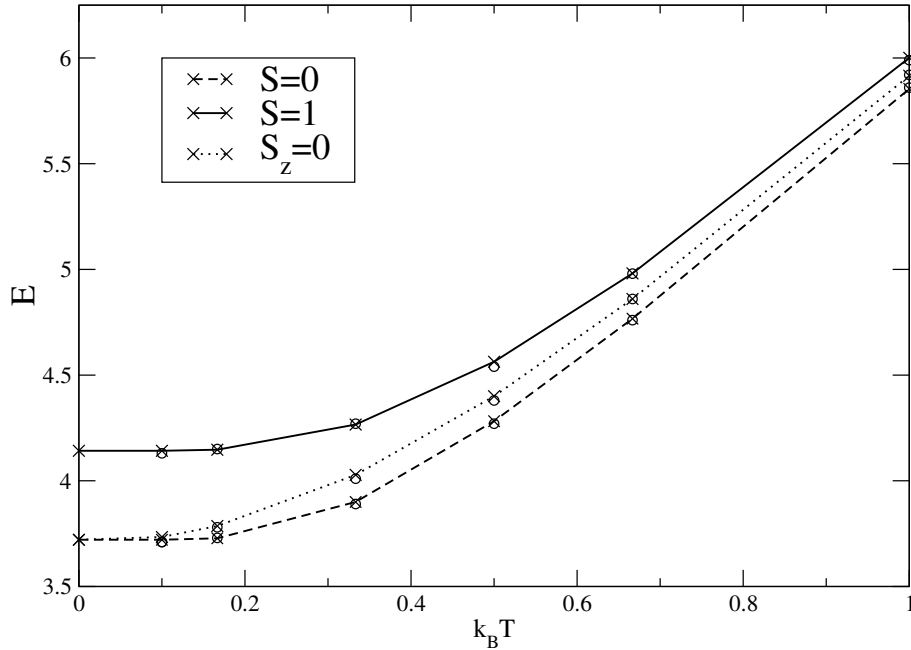


Fig. 3.5: Energies of two interacting electrons in a 2D oscillator at finite temperature and $\lambda = 2$. Exact diagonalization data (\times , lines are guides to the eye only) and PIMC results (\circ) for the three spin states. The error bars for the PIMC are of the order of the symbol size.

reads

$$E = \coth(\beta/2) + \frac{1}{Z^{\text{rel}}} \sum_{\substack{n=0,\infty \\ M=-\infty,\infty}} \tilde{\varepsilon}_{nM} e^{-\beta \tilde{\varepsilon}_{nM}}, \quad (3.52)$$

where the first term is the energy of the c.m. motion and $Z^{\text{rel}} = \sum_{nM} e^{-\beta \tilde{\varepsilon}_{nM}}$. Now, as above for the $S_z = 0$ state the sum extends over all M , whereas for the singlet it extends only over the even M and for the triplet only over the odd M . To ensure convergence we included states with $n < 110$ and $|M| \leq 8$ in the sum (3.52).

In Fig. 3.5 we show the agreement between exact and PIMC data for a relatively small coupling constant $\lambda = 2$. Again for the singlet, the PIMC works with the permanent (corresponding to bosons), for $S_z = 0$ with the product propagator (boltzmanons) and for the triplet with the determinant (spinless fermions). Here, Trotter convergence has to be achieved (see Sec. 3.3). All the results in this section have been obtained with the virial estimator [see Eq. (3.26)]. The spin contamination problem is clearly visible: For $\beta = 10$, the energy of the $S_z = 0$ state is 0.4% higher than the energy of the singlet, while for $\beta = 6$, the difference is already 1.6%.

We also show similar results for stronger interaction $\lambda = 6, 8$ in Fig. 3.6, which also demonstrates the good agreement between diagonalization and PIMC.

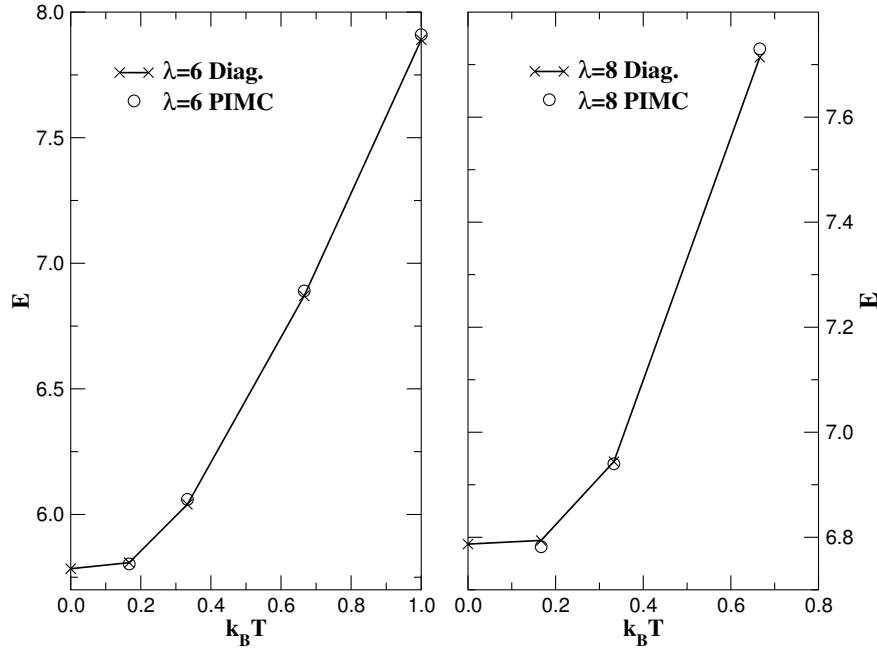


Fig. 3.6: Energies of two interacting electrons in a 2D oscillator at finite temperature. Exact diagonalization data (\times , lines are guides to the eye only) versus PIMC results (\circ) for two cases: $S = 0$ (permanent propagator) and $\lambda = 6$ (left); and $S = 1$ (determinant), $\lambda = 8$ (right). The error bars for the PIMC are of the order of the symbol size.

3.3 Trotter convergence

3.3.1 Trotter convergence for clean quantum-dot Helium

As already mentioned in Sec. 3.1.4, the PIMC results are essentially exact if the Trotter break-up has been done for a small enough imaginary-time step $\epsilon = \beta/P$. Else this approximation introduces a systematic error in the data, the so-called Trotter error, in addition to the statistical error due to the MC method.

One way to cope with this problem is to produce results (with very good statistics) for higher and higher P and check if the systematic error has vanished, i.e. if the result stays the same. For the results in the previous section, Trotter convergence has been achieved in order to obtain high precision data, with relative errors in the energy of a few per mill. However, the Trotter numbers for the three different spin states differ strongly. For $\beta = 10$ and $\lambda = 2$ convergence has been achieved for Trotter numbers

- $P = 133$ for $S = 0$ (permanent propagator)
- $P = 100$ for $S_z = 0$ (product propagator)
- $P = 30$ for $S = 1$ (determinant propagator)

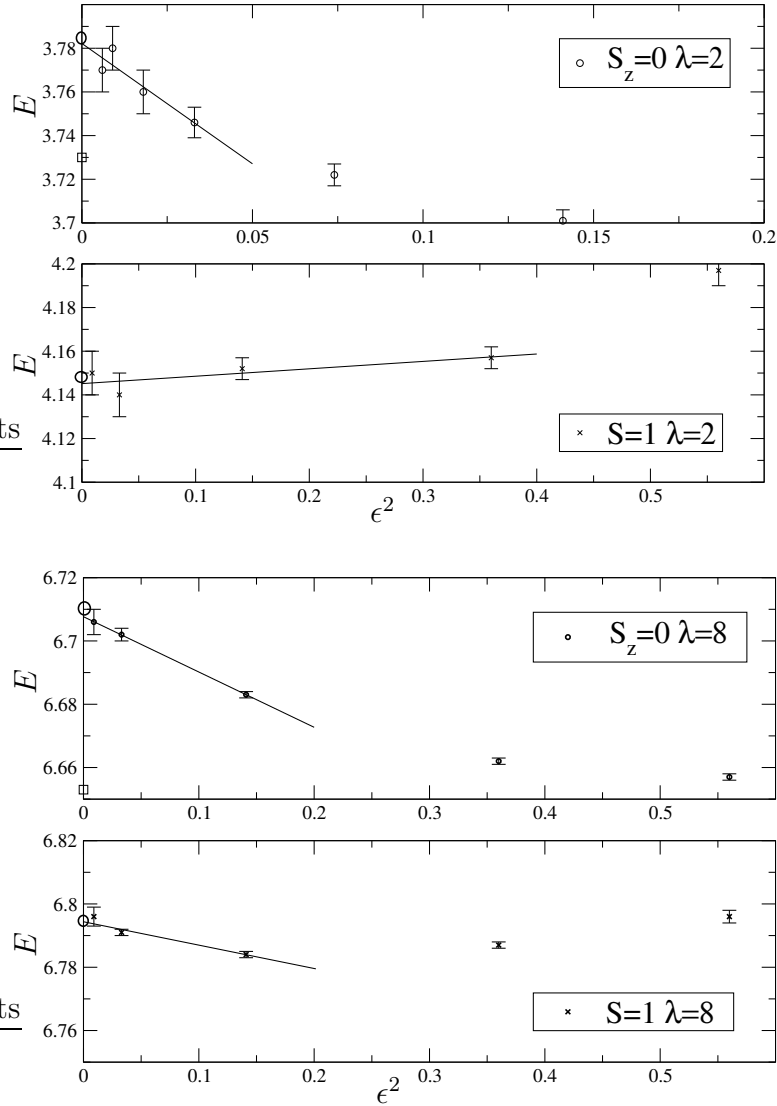


Fig. 3.7: Trotter convergence of the energy of clean quantum-dot Helium at finite temperature $\beta = 6$. The finite Trotter step size is $\epsilon = (\beta/P)$. For two different interaction strengths $\lambda = 2$ (up) and 8 (down) and different spins we show exact diagonalization data (\circ , for $\epsilon = 0$) and PIMC results (with error bars). For small enough ϵ , a linear regression has been performed, to extrapolate the PIMC results. Exact values for $S = 0$ (\square) illustrate the problem of spin contamination.

Convergence for other temperatures is obtained by keeping $\epsilon = \beta/P$ constant (except for $\beta = 1$, where we choose a slightly higher P).

A more systematic method consists in eliminating the Trotter error by an extrapolation. It was shown by FYE (1986) that under very general conditions for a Hermitian observable, the error resulting from the discretized PI with second-order Trotter break-up (3.12) should scale as ϵ^2 for $\epsilon \rightarrow 0$. This might be verified e.g. for

the single harmonic oscillator, where this Trotter error can be calculated analytically (SCALETAR, 1999). Fortunately, for the clean dot with small electron number, we also have exact data to compare.

We illustrate this convergence behavior in Fig. 3.7, showing the PIMC energy versus ϵ^2 for two different interaction strengths and two spin polarizations. Within two standard deviations (two error bars), for low enough ϵ , the data fit on a line which goes through the exact value ($\epsilon = 0$) obtained with finite-temperature exact diagonalization. From the slopes of the different lines, one clearly notices that convergence is very slow for the $S_z = 0$ and $\lambda = 2$ state (note the different x-axis scale). Thus, building the determinant seems to enhance convergence, whereas the product (or permanent) propagator seems to give a worse approximation for the interacting two-particle propagator.

In the graph for $S_z = 0$, $\lambda = 2$, we also plot the exact energy for $S = 0$, which is 1.6% lower than the spin contaminated $S_z = 0$ energy. This may induce one to underestimate the Trotter convergence. Interestingly, for $S = 1$, the energy converges from above¹⁴ giving thus too high energies for too small P . In contrast, for $S = 0$ and $S_z = 0$, one obtains too low energies for small P . This latter fact is unpleasant because we do not have upper bounds to the true energy.

Finally, it is quite surprising that convergence for stronger interaction $\lambda = 8$ (Fig. 3.7) is obtained for lower Trotter numbers than for $\lambda = 2$. One would expect that higher P are necessary for the Trotter break-up at stronger interactions, because naively, the error should scale as $\lambda\epsilon^2$. For $\lambda = 8$ and $S = 1$ the convergence is very smooth (consider the small error bars) from below but for higher ϵ the energies go up again. In all cases (except possibly $S_z = 0$, $\lambda = 2$), we are sure to be in the linear regime for $\epsilon^2 < 0.15$.

3.3.2 Trotter convergence for $N = 2$ with impurity

Now, we study the Trotter convergence with and without the impurity potential (2.16) for low temperature $\beta = 8$ and intermediate interaction strength $\lambda = 4$. These are the relevant parameters for our extended numerical study for higher electron number.

Figure 3.8 shows a linear regression as a fit to the PIMC data. For the clean dot, the extrapolated energies match perfectly the exact diagonalization result. Convergence for $S_z = 0$ is achieved for $\epsilon^2 = 0.032$ corresponding to a Trotter number $P = 45$. For $S = 1$ the correct energy is obtained with $P = 22$. With impurity, the slopes of the two curves show clearly that the convergence is much slower. Now, the polarized $S = 1$ state has approximately the same slope as the $S_z = 0$ state, it converges also from below and we have to choose at least $P = 65$.

¹⁴This is also the case for more than two polarized electrons. However, as we will see below, with impurity the convergence behavior changes.

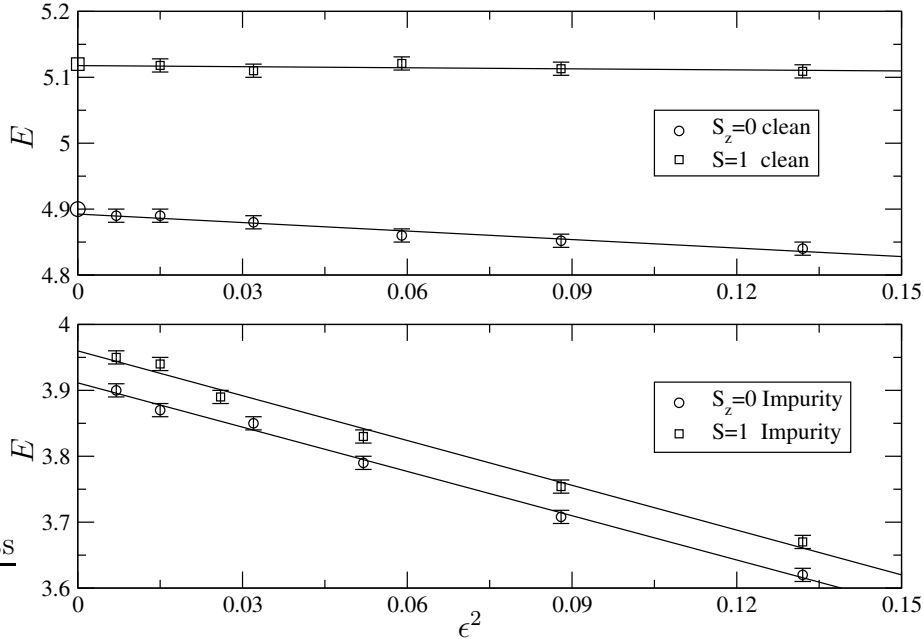


Fig. 3.8: Energies of two interacting electrons in a 2D oscillator for finite temperature $\beta = 8$ and $\lambda = 4$ versus values of $\epsilon^2 = (\beta/P)^2$. PIMC results (with error bars and linear regression fits) with ($w = 4$) and without impurity ($w = 0$, exact diagonalization result \circ , \square shown for $\epsilon = 0$).

We note that with impurity the difference between the two spin states has halved. However the ground state is still the singlet. We conjecture that this is also the case for two interacting electrons in an arbitrary, spin-independent potential (without magnetic field) because the singlet state thus corresponds to spinless (spin-polarized) bosons, and a bosonic ground state is always lower or equal in energy with respect to the fermionic ground state¹⁵.

3.3.3 Trotter convergence for higher electron numbers

For three and four electrons in the clean quantum dot at $\lambda = 4$, exact zero temperature data from configuration interaction calculations are available (MIKHAILOV, 2002a,b). We now discuss the Trotter convergence for these higher electron numbers and different spin states.

For the clean $N = 3$ case an interaction-induced transition to a spin-polarized ground state has been predicted by a previous PIMC study (EGGER ET AL., 1999)

¹⁵There is no such statement for higher electron number. For example, three electrons with $S = 3/2$ have a completely antisymmetric spatial wave-function which corresponds to spinless fermions. However, the $S = 1/2$ state does not correspond to a simple permutational symmetry, it does not even factorize into a spatial and a spin part (RUAN ET AL., 1995).

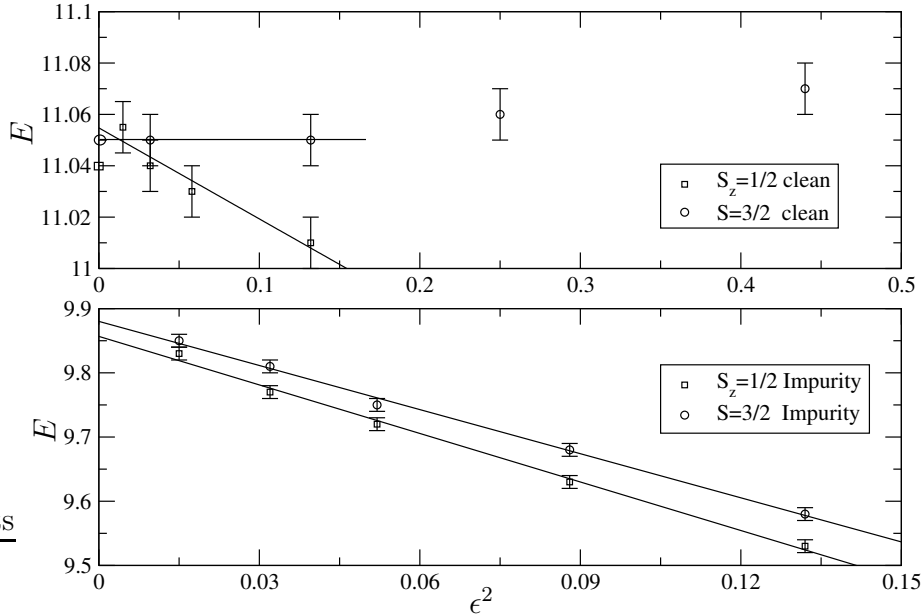


Fig. 3.9: Energies of three interacting electrons in a 2D oscillator for finite temperature $\beta = 8$ and $\lambda = 4$ versus values of $\epsilon^2 = (\beta/P)^2$. PIMC results (with error bars and linear regression fits) with ($w = 4$) and without impurity ($w = 0$, zero temperature exact diagonalization results \circ , \square shown for $\epsilon = 0$).

and also by a semiclassical analysis (HÄUSLER, 2000). At $T = 0$ MIKHAILOV (2002a) determined the transition point $\lambda_c = 4.343$. We are thus very close to this point. Again, as for two electrons, the Trotter convergence for the polarized $S = 3/2$ state is fast (Fig. 3.9): the exact result ($T = 0$, depicted by a \circ at $\epsilon = 0$) lies already in the range of the $P = 16$ ($\epsilon^2 = 0.25$) result and very close to the extrapolated value. The fitted line for the unpolarized state is much steeper. Its intersection with the energy axis lies slightly above the exact zero temperature value (\square). This is expected in view of the spin contamination. For finite temperature the energies of both spin states thus are the same within the range of the small (1 per mill) error bars.

With impurity the convergence is again slower with approximately the same slopes for both spin states. The two extrapolated energies are very close, but the $S_z = 1/2$ state lies still distinctly lower.

A similar behavior is encountered for four electrons. Here, the ground-state spin is found $S = 1$ for all λ with and without impurity. The convergence is shown in Fig. 3.10. Again, the clean polarized $S = 2$ state converges rapidly, convergence for $S_z = 1$ is slower, and is slowest with impurity.

Performing the PIMC for $S_z = 0$ yields the same results as $S_z = 1$ for all Trotter numbers investigated. This is quite important because we are especially interested in the ground-state spin and the spin ordering which we can thus resolve at lower Trotter

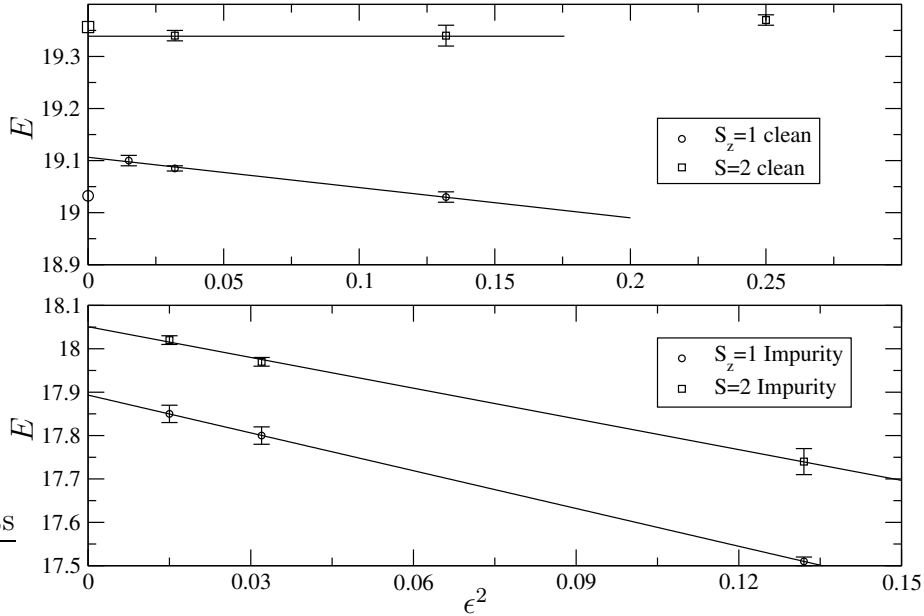


Fig. 3.10: Energies of four interacting electrons in a 2D oscillator for finite temperature $\beta = 8$ and $\lambda = 4$ versus values of $\epsilon^2 = (\beta/P)^2$. PIMC results (with error bars and linear regression fits) with ($w = 4$) and without impurity [$w = 0$, zero temperature diagonalization results ($S = 1$ \circ and $S = 2$ \square)] shown for $\epsilon = 0$.

number. For example, for $N = 3$, $w = 0$ and $\lambda = 6$, the ground state is spin-polarized with an exact energy $E = 13.4373$ [$T = 0$; the unpolarized state has $E = 13.4658$, (MIKHAILOV, 2002a)]. Now, for $P = 25$, where we do not expect the energies to be converged the PIMC gives $E = 13.436(1)$ for $S_z = 3/2$ and $E = 13.457(1)$ for $S_z = 1/2$, which is in impressive accordance for the polarized state. In contrast, the $S_z = 1/2$ state lies lower than the exact $T = 0$, $S = 1/2$ state probably because it receives contributions from below ($S = 3/2$, $S_z = 1/2$). Thus we can reliably determine the spin ordering of the energies for quite low P . Finally, in Figs. 3.11 and 3.12 we display the convergence for higher electron number.

3.3.4 Convergence for other quantities

In the PIMC we do not only sample the energy but also many other quantities, especially the charge density and other correlation densities. We checked convergence for the density by integrating $n(\mathbf{r})$ over some parts of space, e.g. over a disk at the center. Here, the convergence is much faster than for the energy, except at the impurity (see Fig. 3.13), which can be qualitatively understood because the propagator is locally less accurate. Interestingly, the charge in the center converges from below, whereas the charge at the impurity converges from above. In general, the charge densities shown in this work are for $P = 22$ in the clean case, but with

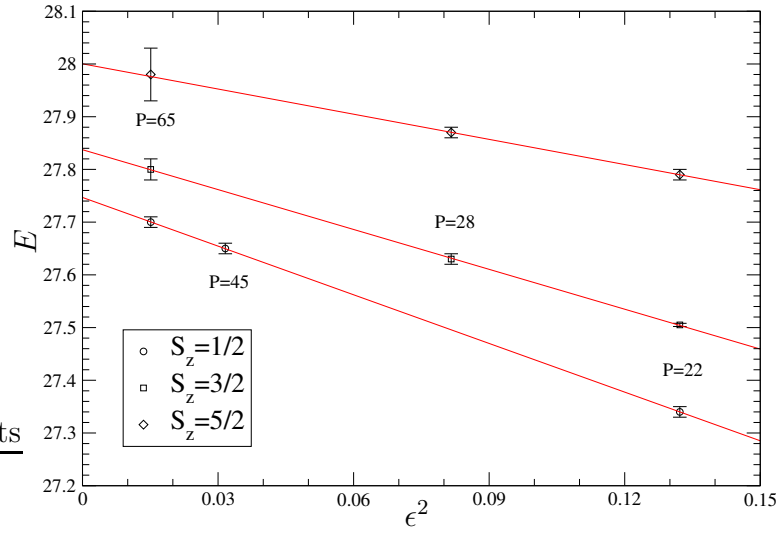


Fig. 3.11: Energies of five interacting electrons in a 2D oscillator with impurity at finite temperature $\beta = 8$ versus values of $\epsilon^2 = (\beta/P)^2$ with error bars and linear regression fits.

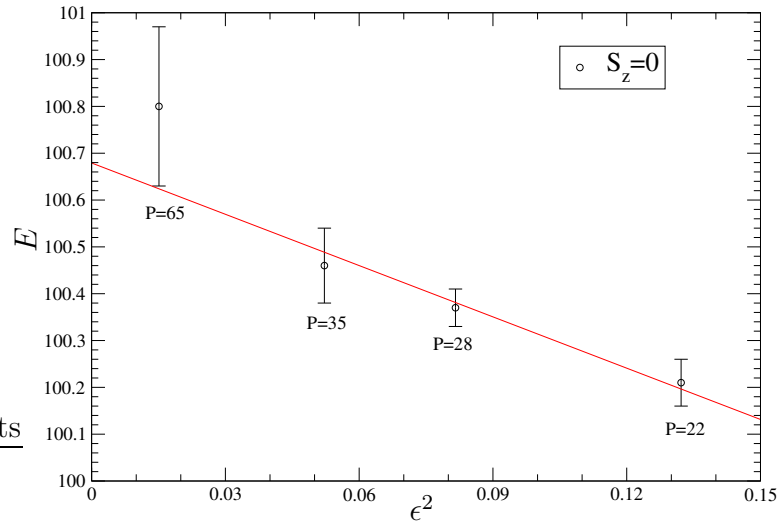


Fig. 3.12: Energies of ten interacting electrons in a 2D oscillator with impurity at finite temperature $\beta = 8$ versus values of $\epsilon^2 = (\beta/P)^2$ with error bars and linear regression fit. The extrapolated value ($\epsilon \rightarrow 0$) is 100.68(9).

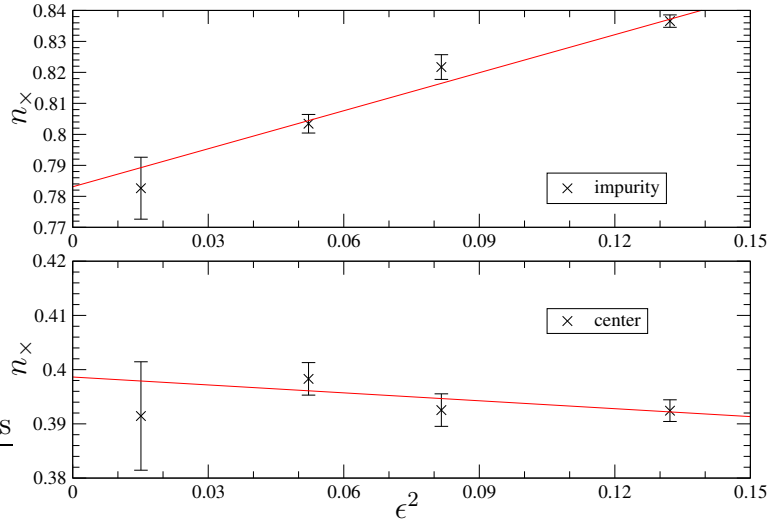


Fig. 3.13: Trotter convergence of the density for $N = 10$, $w = 4$, and $S_z = 0$. Amount of charge n_x integrated over a circle of radius ζ at the center and at the impurity versus values of $\epsilon^2 = (\beta/P)^2$, with error bars and linear regression fit.

impurity we have to choose higher trotter numbers ($\epsilon \approx 0.12$), elsewhere the density at the defect is overestimated.

3.3.5 General procedure

Summarizing, for our choice of parameters, we are sure to be in the regime of quadratic Trotter convergence for Trotter discretization $\epsilon^2 \lesssim 0.15$. In general the simulation proceeds as follows: For an acceptance rate for the Metropolis algorithm of about 30%, the MC step-size is chosen as $\Delta x \approx 2$. Since our problem is symmetric to one axis, we once in a while reflect all coordinates with respect to this axis in order to obtain symmetric densities which corresponds to averaging. Very long runs are necessary to obtain small error bars, ergodicity for the spin and good statistics for the 2D densities. For each data point, we perform ten independent simulations with each up to $M = 4 \times 10^6$ samples. The result with error bar is then estimated from these ten runs. For the Trotter extrapolation, we do this calculation for three to four different Trotter numbers P . The exact value for $\epsilon = 0$ with error bar is then obtained by a linear regression (PRESS ET AL., 1992, p. 659). We recapitulate the two main advantages of the Trotter extrapolation method: First, for smaller P , it is easier to perform an ergodic sampling because the ring polymer described by the discretized PI is more elastic (cf. Sec. 3.1.5). Second, the fermionic sign problem is less severe for smaller P as shown in Fig. 3.1.

3.4 PIMC study for a quantum dot with a single attractive impurity

In this section we present the central results of our PIMC study for a parabolic quantum dot with a single attractive impurity (cf. Sec. 2.9). Our focus is the regime of the incipient Wigner molecule which can hardly be treated with any other method. It is the crossover regime between the quantum and classical limits, therefore the interpretation of our results is sometimes complicated. A shorter version of this work will be published in REUSCH and EGGER (2003).

We start by giving the numerical values for the calculated energies of the dot for $N \leq 10$ and different spins. For the clean dot, despite of the strong interaction, remnants of the energetic shell structure can be identified. With impurity, these cusps in the addition energies disappear. However we find a new, very interesting peak for $N = 8$, which is the only case where the impurity changes the ground-state spin from the expected Hund's rule scheme.

We discuss the onset of Wigner crystallization in real space as depicted by the charge densities. For $N = 6$ we show that spatial ordering is sensitive to spin and this effect is rather enhanced by the impurity. In general, the spin-polarized cases show localization more clearly. In this context we also show spin densities and the correlation function of the impurity's spin with the local spin density. We fathom the possible description of the system with effective spin or lattice Hamiltonians. Our interacting quantum dot with impurity is an intrinsic model for a localized spin so we speculate if we can see some signature of a finite-size Kondo effect as we tune the temperature.

With the present work we also want to give benchmarks to compare with approximative methods. We emphasize that the computationally expensive but exact PIMC method is necessary in order to resolve the tiny energy differences which determine the spin ordering and the addition energies.

3.4.1 Ground-state energies and spins

In Table 3.1 we show our numerical results for the energies for different spins S_z starting with the ground state. For $N > 6$, we cannot afford to calculate all the higher spins states because the sign problem becomes too severe. For $N = 9, 10$, the ground-state spins were derived from finite- ϵ data. In these two cases we also give energies for sub ground-state spin which are more affected by the spin contamination problem but have a smaller error bar (see. Sec. 3.3.3).

For one electron in the deformed dot, the energy is clearly below the first-order perturbation estimate [cf. Eq. (2.17)], but the impurity is not strong enough to bind an electron. For $N = 2 - 4$, the energies without defect were already compared to the literature when we discussed the Trotter convergence (Sec. 3.3.3). Despite of the

N	S_z	$E_{\text{imp}}/\hbar\omega_0$	$E_{\text{clean}}/\hbar\omega_0$	N	S_z	$E_{\text{imp}}/\hbar\omega_0$	$E_{\text{clean}}/\hbar\omega_0$
1	1/2	0.51(1)	1.00	7	1/2	52.49(2)	53.71(2)
2	0	3.911(7)	4.893(7)	7	3/2	52.555(23)	53.80(2)
2	1	3.960(6)	5.118(8)	7	5/2	52.72(4)	53.93(5)
3	1/2	9.857(8)	11.055(8)	7	7/2	–	54.20(11)
3	3/2	9.880(8)	11.050(10)	8	0	67.12(2)	68.52(2)
4	1	17.89(2)	19.104(6)	8	1	67.18(2)	68.44(1)
4	2	18.05(1)	19.34(1)	8	2	67.30(5)	68.51(5)
5	1/2	27.75(1)	29.01(2)	9	1/2	83.22(3)	84.48(3)
5	3/2	27.84(2)	29.12(2)	9	3/2	83.22(4)	84.45(6)
5	5/2	28.00(3)	29.33(2)	9	5/2	83.37(17)	84.61(17)
6	0	39.30(2)	40.53(1)	10	0	100.68(9)	101.99(7)
6	1	39.37(2)	40.62(2)	10	1	100.59(11)	101.96(14)
6	2	39.48(2)	40.69(2)				
6	3	39.84(7)	40.83(4)				

Table 3.1: Ground-state energies for the quantum dot with and without impurity. Bracketed numbers are one standard deviation error bars for the last digit(s).

strong interaction, for up to $N = 10$ electrons the ground-state spin of the clean dot follows the expectation from the energetic shell-filling and Hund’s rule (Sec. 2.5). With impurity, the spin ordering is not changed except for $N = 8$. We discuss this now in more detail.

For $N = 3$ without impurity, the two spin states have the same energy within error bars (see also Fig. 3.9). An interaction-induced transition to a spin-polarized ground state was predicted in a configuration-interaction (CI) study for $\lambda > 4.343$ at zero temperature (MIKHAILOV, 2002a). For $\lambda = 4$, we are still below this transition point. However, at finite temperature, the difference between the first excited state and the ground state is diminished due to spin contamination. Furthermore, it seems that the impurity tends to depolarize the system, since the gap between the two spin states becomes larger. Thus, the transition point is shifted to a higher λ . Maybe this is due to the geometrical influence of the impurity which is located rather close to the center: MIKHAILOV (2002a) showed that in the clean case the crossover from the $S = 1/2$ to the $S = 3/2$ state corresponds to a change from a linear to a threefold geometry, which is then also the classical configuration.

For $N = 6$ in the clean dot with strong interaction ($\lambda = 8$), a PIMC study (EGGER ET AL., 1999) and also semiclassics (HÄUSLER, 2000) predicted a $S = 1$ ground state in contrast to the closed shell $S = 0$ for weak interaction. REIMANN ET AL. (2000) found by means of CI calculations that the ground state was unpolarized up to at least $\lambda \approx 3.5$ (see below). Now, we state that both with and without impurity the ground state for $\lambda = 4$ is $S = 0$ but only with a small gap to the next higher state.

For six electrons, there is also an interesting spin-dependent geometric transition between the five- and the sixfold configurations (see below Subsec. 3.4.2). For the clean seven-electron dot, EGGER ET AL. (1999) predicted a $S = 5/2$ ground state for $\lambda = 8$ instead of the expected $S = 1/2$. We find $S = 1/2$. The gap to the next higher state is rather diminished by the impurity.

For $N = 8$, the prediction for the clean dot and strong interaction ($\lambda \gtrsim 6$) was $S = 2$ (EGGER ET AL., 1999). We find that at $\lambda = 4$ the impurity changes the ground-state spin from $S = 1$ (Hund's rule) to $S = 0$. Probably this depolarization can be attributed to the formation of local momenta at the defect and in the center on the dot¹⁶. This case of sub-Hund's rule spin is very unexpected because, normally, interaction tends to drive the system versus a spin polarization. Below, we see in the addition energies that the eight-electron dot becomes relatively stable in presence of the impurity, while it is very unstable in the clean case.

This sub-Hund's rule spin has also an important consequence, which can be probed experimentally. Since for $N = 9$, we have $S = 3/2$, this change in ground-state spin $\Delta S > 1/2$ should lead to the suppression of the conductance peak for the addition of the ninth electron in a transport experiment (cf. Sec. 2.2). The effect is called *spin blockade* (WEINMANN ET AL., 1995) in analogy to the normal Coulomb blockade. It cannot occur in the weakly interacting regime where electrons together with their spins are accommodated in shells of orbitals. We thus predict this spin blockade for a weakly disordered dot with $N = 8$ when the electron density is low enough.

With the ground-state energies we obtain the addition energies $\Delta(N)$ [Eq. (2.3), Eq. (2.14)], which can be measured in experiments. In Fig. 3.14(a) we show the addition energies for $N < 10$. The curves go down nearly monotonically, although with some very interesting remnants of the energetic shell-structure. In the clean case, in spite of the strong interaction, one can still recognize the enhanced stability of the completely filled second shells ($N = 6$) and the half filled shells ($N = 4, 9$). Nine electrons appear to be exceptionally stable and eight electrons very unstable. This could be possibly attributed to the spin transition $S = 1 \rightarrow 2$ for $N = 8$ mentioned above, or to the stability of the classical configurations. We note that the peak at $N = 2$, which corresponds to the closure of the first shell (cf. Fig. 2.10) is absent already for $\lambda \gtrsim 2$. The addition energy for the first electron is very high. In fact, $\Delta(1)$ can be understood as the Coulomb repulsion for two electrons in the constant interaction model, so classically it would be $\Delta(1) \approx 2\lambda/r_s \approx 2$.

The impurity strongly affects the addition energies, most drastically for $N = 8$. This configuration is now exceptionally stable¹⁷. The cusp for $N = 4$ has disappeared,

¹⁶By monitoring the spin-spin correlation we can see a strong antiferromagnetic coupling between electrons at the impurity and the center (see below Sec. 3.4.2). Unfortunately our data is quite noisy and supposedly, still lower temperatures are necessary to see a pronounced effect.

¹⁷We speculate that this new peak might be generic as its appearance is accompanied by the transition to a new ground-state spin. CIORGA ET AL. (2000) have found a $N = 8$ peak in their experiments and the shape of their lateral dot bears some similarities to our deformed potential.

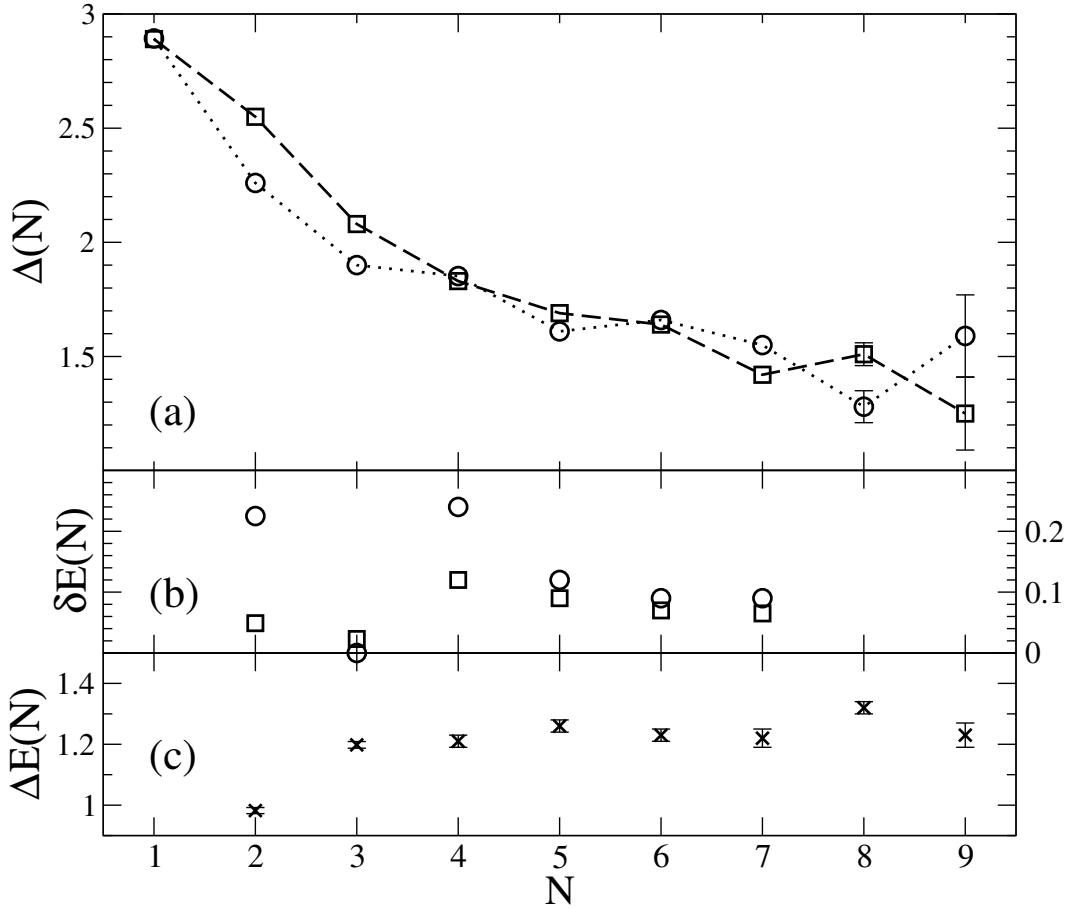


Fig. 3.14: PIMC results with impurity (squares) and for a clean dot (circles), for (a) the addition energy $\Delta(N)$ and (b) the spin gap $\delta E(N)$ for $N < 8$. In (c) $\Delta E(N)$ is the amount by which the impurity has lowered the energy. Error bars, unless shown explicitly, are of the order of the symbol size. Dashed and dotted lines are guides to the eye only.

and for $N = 6$ the shell structure is nearly completely washed out. Interestingly, the values of $\Delta(N)$ for the relatively stable electron numbers $N = 1, 4, 6$ are almost not changed by the impurity. Therefore, we can say that magic numbers are not only astonishingly stable against interaction effects, but their addition energies are also nearly unaffected by the impurity, while the rest of the spectrum is altered substantially.

We were seeking for the phenomenon of *bunching*, i.e. experimentally found vanishing addition energies for certain values of N (Sec. 2.13). In our simple but realistic model, bunching is *not* observed for $N < 10$ (Fig. 3.14). In experiments, level bunching was found only for $N > 7$ (ASHOORI ET AL., 1998). Our calculated addition energies are also most strongly changed by the impurity for $N = 8, 9$. However, we do not find vanishing $\Delta(N)$. Maybe one has to consider even larger electron num-

bers or to assume stronger disorder or other mechanisms not contained in our model. CANALI (2000) emphasized that he found bunching in his lattice model only for short-range interaction (cf. Sec. 2.14). We can only speculate if a screened Coulomb interaction potential would lead to bunching in our continuous model. ZHITENEV ET AL. (1997) estimate the screening length in their dots roughly about 10nm, but this is surely a lower bound and not an exact value for the few-electron limit. We note that bunching and pairing is believed to be a generic effect, though it has been found exclusively in one special kind of experiments.

Since except for $N = 8$, the ground-state spin is not changed by the impurity, its effect on the spin polarization seems to be rather weak. Nevertheless, our results indicate that the defect tends to decrease the “spin gap”

$$\delta E(N) = E_{S+1} - E_S, \quad (3.53)$$

where S is the ground-state spin. This is seen in Fig. 3.14(b), most strikingly for $N = 2, 4$. It indicates a weak tendency towards spin polarization in disordered dots. The role of impurities on the spin polarization of interacting quantum dots has recently been studied by various groups, suggesting either a tendency towards spin polarization (BERKOVITS, 1998; BENENTI ET AL., 2001; JIANG ET AL., 2003), depolarization (JACQUOD and STONE, 2000), or strongly N -dependent behaviors without general trend (HIROSE and WINGREEN, 2002)¹⁸. We also rather adopt this latter point of view, as we found in general a decreased spin gap but also two cases of a trend towards depolarization.

The influence of the impurity can also be quantified when we consider the energy difference between the clean and the deformed dot,

$$\Delta E(N) = E_{\text{clean}} - E_{\text{imp}}. \quad (3.54)$$

In Fig. 3.14(c) $\Delta E(N)$ is nearly constant for $N > 2$, however with a cusp for $N = 8$ where we found the spin transition. Thus the impurity lowers the energy of the eight-electron dot most efficiently.

¹⁸The cited works investigated lattice models, except JIANG ET AL. (2003) and HIROSE and WINGREEN (2002) who studied continuous models with spin-density functional theory (SDFT). CANALI (2000) related the bunching for the energies of his lattice model to the formation of local singlets (see Sec. 2.14), but did not comment in more detail on ground-state spin. The model of HIROSE and WINGREEN (2002) is similar to ours but they include many impurities (see footnote in Sec. 2.9). They considered fluctuations in the addition energies $\Delta(10)$ and $\Delta(11)$ for $0 \leq \lambda < 3$. They found that the probability for non-minimal ground-state spin increases with λ , but never exceeds 50%, and show with a two-orbital model that off-diagonal Coulomb matrix elements stabilize the minimal ground-state spin, as predicted by JACQUOD and STONE (2000). - It would be interesting to test the SDFT method against our results.

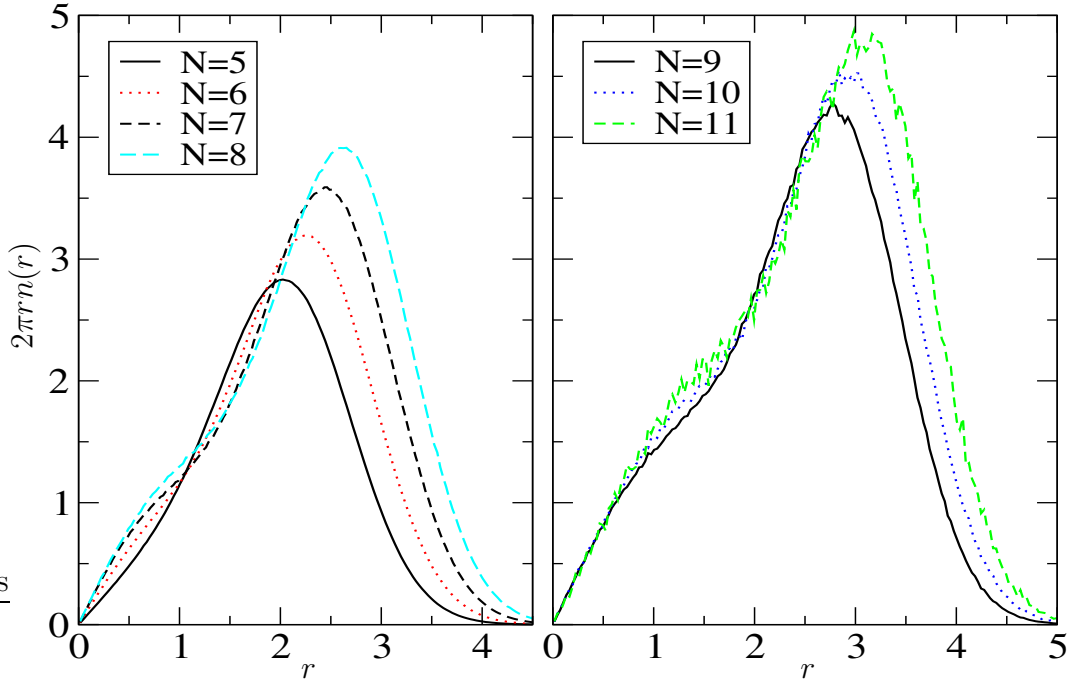


Fig. 3.15: Radial densities for the clean dot with $\lambda = 4$ and minimal spin ($P = 22$). Although Wigner crystallization is not yet very pronounced one can see that the sixth electron enters the center.

3.4.2 Charge and spin densities

With the PIMC we can easily sample two-dimensional one- and two-particle densities like the charge density or the spatial correlation function. We also monitor spatial spin-spin correlation densities (cf. Sec. 3.1.6).

Clean dot, incipient Wigner crystallization

We start with showing the radial charge densities $2\pi r n(r)$ for six to eleven electrons with minimal spin in the clean dot (Fig. 3.15). Densities for the ground state look the same. We are in the incipient Wigner molecule regime, so the density in the center of the dot is nearly constant with a weak modulation. There is no pronounced radial ordering as seen for $\lambda = 8$ in Fig. 2.8 (for spin-polarized electrons) or in Fig. 1 of EGGER ET AL. (1999). However from the curvature for $N = 5, 6$ one can infer that the sixth electron is accommodated rather in the center (see detailed discussion below). With increasing electron number the dot expands laterally and the inner modulation becomes stronger. For $N \geq 8$ the curves have nearly the same slope which indicates that the charge in the center depends only weakly on N .

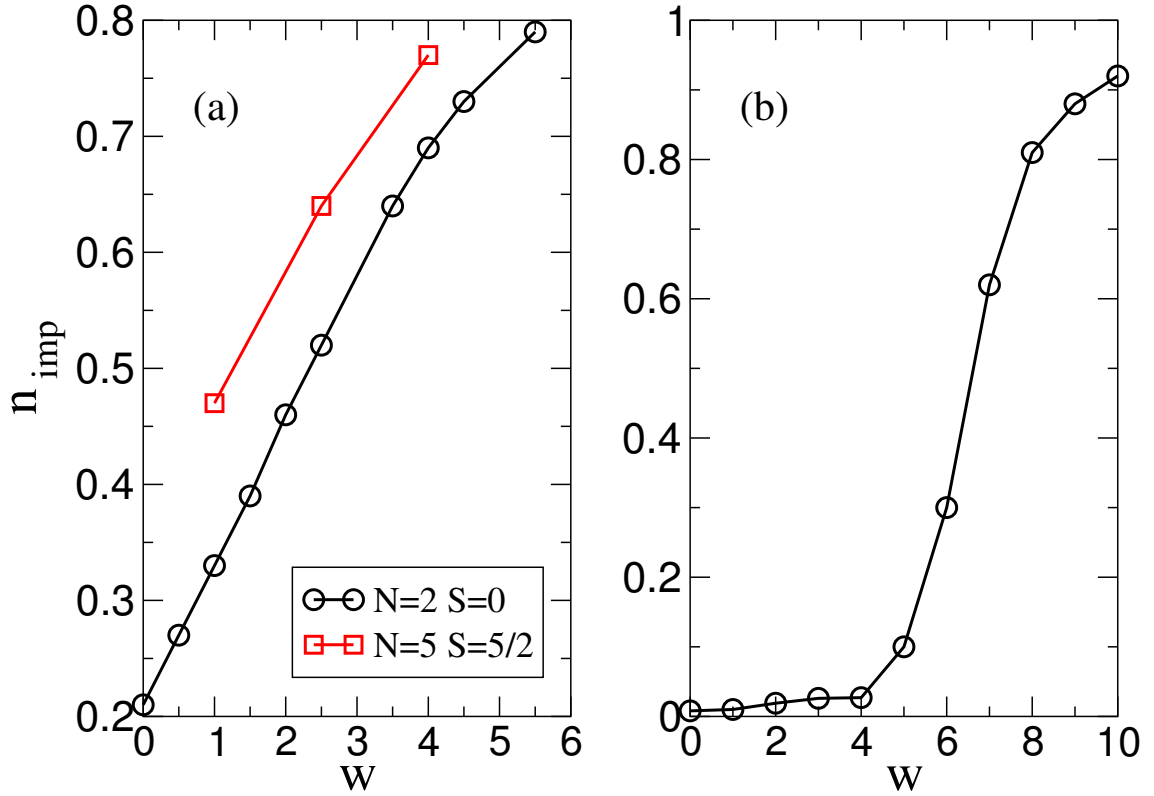


Fig. 3.16: Amount of electron charge n_{imp} trapped by the impurity vs. impurity depth w for (a) $\mathbf{x} = (0, 1.5)$, $\zeta = 0.75$ and (b) $\mathbf{x} = (0, 3)$, $\zeta = 0.82$ in a quantum dot with two (circles) and five electrons (squares) and $\lambda = 4$.

Localization at the impurity

Now we study the influence of the symmetry-breaking impurity. First we show the amount of charge $n_{\text{imp}} = \int_{B_\zeta(\mathbf{x})} d^2r n(\mathbf{r})$ within the effective radius ζ of the impurity when we vary the impurity depth w . For our parameters [Fig. 3.16(a)] this amount of charge increases roughly linear with w , and by fixing $w = 4$ we obtain that about 75% of an electron is trapped by the impurity. For higher electron number, this fraction does not depend too strongly on N . (For one electron the corresponding values is about 41%.) In contrast we show the localization when the impurity is put farther away from the center [Fig. 3.16(b)]: Now, there is a barrier in the outer potential, we have to choose a much higher w to trap an electron. Localization starts abruptly for $w \gtrsim 5$ and seems to saturate for $w \approx 10$.

Charge and spin densities with impurity

Next we show contour plots of the 2D charge densities $n(\mathbf{r})$ for $N = 2 - 5$ with our standard impurity [$w = 4$, $\mathbf{x} = (0, 1.5)$, $\zeta = 0.75$]. It is apparent that rotational

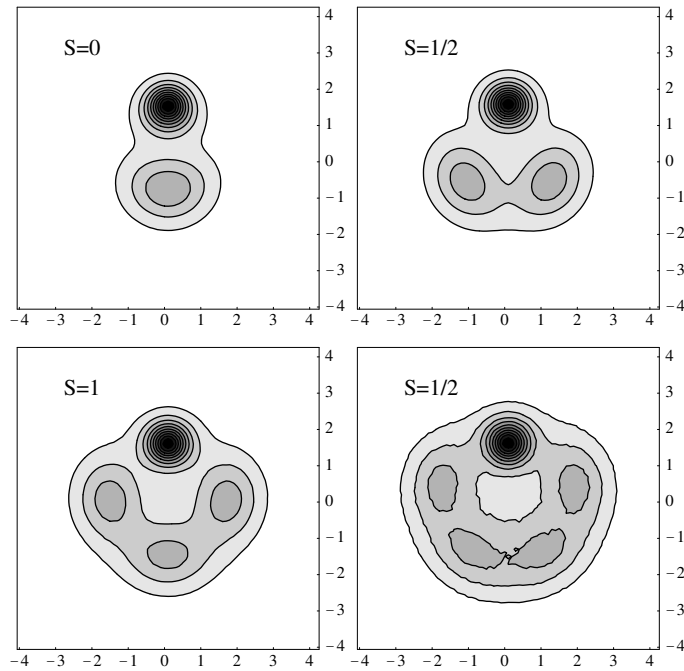


Fig. 3.17: Shaded contour plots of the charge densities $n(\mathbf{r})$ for $\lambda = 4$, ground-state spin, $w = 4$, $\beta = 8$, $N = 2 - 5$. $P = 65$. Contours lie at integral multiples of 0.1 times the maximal density. Darker shading signals higher density.

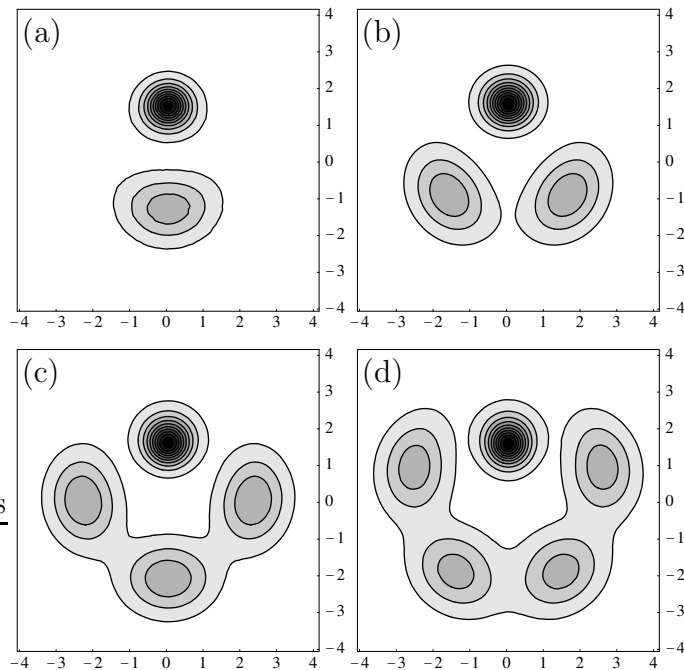


Fig. 3.18: Ground-state charge densities $n(\mathbf{r})$ for $N = 2 - 5$ as above but $\lambda = 10$.

symmetry is efficiently broken. The density at the defect is more than three times higher than at the rest of the dot. The molecule-like structure with the single localized electrons which are arranged around the impurity is evident, although the electrons still have strong overlap.

By looking at the corresponding spin densities $s_z(\mathbf{r})$, we see very similar distributions only with a deeper depression in the center (see also below, for $N = 6$). This means that we are in a regime where the spin follows mostly the charge distribution. Note, that this is not the case for vanishing interaction where the spin density is determined by the singly occupied orbitals. In the deep Wigner-molecule regime, charge and spin have very similar distributions¹⁹, as already known for the clean quantum dot (EGGER ET AL., 1999; MIKHAILOV, 2002b). Obviously, for spin-polarized dots holds $s_z(\mathbf{r}) = n(\mathbf{r})/2$.

To illustrate the case of strong crystallization we present in Fig. 3.18 the same ground-state densities for $\lambda = 10$. The corresponding Brueckner parameter²⁰ is $r_s \approx 15$. The peak at the defect is nearly unchanged, but now the maxima for the other electrons are more pronounced and separated from each other. While with increasing electron number and λ , the electron molecule expands, the electron at the impurity remains at its position and for $N = 5$ [Fig. 3.18(d)] it is nearly embraced by a molecule-like ring.

Spin correlation density and effective Hamiltonians

Another interesting observable is the correlation of the impurity spin (3.22) with the spin density

$$\xi(\mathbf{r}) = \langle S_z^{\text{imp}} s_z(\mathbf{r}) \rangle \quad (3.55)$$

which we show in Fig. 3.19. It holds $\int d^2r \xi(\mathbf{r}) = S_z S_z^{\text{imp}}$. The densities display a large peak at the defect, which means that there is really only one electron trapped. One can see a correlation hole around the impurity for $N > 3$. For $N = 2, 3$ the minima coincide with the maxima of the charge densities in Fig. 3.17, the spin ordering is clearly antiferromagnetic. In the case of four and five electrons the behavior is not so clear, $\xi(\mathbf{r})$ has its maxima at different positions than $n(\mathbf{r})$. For $N = 4, S_z = 1$, negative spin is distributed in the center, close to the impurity. For $N = 5, S_z = 1/2$,

¹⁹To quantify this we tried to compute the function $I = \int d^2r [s_z(\mathbf{r}) - (S_z/N)n(\mathbf{r})]^2$ for given N, λ and S_z . This I vanishes when charge and spin are identically distributed, so we expect I to decay with increasing interaction. However, there are problems with noise and proper sampling of $s_z(\mathbf{r})$ (cf. Sec. 3.1.6). Also, Trotter convergence has to be checked carefully when doing the simulation for different λ .

²⁰Such densities are not yet in experimental reach for quantum dots. However this quasi-classical regime is tempting for PIMC studies because there is hardly any sign problem. FILINOV ET AL. (2001) studied thermal and quantum melting for densities as low as $r_s \approx 35$. BERNU ET AL. (2001) investigated the 2D electron gas with PIMC up to $r_s \approx 200$. Our PIMC code with anti-symmetrization at every time slice is best adapted to the crossover regime where the sign problem is worst.

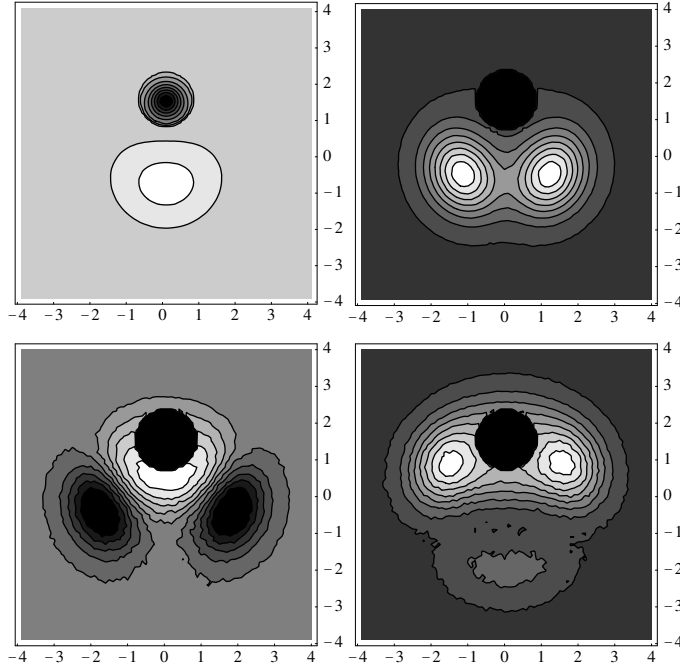


Fig. 3.19: Spin correlation density $\xi(\mathbf{r})$ corresponding to the ground states shown in Fig. 3.17, $N = 2 - 5$. $P = 22$, but results for higher P are qualitatively the same. For $N > 2$ the maximum at the impurity is cut at a value of 0.005 in order to resolve the tiny correlation $\xi(\mathbf{r})$ outside the impurity. The gray shade outside the dot corresponds to zero correlation, whereas brighter gray shades mean negative correlation.

negative spin correlation extends nearly over the area of the dot, with two pronounced minima close to the impurity.

It would be interesting to know if the system maps on an effective Hamiltonian, e.g. of Heisenberg type, $H = \sum_{\langle i,j \rangle} J_{i,j} \mathbf{S}_i \mathbf{S}_j$, where the charge degrees of freedom have been eliminated. For three electrons in Fig. 3.19, this would give a frustrated antiferromagnet for the low-energy spectrum. However, at $r_s = 4$ we are still far from this regime, we have high mobility of charge and spin. BERNU ET AL. (2001) calculated exchange energies for the 2D Wigner crystal with PIMC ($45 \leq r_s \leq 200$). They obtained an effective spin Hamiltonian which can be diagonalized and stated that at zero temperature and very low density, $r_s \approx 175$, the system undergoes a phase transition from a spin liquid to a ferromagnetic ground state. CREFFIELD ET AL. (1999) performed an exact diagonalization in real space for two electrons in polygonal dots ($r_s \lesssim 100$). They found that the spectra could be reproduced very well by an effective Hubbard-type Hamiltonian with hopping, exchange, superexchange and Coulomb repulsion (tJV model). For some geometries they had to include three-site terms of combined hopping and spin-flips, so their model is quite elaborate. Unfortunately, with PIMC we do not obtain a complete spectrum, but in general, constructing an ef-

fective Hamiltonian can help to understand the low-energy excitations of the Wigner molecule (cf. Sec. 2.7)²¹.

Charge and spin order for $N = 6$

The case $N = 6$ is especially interesting because now one electron can enter the center of the dot. Classically, the fivefold geometry has a lower energy than the hexagon (Table 2.1). The clean six-electron Wigner molecule has also been studied by REIMANN ET AL. (2000), who found by means of CI calculations that the true ground state is unpolarized antiferromagnetic with a sixfold symmetry up to at least $\lambda \approx 3.5$, whereas the polarized state has already fivefold symmetry at this interaction strength²². They quantified this by computing the pair correlation function $g_{\sigma\sigma'}(\phi)$ for (anti-)parallel spins at the outer maximum of the density distribution. In Sec. 4.3.5 we will discuss how the Wigner crystallization of the six-electron molecule takes place within the Hartree-Fock approximation.

We start by showing charge and spin distributions for the clean dot in Fig. 3.20. The 2D contour plots show radial ordering, however, for $S_z = 0, 1$ the densities are rather flat in the center [Fig. 3.20(a),(b)]. Only in the spin-polarized case [Fig. 3.20(c)] a pronounced peak appears in the center, putting in evidence the fivefold geometry. The spin correlation density $\xi(\mathbf{r})$ for the ground state is shown in Fig. 3.20(d) and suggests antiferromagnetic spin order. Here, $\xi(\mathbf{r})$ has been defined for the same position as above with impurity, Sec. 3.4.2, which for the clean six-electron dot lies at the maximum of the outer ring. However, $\xi(\mathbf{r})$ decays quickly when we move away from the considered region. The spin density for $S_z = 0$ vanishes within the statistical error. For the state with $S_z = 1$, the distribution of $s_z(\mathbf{r})$ [Fig. 3.20(e)] is similar to the corresponding charge density, except at the center, where it displays a clear minimum. This means that spin mobility in the center is enhanced.

In Fig. 3.21 we present the same densities for the dot with the defect. Now, a high peak is surrounded by a nearby plateau which exhibits small modulation. The cusps in the plateau show the crystalline structure of the pinned Wigner molecule. As before in the clean case, localization becomes stronger with increasing spin [Fig. 3.21(a)-(c)]. We will quantify this below. However at first glance, Wigner crystallization is enhanced by the defect. Also, the spin correlation $\xi(\mathbf{r})$ for the ground state [Fig. 3.21(d)] shows stronger antiferromagnetic coupling than in the clean case. This becomes still more evident for lower temperature, e.g. $\beta = 12$ (see Fig. 3.24). The spin density for $S_z = 1$ [Fig. 3.21(e)] does not too well follow the charge density. It is increased at the impurity's next neighbors and smaller at the center and away from the impurity.

²¹In Sec. 4.3.4 we show that the UHF Hamiltonian for strong interaction is equivalent to *one* particle hopping between the different sites of a Wigner molecule.

²²They cannot perform calculations for higher coupling constants, because the truncation of Hilbert space becomes too severe a problem. Their energies agree quite well with PIMC results.

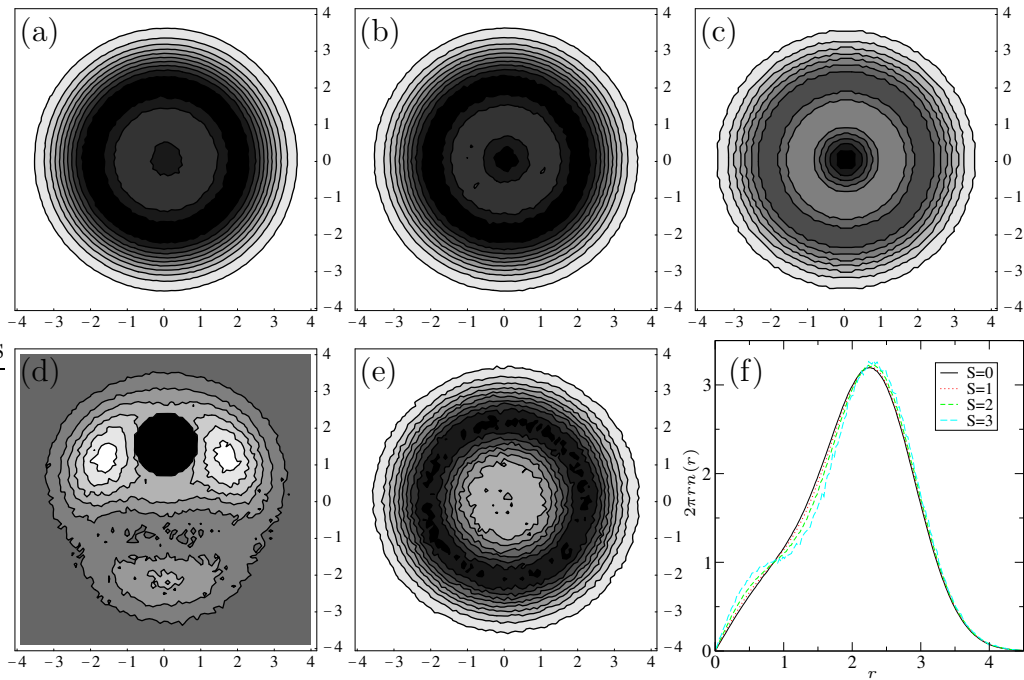


Fig. 3.20: Six electrons in the clean quantum dot. Charge density $n(\mathbf{r})$ for $S_z = 0, 1, 3$ [(a)-(c)]. (d) Spin correlation density $\xi(\mathbf{r})$, $S_z = 0$. (e) Spin density $s_z(\mathbf{r})$, $S_z = 1$. In (f) radial charge densities for different spins.

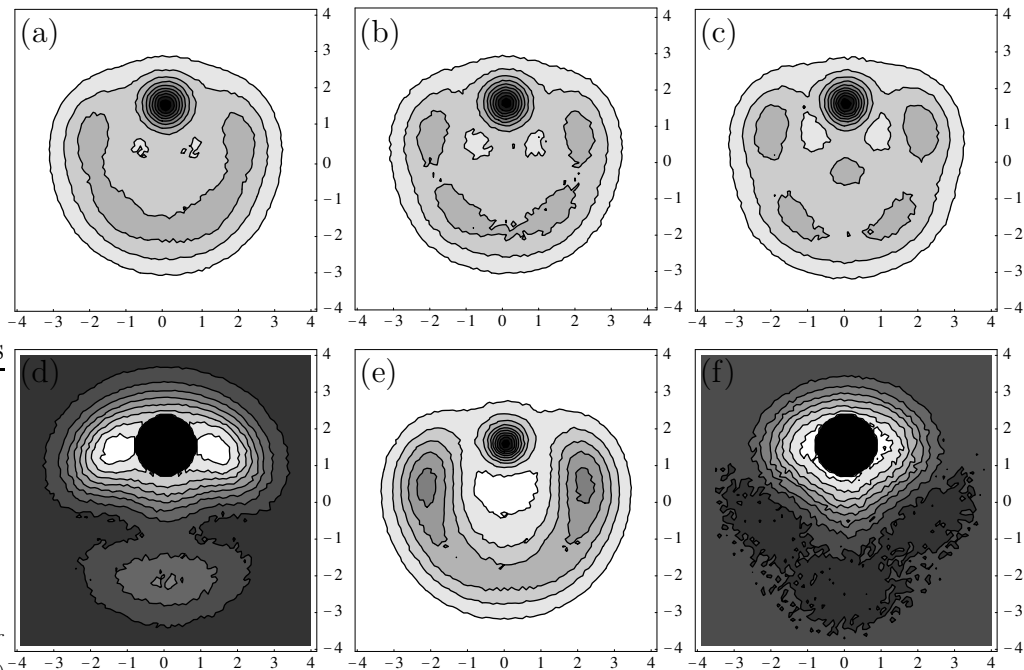


Fig. 3.21: Same as in Fig. 3.20 but with impurity. In (f) $\xi(\mathbf{r})$ for $S_z = 1$. Note that shading and contours refer to the height relative to the maximum of each single density plot, they do not have a common scale.

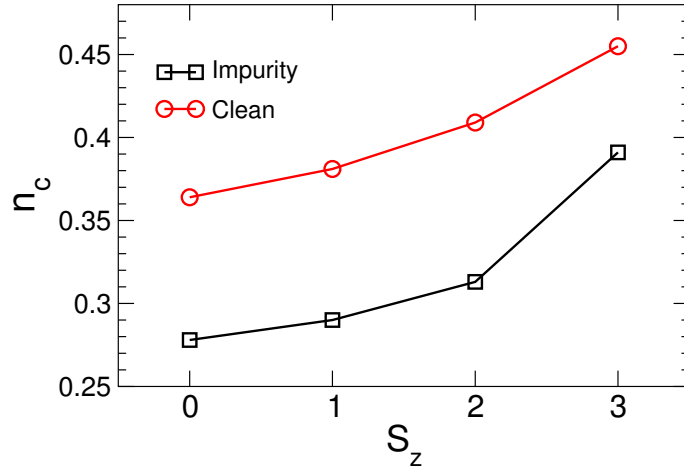


Fig. 3.22: Amount n_c of electron charge localized in the center integrated over a radius $\varsigma = 0.75$ for $N = 6$ and different spins.

This typical pattern for $s_z(\mathbf{r})$ is also seen for higher electron number which indicates that the impurity strongly affects the spin structure. The respective $\xi(\mathbf{r})$ [Fig. 3.21(f)] displays an antiferromagnetic coupling close to the defect and a tiny ferromagnetic correlation farther away from it, similar to the case $N = 4, S_z = 1$.

Figure 3.22 summarizes our findings for $N = 6$ quantitatively. We calculate the amount of charge in the center $n_c = \int_{B_\varsigma(\mathbf{0})} d^2r n(\mathbf{r})$ and plot it versus the spin quantum number. Here, we see that indeed this amount is bigger for higher spin. The nearby impurity draws off charge from the center, therefore the values for the clean dot are higher. When S_z is increased, more and more charge goes into the central region. For the clean dot, comparing $S = 0$ and $S = 3$, this amounts to a $\approx 25\%$ increase in n_c , but with the defect, this increase is $\approx 40\%$. That implies that the spin sensitivity of the incipient crystallization process is significantly enhanced by the impurity. The strong dependence on spin means that there is no clear separation of energy scales for spin and charge fluctuations. Such behavior is only found in the *incipient* Wigner molecule regime, and invalidates the commonly used lattice-spin models appropriate in the deep Wigner-crystallized limit.

Charge densities for $N > 6$

Figure 3.23 shows contour plots for the ground-state charge density for $N = 7$ to 10 electrons. At the defect, the density is about three times larger than elsewhere in the dot. Although there are large quantum fluctuations, a spatial shell structure is already discernible. The classical prediction for clean dots at these electron numbers is as follows (cf. Sec. 2.8). For $N = 7$ and $N = 8$, just one electron is in the center, while for $N = 9$ and $N = 10$, the spatial filling is $(2, 7)$ and $(2, 8)$, respectively, with the configurations $(1, 8)$ and $(3, 7)$ very close in energy. Quantum-mechanically, for

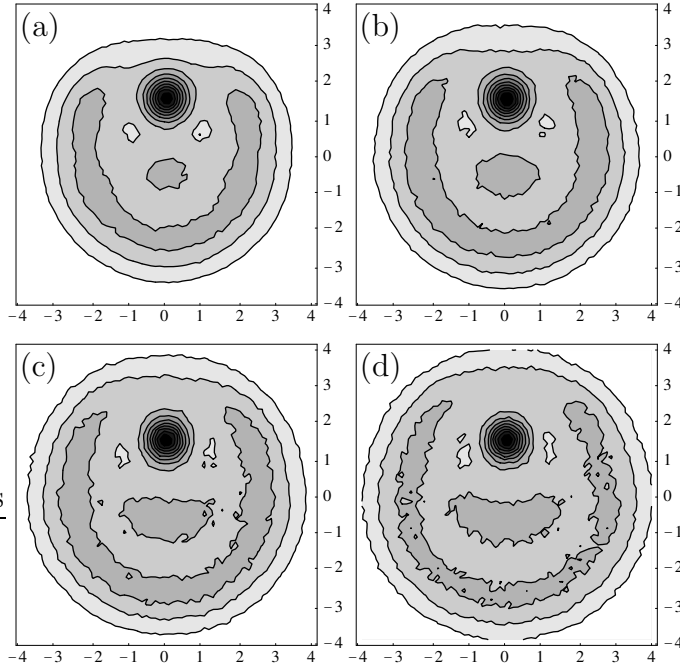


Fig. 3.23: Quantum dot with impurity. Charge densities $n(\mathbf{r})$ for $\beta = 4$ and $N = 7, 8, 9$, and 10 electrons [(a)-(d)]. $P = 33$. For lower temperature the densities look very similar although with more noise. The incoming electrons are accommodated in the outer ring (also for $N = 11$) which merges and for $N = 10$ nearly embraces the impurity. Note that the density at the impurity is more than three times higher than at the rest of the dot. Its Trotter convergence is slow, therefore we cannot show the densities for lower P .

$\lambda = 4$, the radial ordering is not yet very pronounced in the clean dot (cf. Fig. 3.15 and REIMANN ET AL., 2000). With impurity, however, our data in Fig. 3.23 displays spatial shells, although with a rather different filling sequence. A detailed examination of the central region shows that only one to two electrons are accommodated in this part. Therefore incoming electrons enter the outer ring for $N = 7, 8, 9$, and 10, with the ring expanding and, for $N = 10$, nearly embracing the impurity.

3.4.3 Impurity susceptibility - finite-size Kondo effect?

The impurity captures an electron which carries a magnetic momentum. We therefore have an intrinsic model for a localized spin with a surrounding bath, which bears some similarities with the Kondo problem²³. One can define a magnetic momentum of the

²³The Kondo effect has indeed been found in quantum dots (KOUWENHOVEN and GLAZMAN, 2001). However, there, the whole dot with one unpaired electron serves as an artificial magnetic impurity. In these experiments, the dot is more strongly coupled to the leads and, at low temperatures, the conductance through it is *enhanced* by the Kondo effect. (In metals with magnetic

impurity M^{imp} [cf. Eq. (3.22)] and a susceptibility

$$\chi_z^{\text{imp}} = \frac{\partial M^{\text{imp}}}{\partial B} = \int_0^\beta d\tau \left\{ \langle S_z^{\text{imp}}(\tau) S_z^{\text{imp}}(0) \rangle - \langle S_z^{\text{imp}} \rangle^2 \right\}. \quad (3.56)$$

This expression is obtained by introducing a coupling $V = -\mathbf{M}^{\text{imp}} \cdot \mathbf{B}$ to an external magnetic field and then letting $B \rightarrow 0$. It is the integral over the imaginary-time auto correlation function of the impurity's spin, which has the period β . We can sample the first part of the integrand quite well (fast Trotter convergence), but we also have to sample S_z^{imp} decently! This second term matters because the susceptibility decreases with increasing spin polarization.

If one electron is isolated on the impurity its susceptibility reads $\chi_z^{\text{Curie}} = \beta/4$. We have about 3/4 of an electron charge localised within a radius of $\zeta = 0.75$, so we expect χ_z^{imp} to be diminished. In the classical Kondo problem, a localized spin of a magnetic impurity is coupled to the spin of the conduction electrons in a metal. Its susceptibility is diminished according to $\chi_z^{\text{Kondo}} = \beta/4[1 - 1/\ln(T/T_K) + \dots]$, for $T \gg T_K$, where T_K is the Kondo temperature. The impurity is surrounded by a screening cloud and at low temperatures $T \ll T_K$ a total spin singlet forms and the susceptibility saturates $T_K \chi_z^{\text{Kondo}} = 1 - (T/T_K)^2$.

In our system the impurity's spin is coupled to a small, strongly correlated bath. For our parameters the susceptibility does not show a clear dependence on the electron number. In Fig. 3.24 we plot χ_z^{imp} for the unpolarized six electron dot. It decays with increasing temperature and seems to saturate when $T \rightarrow 0$ which is the expected behavior. However, we do not find a clear signature of Curie or Kondo behavior because our system is far from these ideal cases: the impurity is screened by the bath, but it is not completely localized and the bath is very small and truly not a Fermi liquid.

In the inset of Fig. 3.24 we display the spin correlation density $\xi(\mathbf{r})$ for $\beta = 12$. It shows nicely the antiferromagnetic ordering of the unpolarized six-electron Wigner molecule which is pinned by the impurity. At higher temperature the tiny positive correlation at the next-nearest-neighbor sites are washed out (cf. Fig. 3.21).

3.5 Conclusion

To conclude, we have presented an extensive path-integral Monte Carlo (PIMC) study for interacting electrons in a parabolic quantum dot. We have obtained high-precision results for clean dots and in the presence of a symmetry-breaking impurity. First, we have explained comprehensively the basic idea of PIMC and our implementation and procedure. Due to the fermion sign problem, CPU times are very long, we therefore restricted our calculation to $N \leq 10$.

impurities, the resistance increases at low temperatures due to the Kondo effect.)

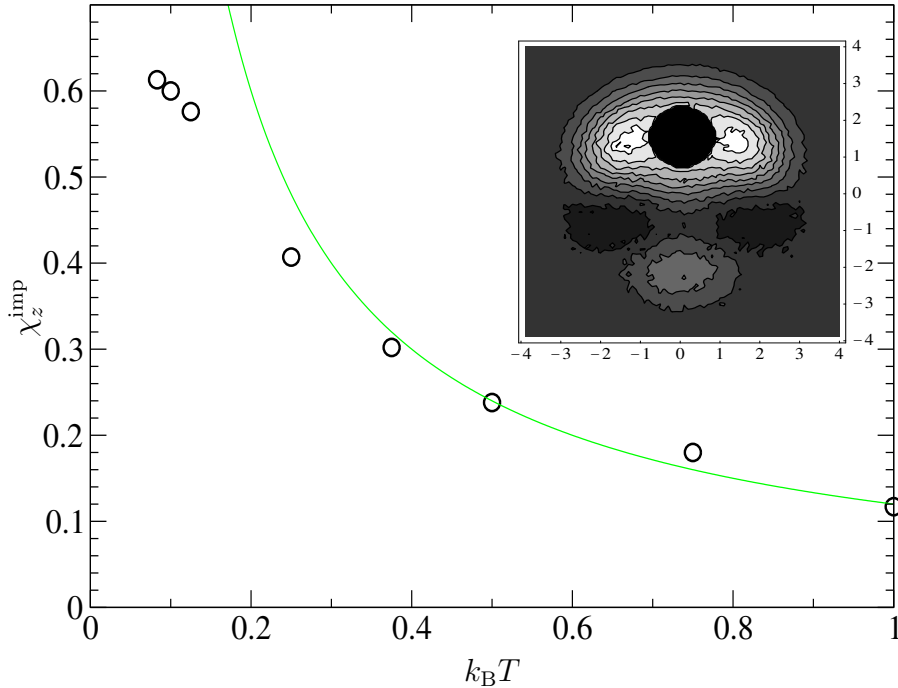


Fig. 3.24: Impurity susceptibility versus $k_B T$ for $N = 6$, $S_z = 0$ (circles). Error bars are smaller than the symbol size. The straight line is a fit for higher temperature with the expected Curie law $\propto 0.11 T^{-1}$. The inset shows the spatial spin-spin correlation density $\xi(\mathbf{r})$ for the lowest temperature, $\beta = 12$.

For small electron number in the clean dot, we checked our PIMC results against other exact results that we obtained ourselves or were available from the literature. An important step to achieve high accuracy is our extrapolation procedure: simulations are done for different discretization step sizes ϵ of the path integral. We can then eliminate the systematic Trotter error by a linear regression for $\epsilon \rightarrow 0$. Performing the PIMC with different Trotter numbers has also the advantages of improving ergodicity and the sign problem.

We have then applied this simulation method to investigate impurity effects for a quantum dot in the incipient Wigner molecule regime. In this stage of beginning crystallization, the numerical description and the physical interpretation are most difficult, yet most interesting. We found that in the clean case, despite of rather strong interactions, the energetic shell structure is still discernible by tiny cusps in the addition energies. The impurity alters the addition spectrum substantially. The shell structure is destroyed, instead we find a new peak at $N = 8$ which comes along with a very unexpected sub-Hund's rule spin $S = 0$. For other electron numbers, the ground-state spin is not altered by the defect. By looking at the spin gap between the low-lying energies we find a tendency towards spin polarization, however, this seems to be a rather weak effect depending on N . The interplay of disorder and interaction

in quantum dots is currently subject of intense theoretical and experimental research; our deformed dot is probably not an example for real disorder, but we can treat the few-electron problem with rather strong interaction and impurity in an exact fashion.

The PIMC method enables us to monitor spin and charge spatial distributions and correlation functions. The onset of Wigner crystallization is clearly enhanced by the symmetry-breaking defect, although we still have strong quantum fluctuations. The charge densities show a peak at the impurity with a surrounding weakly modulated plateau which represents the Wigner molecule. We also investigated the spin sensitivity of the beginning crystallization. Interestingly, this dependency, which is not found in the deep Wigner molecule case, is reinforced by the impurity. The spatial spin-spin correlation function shows rather a Fermi hole than a clear spin ordering. However for small electron number and low temperatures, we were able to monitor this tiny correlation: for our parameters we do not have strong separation of the energy scales of charge and spin fluctuations. Such behavior is only found in the incipient Wigner molecule regime and invalidates a possible lattice-spin model description. These effective Hamiltonians are only appropriate in the deep Wigner-crystallized limit.

We illustrated these findings extensively for the six-electron Wigner molecule. Here, the classical configuration is a pentagon with an electron in the center. We found that both with and without impurity the ground state is unpolarized with antiferromagnetic spin ordering, which mirrors the sixfold geometry. Conversely, for polarized spin one electron clearly enters the center of dot. Enhanced spin sensitivity can also be seen in the spin densities which do not simply follow the charge densities. These spin effects are increased in presence of the defect. Finally, for $N = 6$ we have considered the impurity's susceptibility as a function of temperature. Its behavior is indeed reminiscent of the Kondo effect, i.e. a saturation for low T and a decay for higher T . The detailed form $\chi_z^{\text{imp}}(T)$, however, deviates from the idealized model.

4 Unrestricted Hartree-Fock for quantum dots

In the present chapter we discuss properties, predictions, and limitations of Hartree-Fock (HF) calculations for clean quantum dots. This method has a long tradition in atomic and nuclear physics. *Unrestricted* Hartree-Fock is the best one-particle approximation which takes into account the anti-symmetry of the many-fermion wave function and the interaction. While quantum dots may be considered as tunable two-dimensional (2D) artificial atoms, the electron density can be much smaller than in real atoms and correlations play a more prominent role. This is why for quantum dots the HF method has to be regarded with care. In this work we focus on the crossover from weak to strong Coulomb interaction, i.e. from higher to lower electronic densities. This is equivalent to weakening the external confinement potential for a given host material of the quantum dot.

The physics of this crossover can be sketched as follows. In the case of weak interaction (high density) a one-particle picture is valid: Electrons are filled into the energy shells of the 2D isotropic harmonic oscillator. Here, the appropriate method is Restricted Hartree-Fock (RHF), where every orbital belongs to an energetic shell and has good orbital momentum. This shell filling with Hund's rule was found experimentally in small dots (TARUCHA ET AL., 1996). In the case of strong interaction (low density), one can no longer stay within this simple one-particle picture. WIGNER (1934) has shown that for strong correlation the ground state of the 2D electron gas is described by localized electrons, which form a classical hexagonal crystal. Accordingly, in this limit the electrons in the dot form a small crystal, a so-called Wigner molecule. Therefore the picture of energetic shells is no longer meaningful. One has to improve the HF approximation, and this is done by passing over to unrestricted Hartree-Fock (UHF). This means that the space of the HF trial wave functions is extended, leading to considerably lower energies than with RHF. At the same time the UHF Slater determinant breaks the symmetry of the problem, i.e. spatial and spin rotational invariance. This complicates the interpretation of the UHF solution.

For very strong interaction, UHF is also expected to give reasonable results because a one-particle picture of localized orbitals (e.g. a Slater determinant of spatially localized orbitals) should model the Wigner molecule quite well. In fact, the UHF energies become nearly spin-independent, in accordance with semiclassical and quantum Monte Carlo studies, while this is not the case with RHF. We show that the UHF Hamiltonian for strong interaction has the same spectrum as a tight-binding Hamil-

tonian of a particle hopping between the sites of a Wigner molecule. The hopping matrix element and on-site energies can be extracted from the UHF orbital energies.

The application of the HF method to quantum dots is natural and has been discussed in various recent papers. By comparing to exact PIMC results, we will demonstrate that some of the conclusions drawn on the basis of HF calculations are not based on firm grounds. This is in particular the case, when the HF wave functions are used to describe charge and spin density distributions in a quantum dot. The onset of Wigner crystallization cannot directly be determined from these quantities. On the other hand, UHF will be shown to give rather reliable estimates for the ground-state energies, although the method cannot correctly resolve spin order and addition energies.

In this chapter we give a complete account of UHF calculations for clean quantum dots (REUSCH and GRABERT, 2003). To our knowledge, we are first to discuss the UHF two-electron problem in detail and give an elaborate analysis of the strongly interacting limit and a weak magnetic field. An incomplete version of our results has been presented in an earlier short communication (REUSCH ET AL., 2001). In Sect. 4.1 we present the method and introduce the basic notation. In Sect. 4.2 we obtain explicit results for quantum-dot Helium that already show many features of HF solutions for higher electron numbers presented in Sect. 4.3. In Sect. 4.4 we also discuss the effect of a magnetic field.

4.1 Unrestricted Hartree-Fock method

4.1.1 Hartree-Fock Slater determinant

The HF approximation (FOCK, 1930) consists in approximating the interacting many-electron ground state by a single, optimal Slater determinant

$$|\Psi^{\text{HF}}\rangle = \left(\prod_{i=1}^N \hat{c}_i^\dagger(\text{HF}) \right) |0\rangle . \quad (4.1)$$

Optimal means that this trial wave function gives the lowest ground-state energy $E^{\text{HF}} = \langle \Psi^{\text{HF}} | \hat{H} | \Psi^{\text{HF}} \rangle$ according to the variational principle. Then, the HF one-particle functions, the *orbitals* $|i\rangle = \hat{c}_i^\dagger(\text{HF}) |0\rangle$, fulfill the HF equations (see below), that means they are determined self-consistently¹. In other words, the orbitals form a *mean field* that acts effectively on every single electron. The orbitals do not have to correspond to the unperturbed (atomic or harmonic oscillator) orbitals, which would

¹The derivation of the HF equations can be found in any text book on quantum mechanics. In quantum chemistry (e.g. SZABO and OSTLUND, 1982; PRIMAS and MÜLLER-HEROLD, 1990), (restricted) HF calculations often serve as a reference point for more refined methods. We emphasize, however, that we want to describe a system that is much stronger correlated than electrons in atoms or molecules.

only be true in the weakly interacting case. Furthermore, we want to remark that HF, though being an approximation, is a fully quantum-mechanical method. It is not a semiclassical method, although we are interested in the crossover to the regime of classical electrons.

4.1.2 Hartree-Fock orbitals

The HF orbitals are expanded in a known basis. In our calculation, we have chosen the angular momentum basis of the two-dimensional harmonic oscillator, the Fock-Darwin states Eq. (2.10). The expansion then reads

$$|i\rangle = \hat{c}_i^\dagger(\text{HF}) |0\rangle = \sum_{\substack{n=0,\infty \\ M=-\infty,\infty}} u_{nM}^i |nM\sigma_i\rangle . \quad (4.2)$$

Here, M is the angular and n the radial quantum number of the Fock-Darwin basis and $\sigma_i = \pm 1/2$ is the electron spin of the i -th orbital². Thus only the z -component of the total spin is fixed, $S_z^{\text{tot}} = \sum_i \sigma_i \equiv S_z$. In a practical calculation, the number of basis functions is finite. For $N \leq 8$ we used up to 55 basis functions per spin direction (up to an energy of $10\hbar\omega_0$).

We want to point to some features of the expansion (4.2). The orbitals are no longer eigenfunctions of the one-particle angular momentum. Therefore, as we shall see explicitly below, the HF Slater determinant is not an eigenstate of the total angular momentum, it breaks the symmetry of the original Hamiltonian. Another possibility is to give each orbital i a fixed angular momentum M_i . This restricted HF (REUSCH, 1998) preserves the total angular momentum but yields higher ground-state energies. Giving up the symmetry is thus necessary to obtain useful results within the one-particle picture of HF³. Still another possibility would be to build a Slater determinant of spatially localized orbitals for the strongly interacting case (SUNDQVIST ET AL., 2002) or of multicenter localized orbitals in high magnetic field (SZAFRAN ET AL., 2003) and vary position and shape of these orbitals to minimize the HF energy. Our orbitals fulfill the HF equations (see below), they are self-consistent and best adapted to study the crossover from weak to strong correlation.

4.1.3 Breaking of rotational symmetry

To show explicitly the breaking of rotational symmetry, we consider the total angular momentum $L_z^{\text{tot}} = \sum_{i=1}^N L_z^{(i)}$ in the HF basis $\hat{c}_i^\dagger(\text{HF}) = \sum_\alpha u_\alpha^i \hat{a}_\alpha^\dagger$ (where \hat{a}_α^\dagger is the

²Each orbital has its own fixed spin, that is to say there is no double occupancy of orbitals with spin up and down, but there are different orbitals for different spins.

³One can say that breaking a symmetry implies that correlations are partly taken into account in spite of the one-particle description (see e.g. RING and SCHUCK, 1980; LIPKIN, 1960).

creator in the angular momentum basis, i.e. $\hat{a}_\alpha^\dagger |0\rangle \equiv |n_\alpha M_\alpha\rangle$)

$$\hat{L}_z^{\text{tot}} = \sum_{i,j} \langle i | L_z | j \rangle \hat{c}_i^\dagger(\text{HF}) \hat{c}_j(\text{HF}) \equiv \hat{L}. \quad (4.3)$$

As \hat{H} and \hat{L} commute, the exact, non-degenerate ground state must be an eigenstate of \hat{L} . On the other hand, if we calculate the expectation value for the UHF ground state

$$\langle \Psi^{\text{HF}} | \hat{L} | \Psi^{\text{HF}} \rangle = \sum_{i=1}^N \langle i | L_z | i \rangle = \sum_{i=1}^N \sum_{\alpha} |u_\alpha^i|^2 M_\alpha, \quad (4.4)$$

one sees that the result is not necessarily integer. However, only eigenstates of the total angular momentum are rotationally invariant, since L_z^{tot} is the infinitesimal generator of a rotation of the system. A finite rotation by angle α is given by

$$\exp \{ i\alpha L_z^{\text{tot}} \} \Psi = \exp \{ i\alpha M^{\text{tot}} \} \Psi, \quad (4.5)$$

if and only if $L_z^{\text{tot}} \Psi = M^{\text{tot}} \Psi$.

4.1.4 Numerical procedure

In the diploma thesis (REUSCH, 1998) the RHF ground state was found by parameterizing and minimizing the RHF energy functional. Now, with the UHF approach the dimensionality of the problem is strongly increased, in particular the matrix u_{nM}^i is no longer block diagonal (except with respect to spin). Thus the parameter space gets to big and a minimization is no longer effective. Therefore we seek for the UHF ground state by iterative diagonalization of the HF equations,

$$\sum_{\alpha} \{ \langle \gamma | h | \alpha \rangle + \sum_{\beta\beta'} (\gamma\beta | w | \alpha\beta') \rho_{\beta'\beta} \} u_\alpha^k = \varepsilon_k u_\gamma^k. \quad (4.6)$$

Here, Greek indices abbreviate the quantum numbers of the basis (2.10), e.g. $\alpha \equiv (n_\alpha M_\alpha \sigma_\alpha)$, and $\langle \gamma | h | \alpha \rangle$ is the matrix element of the one-particle Hamiltonian (2.9). Further,

$$(\alpha\alpha' | w | \beta\beta') = \langle \alpha\alpha' | w | \beta\beta' \rangle - \langle \alpha\alpha' | w | \beta'\beta \rangle \quad (4.7)$$

is the anti-symmetrized Coulomb matrix element, which we have obtained by transformation to relative and center of mass coordinates (REUSCH, 1998). Now, we start with an initial guess for the density matrix

$$\rho_{\alpha\alpha'} = \sum_{i=1}^N u_\alpha^i u_{\alpha'}^{i*}. \quad (4.8)$$

Then we diagonalize (4.6) and obtain new expansion coefficients u_{nM}^i and from these a new density matrix (4.8). This process is iterated until a stable, self-consistent solution is obtained.

Clearly, this solution could be merely a local minimum and not the HF ground state. Therefore the iteration has to be stable over many cycles and, above all, one has to try several initial guesses for the density matrix $\rho_{\alpha\alpha'}$. The initial guess should not contain any symmetries which would pass over to the HF Hamiltonian Eq. (4.6) and steadily be iterated. Typically we used about 500 to 1000 iterations. The true minimum can also be identified by its one-particle density,

$$n^{\text{HF}}(\mathbf{r}) = \sum_{i=1}^N |\varphi_i(\mathbf{r})|^2, \quad (4.9)$$

which in the strong coupling limit mirrors the geometry of classical electrostatic point-charges as we discuss below.

4.1.5 Orientational degeneracy

In principle the orientation of the deformed symmetry-breaking HF solution is arbitrary. This fact is due to the rotational invariance of the original Hamiltonian and can be called orientational degeneracy. The HF solution one finds has a special orientation and depends on the initial guess for the density matrix $\rho_{\alpha\alpha'}$. Any desired orientation can be obtained by applying $\exp(i\alpha L_z^{\text{tot}})$ to the Slater determinant.

At this point we have to add a remark which is also of relevance for numerics. When we consider a quantum dot in zero magnetic field, our Hamiltonian is invariant under time reversal. Thus we can choose real expansion coefficients u_{nM}^i in (4.2). However, then the HF one-particle density is always symmetric to one axis. We show this for the density of one orbital $\varphi_i(\mathbf{r}) \equiv \langle \mathbf{r} | i \rangle$

$$|\varphi_i(\mathbf{r})|^2 = \sum_{\alpha,\beta} u_{\alpha}^{i*} u_{\beta}^i e^{i(M_{\beta}-M_{\alpha})\varphi} R_{\alpha}(r) R_{\beta}(r), \quad (4.10)$$

where R stands for the radial part of the basis. If the coefficients u_{α}^i are real

$$|\varphi_i(\mathbf{r})|^2 = 2 \sum_{\alpha>\beta} u_{\alpha}^i u_{\beta}^i \cos[(M_{\beta} - M_{\alpha})\varphi] R_{\alpha}(r) R_{\beta}(r) + \sum_{\alpha} [u_{\alpha}^i R_{\alpha}(r)]^2 \quad (4.11)$$

and the total density is symmetric to the axis from where the polar angle φ is measured. Only with complex coefficients u_{α}^i does one obtain an arbitrary orientation of the density.

4.2 Unrestricted Hartree-Fock for quantum-dot Helium

In this section, we present UHF energies and densities for the two-electron quantum dot (quantum-dot Helium). This illustrates the basic concepts and properties of the HF approximation, and reveals features that are also important for higher electron numbers. We compare with exact results obtained by diagonalization of the relative motion (cf. Sec. 3.2.1). We also compare with the RHF method, in order to illustrate the differences to UHF.

The UHF two-electron problem has been treated previously by YANNOULEAS and LANDMAN (2000b). However, we find some deviations from their results. An extensive discussion of the properties of the RHF quantum-dot Helium for $\lambda \approx 2$ can be found in PFANNKUCHE ET AL. (1993).

4.2.1 Two-electron Slater determinant

The Slater determinant for two electrons with $S_z = 0$ is

$$\Psi^{\text{HF}} = \frac{1}{\sqrt{2}} [\varphi_1(\mathbf{r}_1)\varphi_2(\mathbf{r}_2)\chi_+^1\chi_-^2 - \varphi_1(\mathbf{r}_2)\varphi_2(\mathbf{r}_1)\chi_+^2\chi_-^1]. \quad (4.12)$$

Here we have displayed the orbital and spin parts of the wave function explicitly, χ_{\pm}^i is the spin of the i -th electron. The state Ψ^{HF} is generally not an eigenstate of the total spin S_{ges}^2 . In order to obtain a singlet one has to set $\varphi_1 = \varphi_2$, and thus

$$\Psi^{\text{HF}} = \varphi_1(\mathbf{r}_1)\varphi_1(\mathbf{r}_2)\chi_{\text{singlet}}. \quad (4.13)$$

This restriction is also called *closed-shell* HF (CSHF), because if every orbital is filled with spin up and down, open shells are impossible. One sees very clearly from (4.12) that the Slater determinant violates the symmetry of the problem. For two electrons, the spin symmetry is easily restored, namely by a superposition of two Slater determinants with spin up/down and down/up. For the polarized case $S_z = 1$, total spin is conserved, and the HF wave function is a product of a symmetric spin function and an anti-symmetric orbital function.

4.2.2 Different HF approximations

Now we want to compare the energies of different HF approximations. These differ in the numerical effort, however, for today's computer, the most general solution of the problem involves diagonalizing a 50x50 matrix a thousand times, which is a child's play. We compare with the results of an exact diagonalization⁴.

⁴Since we know the Coulomb matrix elements explicitly, a diagonalization of the relative motion of two electrons (Sec. 3.2.1) is easier than an evaluation of the analytic solution in terms of power series (TAUT, 1993).

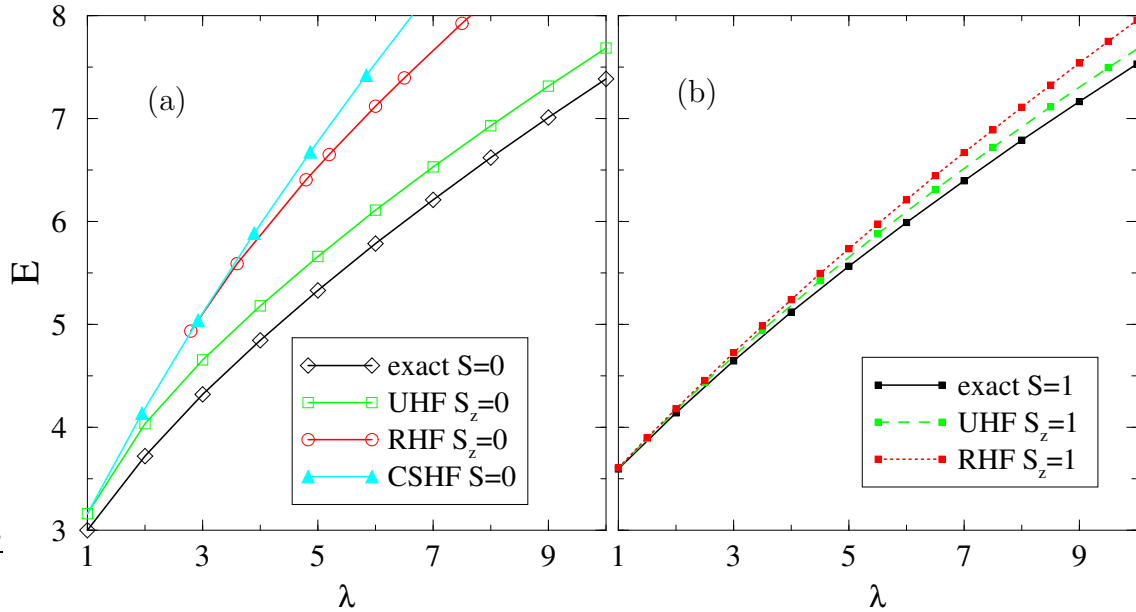


Fig. 4.1: Comparison of different HF energies with the exact energies vs. the coupling constant λ . (a) $S = 0$, (b) $S = 1$.

First we consider the case $S_z = 0$. The most general ansatz for the HF orbitals is the UHF state (4.2), a spin-dependent expansion which includes arbitrary angular momentum. Less general is the RHF ansatz, where angular momentum is preserved. And still less general is CSHF (4.13), when we force the two electrons to occupy two identical (rotationally symmetric) orbitals. In Fig. 4.1 one can clearly see the importance of breaking the symmetry to obtain lower HF energies. Up to $\lambda \approx 1$ all three methods give nearly the same result. Up to $\lambda \approx 3$ the closed-shell energy is equal to the RHF energy. This means that from this point on the two RHF orbitals are no longer identical. As expected, the UHF energy is lowest. For $S_z = 1$, one has a triplet, and total spin is conserved. One needs two different orbitals, there is no CSHF.

In Fig. 4.2 we show the differences of the HF energies from the energy of the exact ground state which is the singlet. In the spin-polarized case, UHF gives lower energies than RHF, but the gain in energy is not as big as in the unpolarized case. Interestingly, the UHF energies become spin-independent with increasing λ : Above $\lambda \approx 4$ they agree within about 0.3%, the $S_z = 1$ state is somewhat lower than the $S_z = 0$ state⁵. The exact energies merge more slowly: For $\lambda = 20$ the energy difference between singlet and triplet is still about 1%. Note that the RHF energies fail to become spin-independent for large λ , which leads to overestimate the spin gap.

⁵This is probably due to the exchange term which lowers the HF energy for parallel spins. In fact, exchange integrals are always positive (for a proof see SLATER, 1960, App. 19).

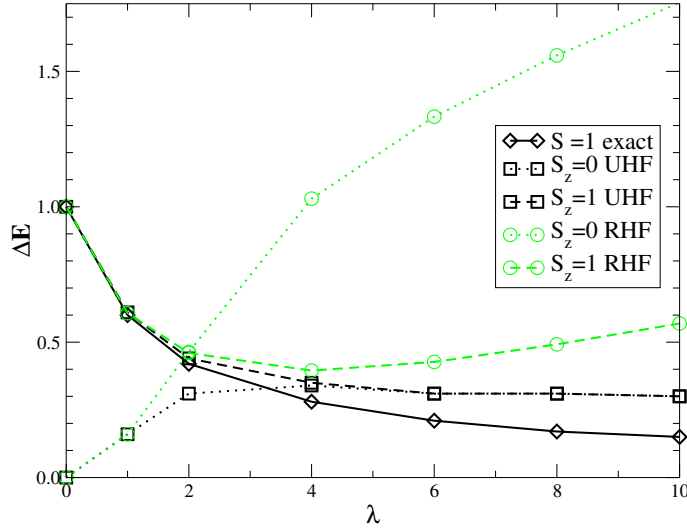


Fig. 4.2: Absolute energy differences with respect to the exact ground state $\Delta E = E_S - E_{\text{GS}}^{\text{exact}}$. Above $\lambda \approx 4$ the two UHF energies are nearly the same.

Of course, one expects spin-independent energies in the classical limit of localized electrons without overlap. However, as we will illustrate below, the UHF orbitals are not localized.

4.2.3 UHF one-particle densities

Now we want to have a closer look at the one-particle density which is just the sum of the densities of the two orbitals,

$$n^{\text{HF}}(\mathbf{r}) = |\varphi_1(\mathbf{r})|^2 + |\varphi_2(\mathbf{r})|^2. \quad (4.14)$$

In Fig. 4.3 we show this density for different values of the coupling parameter λ . Already for a relatively small λ , we detect two azimuthal maxima. The density is strongly anisotropic which is due to the symmetry breaking (see Sec. 4.1.5). In the case of $S_z = 1$ the two maxima are more distinct as a consequence of the Pauli principle because polarized electrons are stronger correlated. However, the direct interpretation of the two dips as localized electrons is questionable: with increasing λ the azimuthal modulation first *decreases*, then for $\lambda \gtrsim 8$ ($\lambda \gtrsim 10$ for $S_z = 1$) it increases again. For very high λ the densities become almost spin-independent. A closer view reveals that the azimuthal maxima are more distinct for the case $S_z = 0$. This can be understood by remembering the exchange term in the HF energy which lowers the energy for strong interaction and overlapping spin-polarized orbitals. Thus the orbitals are less localized for $S_z = 1$ as we show explicitly below.

While the azimuthal modulation is an artifact of the HF approximation, the densities display correctly a minimum in the center which gets deeper with stronger

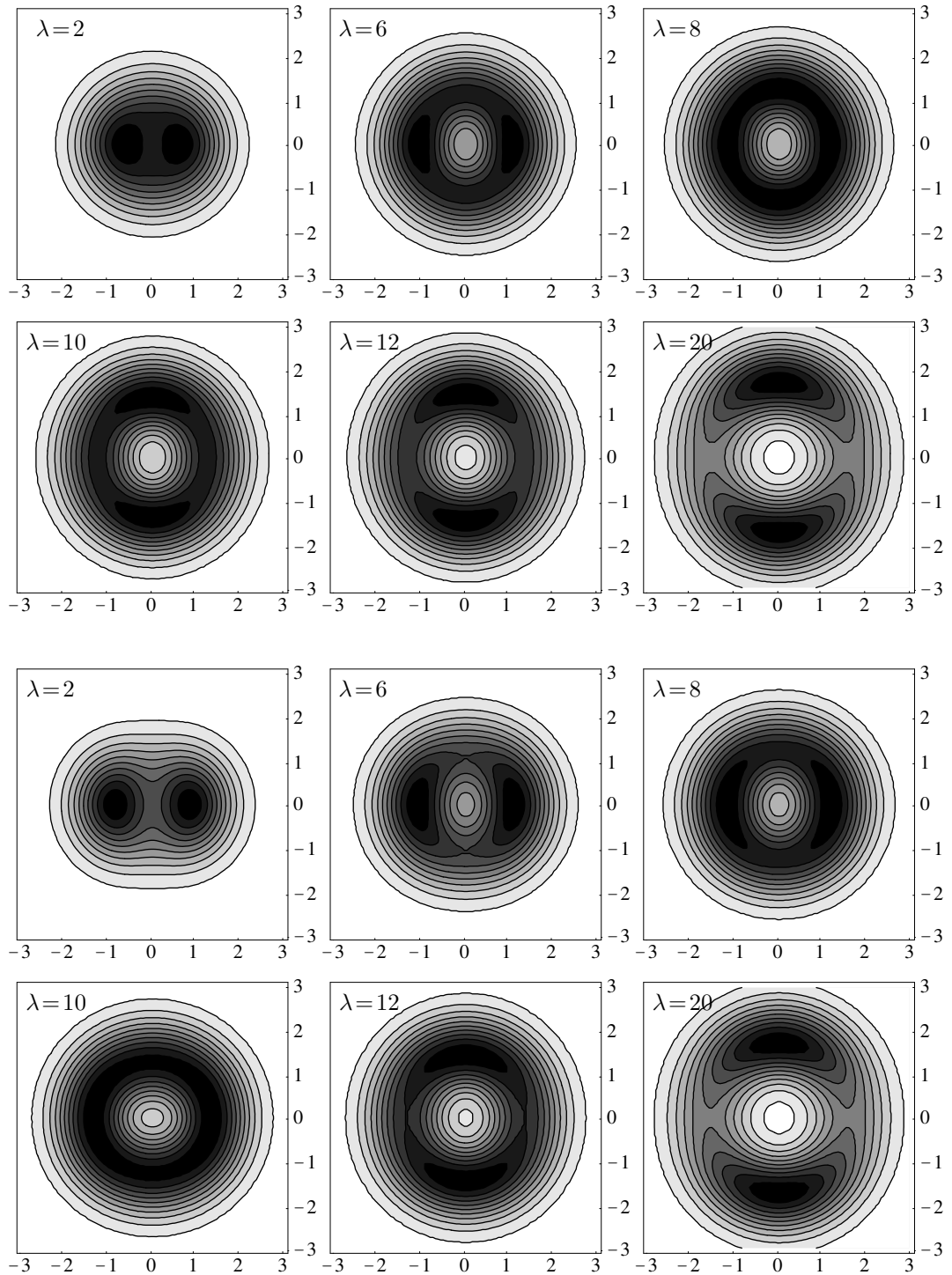


Fig. 4.3: Shaded contour plots of the HF single particle densities for quantum-dot Helium and different values of the interaction. $S_z = 0$ upper part, and $S_z = 1$ lower part. One contour corresponds to 1/10 of the maximal density.

interaction. Also, the maxima are in very good agreement with the classical positions $r_a = \sqrt[3]{\lambda/4}$ (see Sec. 2.8).

4.2.4 UHF orbitals

In order to understand the form of the UHF densities it is necessary to have a closer look at the UHF orbitals. For $S_z = 0$, we obtain two orbitals that are exactly complex conjugate, $\varphi_1 = \varphi_2^*$ (Fig. 4.4). This can be seen by studying the expansion coefficients u_{nM} in Eq. (4.2) and means that the Slater determinant is symmetric under time reversal⁶.

For $S_z = 1$, the two orbitals depicted in Fig. 4.5 are always different and can be chosen real. One can easily see how the total density is composed of the two orbital densities. For $\lambda = 2$, one can still interpret the orbitals in the energy shell picture like with RHF: The first orbital is (approximately) round, S-like, and the second one is dumbbell formed, P-like⁷. This gives (again approximately) a total angular momentum $M_{\text{tot}} = \pm 1$. The deformed Slater determinant and the dumbbell formed density can be seen as a superposition of opposite angular momenta, resulting in a standing wave (see below).

For very high $\lambda \gtrsim 14$, there is a simple relation between the orbitals for both spin polarizations. If for $S_z = 1$ we choose both orbitals real, we find

$$\varphi_{1/2}^{S=0} \approx \frac{1}{\sqrt{2}}(\varphi_1^{S=1} \pm i\varphi_2^{S=1}). \quad (4.15)$$

In this fashion, we see that $\varphi_{1/2}^{S=0}$ are complex conjugate and approximately orthonormal, since we have made an unitary transformation. We have thus obtained orthogonal Hartree orbitals, because there is no exchange term for $S_z = 0$. In Fig. 4.6 we show that the overlap $\langle \varphi_1^{S=0} | \varphi_2^{S=0} \rangle$ vanishes exponentially with increasing λ (cf. Fig. 4.13).

To shed more light on this behavior we consider now the orbital energies⁸. We start with the HF Hamiltonian in the HF basis for $S_z = 1$

$$\begin{pmatrix} \varepsilon_1 & 0 \\ 0 & \varepsilon_2 \end{pmatrix} = \begin{pmatrix} h_{11} + w_{1212} & 0 \\ 0 & h_{22} + w_{1212} \end{pmatrix}. \quad (4.16)$$

⁶This finding is in conflict with the results of YANNOULEAS and LANDMAN (2000b). They find two different UHF orbitals, which then give rise to another conditional probability density (see Sec. 4.2.5). Seemingly (see also YANNOULEAS and LANDMAN, 2002) they find (or use) spatially localized orbitals. We do not find localized orbitals and this is to be expected in view of the rotational invariance of the problem (e.g. there are no localized orbitals in a benzene ring). However, in the limit of strong interaction one can build a Slater determinant of spatially localized orbitals, e.g. of Gaussians located at the classical positions (SUNDQVIST ET AL., 2002) and this should give nearly the same variational energy (see comment in Sec. 4.4.3).

⁷An orbital with angular momentum $M = 1$ has an isotropic density. Superposition of $M = \pm 1$ orbitals gives a dumbbell formed density.

⁸For an interesting exact property of HF orbital energies see BACH ET AL. (1994).

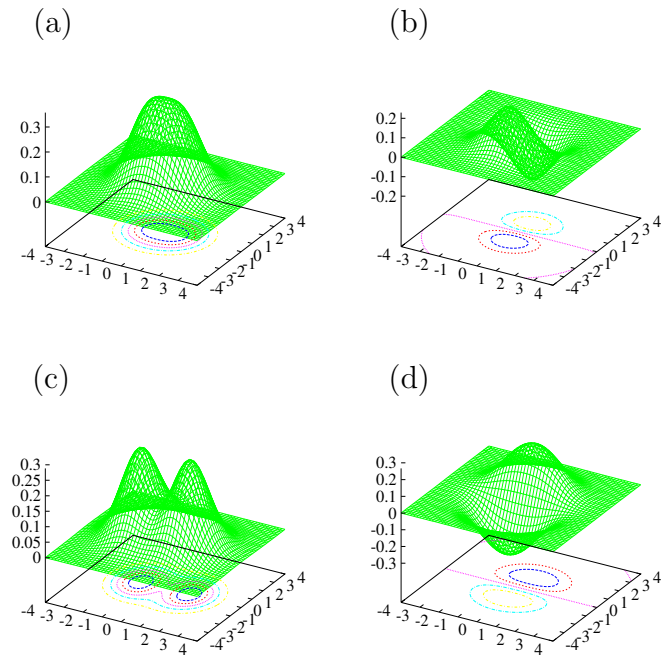


Fig. 4.4: UHF orbitals for $N = 2$, $S_z = 0$. (a), (b) real and imaginary part of φ_1 at $\lambda = 2$. (c), (d) real and imaginary part at $\lambda = 8$. The second orbital is always complex conjugate.

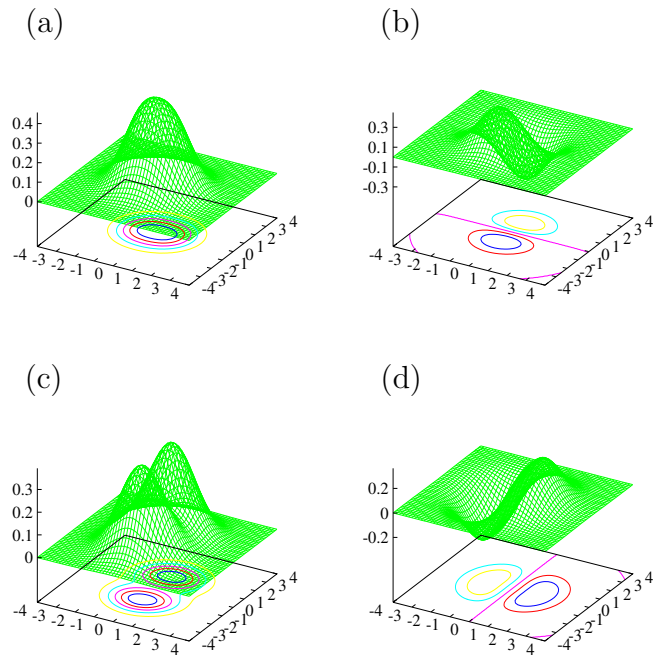


Fig. 4.5: Pairs of real UHF orbitals for $N = 2$, $S_z = 1$. (a), (b) at $\lambda = 2$. (c), (d) at $\lambda = 10$.

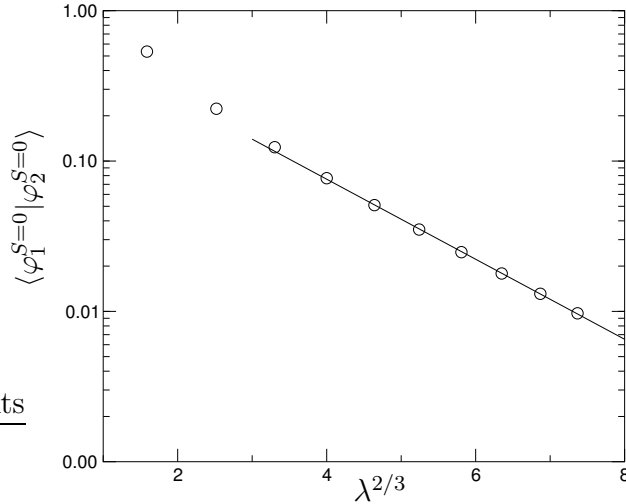


Fig. 4.6: Log-linear plot of overlap $\langle \varphi_1^{S=0} | \varphi_2^{S=0} \rangle$ vs. $\lambda^{2/3}$. For $\lambda \geq 8$, the line of best fit is shown.

Here, we use the notation $h_{ij} = \langle i | h | j \rangle$ and $w_{ijkl} = \langle ij | w | kl \rangle$ for matrix elements in the HF basis. When we apply the unitary transform (4.15),

$$\frac{1}{2} \begin{pmatrix} 1 & i \\ 1 & -i \end{pmatrix} \begin{pmatrix} \varepsilon_1 & 0 \\ 0 & \varepsilon_2 \end{pmatrix} \begin{pmatrix} 1 & 1 \\ -i & i \end{pmatrix} = \begin{pmatrix} U & -t \\ -t & U \end{pmatrix} = H_2, \quad (4.17)$$

we obtain a two-state Hamiltonian H_2 , with on-site energy $U = (h_{11} + h_{22} + 2w_{1212})/2$ and tunnel splitting $t = (h_{22} - h_{11})/2$. Thereby, we have mapped the HF Hamiltonian on a lattice model. It is intuitive that for strong interaction the two electrons localize, and thus a tight-binding approach should become physically correct.

Now we want to show that the transformation (4.15) is just the one which yields so-called *localized orbitals*. It is known from quantum chemistry that HF orbitals are always very badly localized, because they should maximize the exchange term of the HF energy (PRIMAS and MÜLLER-HEROLD, 1990). In order to obtain localized orbitals, one can make a unitary transformation within occupied states, e.g. by minimizing the exchange energy⁹.

For $S_z = 0$, there is *no* exchange term in the HF equations, and these lead to the Hartree orbitals of Eq. (4.15). On the other hand, the transformed Hamiltonian (4.17) for $S_z = 1$ reduces for very small tunneling, i.e. strong interaction, to

$$H'_2 = \begin{pmatrix} U & 0 \\ 0 & U \end{pmatrix} \equiv \frac{1}{2} \begin{pmatrix} \varepsilon_1 + \varepsilon_2 & 0 \\ 0 & \varepsilon_1 + \varepsilon_2 \end{pmatrix}. \quad (4.18)$$

⁹This is the criterion of localization given by EDMINDSTON and RUEDEBERG (1963). These new orbitals then no longer fulfill the HF equations, but form the same Slater determinant, and thus give the same expectation values for the energy and densities. Localization in this sense does not necessarily mean that these orbitals are restricted to certain parts of space (EDMINDSTON and RUEDEBERG, 1963).

Hence, for large λ , it coincides with the HF Hamiltonian for $S_z = 0$, so that $\varepsilon_{1/2}^{S=0} \approx (\varepsilon_1^{S=1} + \varepsilon_2^{S=1})/2$. Already for $\lambda = 14$, we have $\varepsilon_{1/2}^{S=0} = 6.83$ and $\varepsilon_1^{S=1} = 6.71$, $\varepsilon_2^{S=1} = 6.95$ corresponding to a small splitting $t = 0.12$ in H_2 . We will discuss in general how the HF Hamiltonian maps on a lattice model in Sec. 4.3.4 and show how t depends on λ .

4.2.5 UHF two-particle densities

Here we examine the conditional probability density (CPD) for finding one electron at \mathbf{x} , under the condition that another electron is at \mathbf{y} . For quantum-dot Helium and $S_z = 0$ the CPD reads

$$n^{\text{HF}}(\mathbf{x}|\mathbf{y}) = \frac{|\varphi_1(\mathbf{x})|^2|\varphi_2(\mathbf{y})|^2 + |\varphi_1(\mathbf{y})|^2|\varphi_2(\mathbf{x})|^2}{n^{\text{HF}}(\mathbf{y})}. \quad (4.19)$$

Now, since we found complex conjugate orbitals, $\varphi_1 = \varphi_2^*$, we have $n^{\text{HF}}(\mathbf{x}|\mathbf{y}) = n^{\text{HF}}(\mathbf{x})$, i.e. the CPD is independent of the condition. This is not too astonishing, because within the HF method two electrons are only correlated by the exchange term, which vanishes here.

For $S_z = 1$, the orbitals are different from each other and the CPD is given by

$$n^{\text{HF}}(\mathbf{x}|\mathbf{y}) = \{|\varphi_1(\mathbf{x})|^2|\varphi_2(\mathbf{y})|^2 + |\varphi_1(\mathbf{y})|^2|\varphi_2(\mathbf{x})|^2 - 2\text{Re}[\varphi_1^*(\mathbf{x})\varphi_2(\mathbf{x})\varphi_1(\mathbf{y})\varphi_2^*(\mathbf{y})]\}/n^{\text{HF}}(\mathbf{y}). \quad (4.20)$$

In Fig. 4.7 we show contour plots of UHF CPDs for different coupling constants and given positions \mathbf{y} . In the upper row, for $\mathbf{y} = (2, 0)$, we find for small $\lambda = 2$ a suggestive result: the density has a single maximum at a distinct distance of the fixed coordinate \mathbf{y} . With increasing λ , however, we obtain two maxima, which develop more and more and are not at all located at the classical position.

The situation is likewise irritating when one chooses $\mathbf{y} = (0, 2)$ as fixed coordinate (lower row). While the exact CPD is rotationally symmetric when both \mathbf{x} and \mathbf{y} are rotated, the UHF CPD does not respect this symmetry. The reason for this lies in the symmetry-breaking and because the UHF approximation cannot completely account for correlations¹⁰. The UHF Slater determinant is deformed and derived quantities do not have necessarily a direct physical meaning, except for the UHF energy which is a true upper bound for the exact energy. Furthermore, it is clear how one could improve the situation, namely by restoring the symmetry. This can

¹⁰Here we disagree with YANNOULEAS and LANDMAN (2000b) who state that the degree of Wigner crystallization can be extracted from the UHF CPD. Building a Slater determinant a priori from spatially localized orbitals may lead to a reasonable CPD, but the UHF orbitals are determined self-consistently.

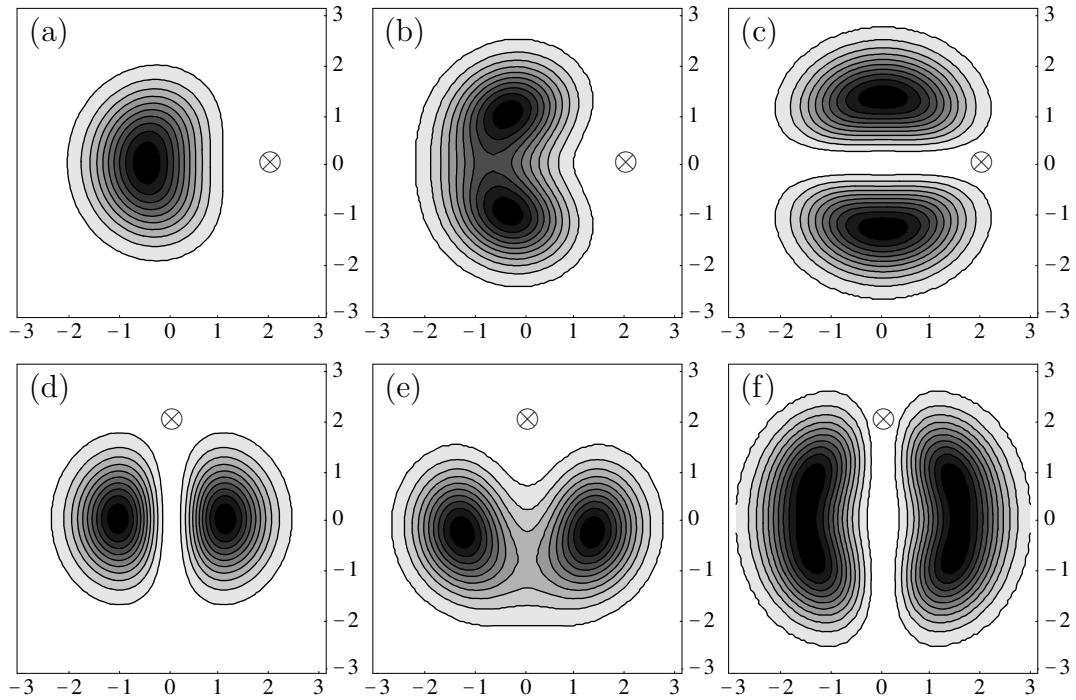


Fig. 4.7: Conditional probability density $n^{\text{HF}}(\mathbf{x}|\mathbf{y})$. In the upper row $\mathbf{y} = (2, 0)$ (\otimes) and (a) $\lambda = 2$, (b) $\lambda = 6$, (c) $\lambda = 10$. Lower row $\mathbf{y} = (0, 2)$ (\otimes) with (d) $\lambda = 2$, (e) $\lambda = 10$, (f) $\lambda = 18$.

be done by projecting the single Slater determinant on a multi Slater determinant state with good total angular momentum (RING and SCHUCK, 1980)

$$\Psi^{\text{Symm}} = \int_0^{2\pi} \frac{d\alpha}{2\pi} \exp \{i\alpha (L_z^{\text{ges}} - M^{\text{tot}})\} \Psi^{\text{HF}}. \quad (4.21)$$

This projection has been performed for two electrons in a recent work by YANNOULEAS and LANDMAN (2002).

4.3 Unrestricted Hartree-Fock for higher electron numbers

In this section we show further results of UHF calculations, namely energies and densities for up to eight electrons. Many effects are similar to what we have already seen for two electrons, for example the errors of the UHF energies and their spin dependence. An interesting phenomenon shown by the UHF densities is the even-odd effect discussed below.

4.3.1 UHF energies

For $N > 2$, we compare the UHF energies with results of a Quantum Monte Carlo (QMC) simulation by EGGER ET AL. (1999) and our own QMC results. This data was obtained for a very low temperatures, $k_B T \leq 0.125 \hbar \omega$. The QMC energies are always below the HF energies and can therefore be considered as effective zero temperature reference points. In Fig. 4.8 we show the relative error for various electron numbers and spins.

For $N = 3$, QMC and also a semiclassical analysis (HÄUSLER, 2000) as well as an exact diagonalization study (MIKHAILOV, 2002a), predict a transition from the $S = 1/2$ ground state in the weakly interacting case to a $S = 3/2$ ground state for $\lambda \gtrsim 4$. The UHF ground state, however, is already spin-polarized for $\lambda \gtrsim 2$. In Fig. 4.8 one can see that the relative error for $S_z = 3/2$ is small, less than 3%. In the non-polarized case, the error is higher, about 7% for $\lambda = 2$. With increasing N and λ , the relative error becomes smaller because the absolute energies are higher. In general, we can say that for the non-polarized states at $\lambda = 2$, the relative error is largest, whereas it is much smaller for the spin-polarized states. Therefore UHF also fails to give correct addition energies (2.3), e.g. $\Delta^{\text{HF}}(2) = 1.34$, for $\lambda = 2$, while the exact value is $\Delta(2) = 1.72$.

In Fig. 4.9 we show the absolute energy differences from the QMC ground state for five and eight electrons. For intermediate values of λ , the UHF energies become already nearly spin-independent, whereas the QMC energies approach this semiclassical behavior more slowly. For stronger interaction, the UHF ground state is always spin-polarized¹¹. Thus the UHF method can not resolve the correct spin ordering of the energies. For $N = 5$, QMC and also semiclassics predict a total spin $S = 1/2$ for all coupling constants λ . This is also the spin in the energy shell model. HF can find this ground-state spin only up to $\lambda \approx 2$. For $N=8$ the QMC method predicts a transition of the total spin from $S=1$ to $S=2$ near $\lambda \approx 6$. The UHF method finds a polarized ground state with $S=4$ for $\lambda \gtrsim 4$. Here, however, the energy differences for different spins are already quite small.

Thus one can conclude that the UHF Slater determinant with fixed spin structure is still a poor description of the total many-electron wave function. Essentially, UHF renders the properties of the spin-polarized solution for larger λ . This can also be seen in the UHF densities which become spin-independent for larger interaction (see below). Finally we briefly mention the RHF results: There the HF energies do not become spin-independent (REUSCH, 1998), but the energies for lower spins are considerably higher for large λ . For large λ , RHF does not give a satisfying estimate of the ground-state energy (see Fig. 4.2).

¹¹For small interaction, UHF can also *underestimate* the spin, e.g. for $N = 4$, $\lambda = 2$ the UHF ground state has $S_z = 0$ (see Fig. 4.8) instead of the correct $S = 1$ (Hund's rule).

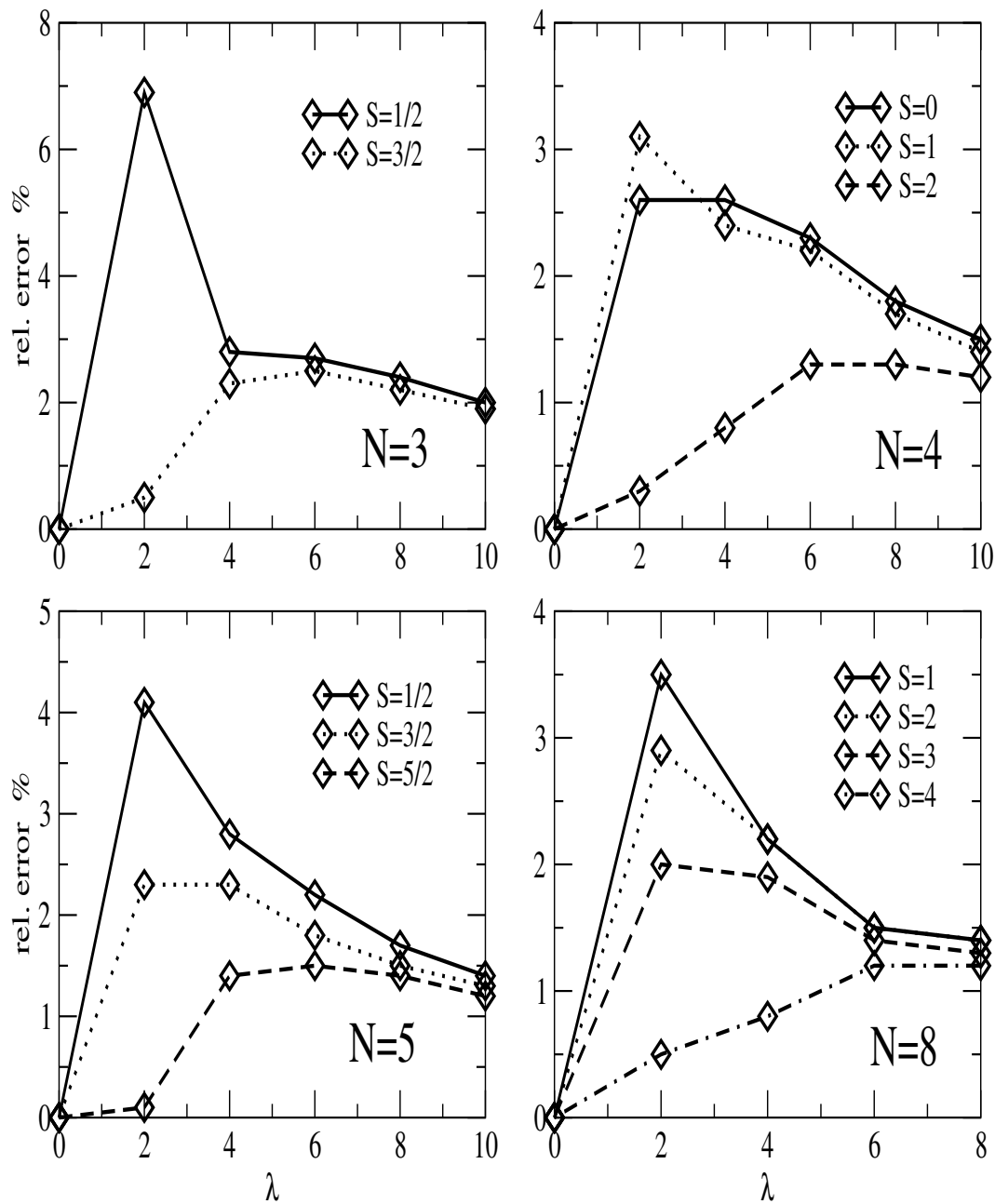


Fig. 4.8: Relative error of the UHF energies $(E_S^{\text{HF}} - E_S^{\text{QMC}})/E_S^{\text{QMC}}$ for various electron numbers and spins vs. coupling constant λ .

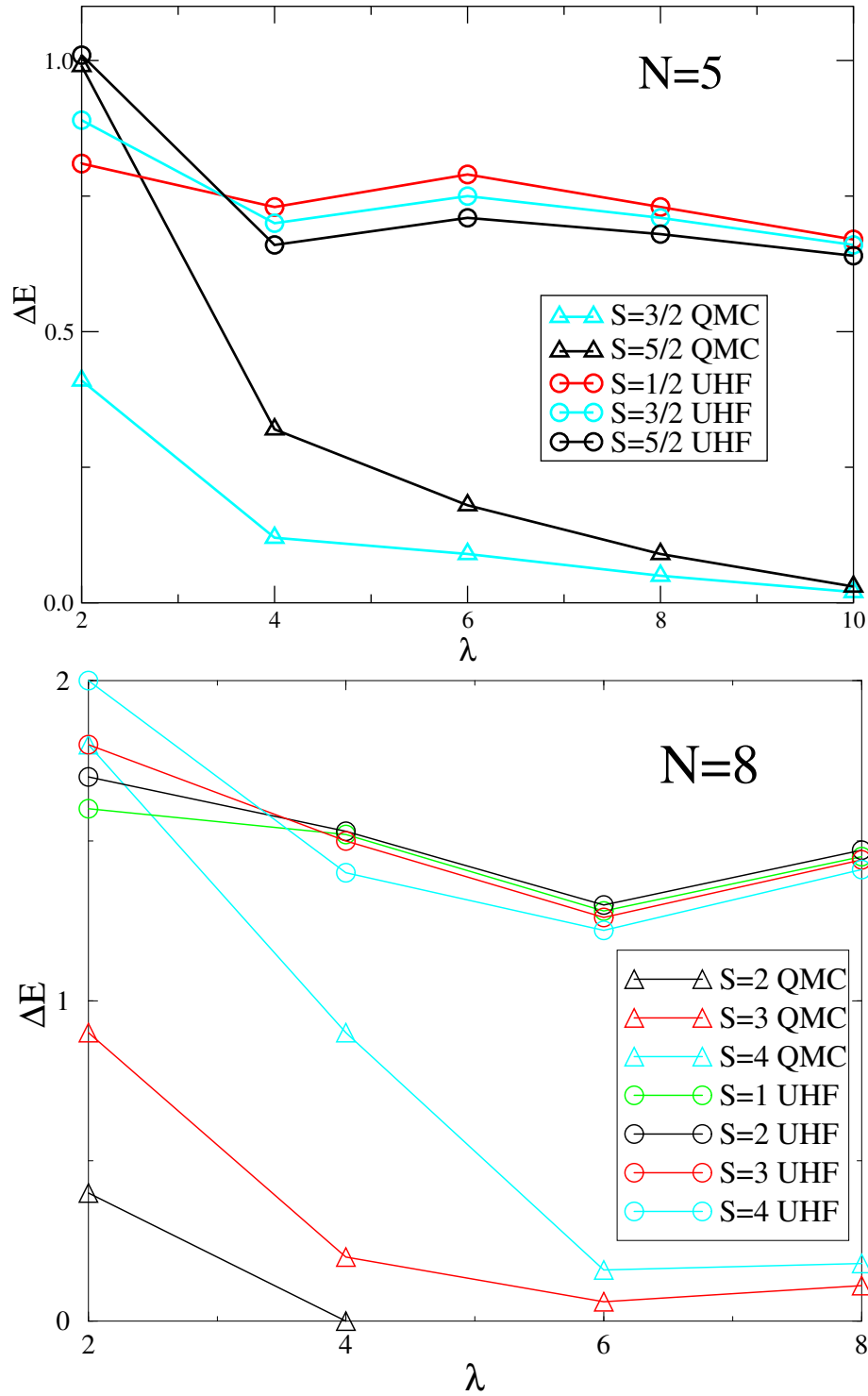


Fig. 4.9: Absolute energy differences from the QMC ground state, $\Delta E = E_S - E_{\text{GS}}^{\text{QMC}}$ for five and eight electrons and various spins vs. coupling constant λ .

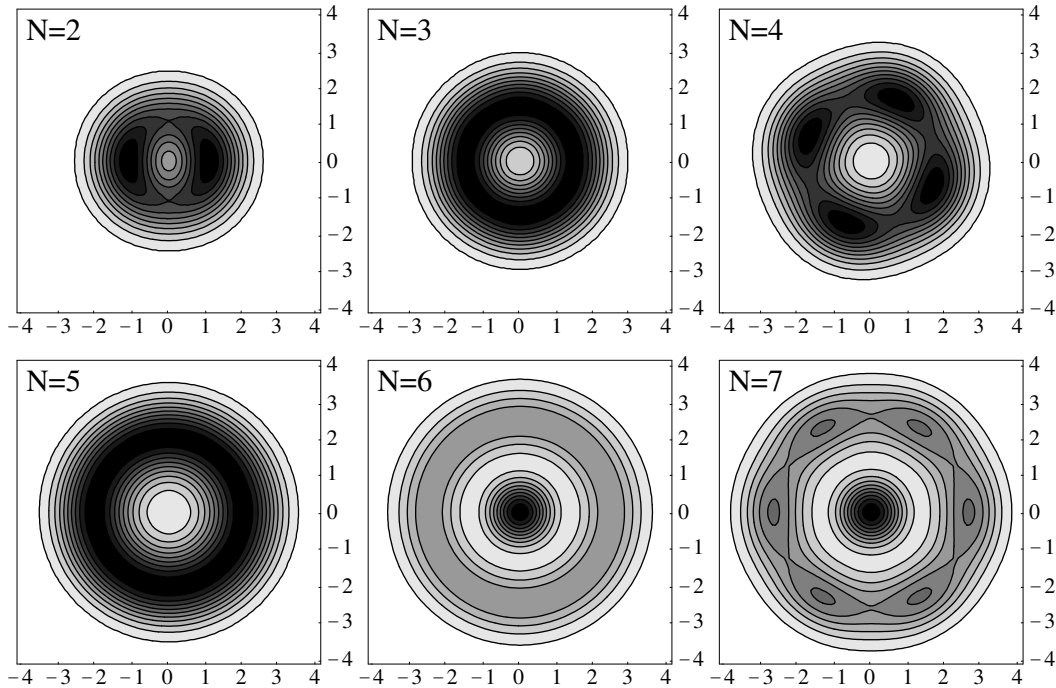


Fig. 4.10: HF one-particle densities n^{HF} for $\lambda = 6$, various electron numbers N and polarized spin $S_z = N/2$.

4.3.2 HF densities: Even-odd effect

In this subsection we consider the UHF densities for higher electron numbers. We find an even-odd effect that may seem quite counter-intuitive at first glance, but can be explained easily. We first show in Fig. 4.10 the densities for rather strong coupling constant $\lambda = 6$, various electron numbers N and $S_z = N/2$. Above this interaction strength, the UHF densities are essentially the same for all S_z and do not change qualitatively with increasing λ (except for $N = 2$, see above).

Surprisingly, only for some N one obtains a molecule-like structure, i.e. an azimuthal modulation that we had already seen for two electrons. For three and five electrons the density is apparently rotationally symmetric, and also for six electrons, where we have a pronounced maximum in the center. The naively expected structure shows up only for $N = 2, 4$ and 7 . Thus, when we consider also $N = 8$ (see below) we recognize that the azimuthal maxima occur only for an even number of electrons per spatial shell. In stating this we want to emphasize that all the densities shown belong to symmetry-breaking, deformed Slater determinants.

This even-odd effect is also surprising, because UHF calculations for quantum dots in a strong magnetic field, MÜLLER and KOONIN (1996) found molecule-like densities for all electron numbers. Naively, one would expect a similar behavior in

the case of strong interaction. We also have performed calculations with a magnetic field that reproduce the densities of MÜLLER and KOONIN (1996)¹² and show that the molecule-like structure disappears for odd N and vanishing field. In the UHF study of YANNOULEAS and LANDMAN (1999) the even-odd effect is not mentioned. They show in Fig. 2(c) for $N=6$ a density with five maxima on a ring and a central maximum which disagrees with our results.

A physical explanation of the even-odd effect combines the geometry of the classical system with the symmetry of quantum mechanics (RUAN ET AL., 1995). Consider the *exact* spin-polarized N -electron wave function Ψ_N for the Wigner molecule case. Due to the strong Coulomb repulsion, the electrons move on an N -fold equilateral polygon (for $N < 6$, for $N = 6$ one electron enters the center of the dot). A rotation by $2\pi/N$ therefore corresponds to a cyclic permutation

$$\exp\left\{\frac{2\pi i}{N} L_z^{\text{tot}}\right\} \Psi_N = (-1)^{N-1} \Psi_N, \quad (4.22)$$

where we have used that a cyclic permutation of an even (odd) number of electrons is odd (even). From Eq. (4.22), the allowed total angular momenta of the Wigner molecule can be easily read off: For an odd number of electrons the minimal angular momentum is zero, whereas it is nonzero and degenerate for an even electron number¹³, e.g. $M^{\text{tot}} = \pm 2$ for $N = 4$. Hence the UHF wave functions for $N = 2, 4, 7$ can be interpreted as standing waves, i.e. superpositions of opposite angular momentum states. For odd numbers of electrons in a spatial shell, there is no angular momentum degeneracy, and therefore no standing wave and no modulation in the densities. With a similar argument, HIROSE and WINGREEN (1999) explain the charge-density-waves which they found for *odd* number of electrons in the *weakly* interacting regime (open shell configurations) from density functional calculations. We will come back on this point for seven electrons in Sec. 4.3.6.

Equation (4.22) does not hold anymore when the spin is not polarized, because the total wave function is not a product of spin and orbital wave functions. However, within UHF we do not fix the exact spin but only subspaces with fixed S_z . For $S_z < N/2$ the UHF solution mainly renders the properties of the spin-polarized solution, as the energies and densities are essentially the same for $\lambda \gtrsim 6$. The even-odd effect is thus *not* a physical effect but an *artifact* of the UHF symmetry-breaking. Therefore great caution must be taken when interpreting the UHF densities. In particular, the exact onset of Wigner crystallization cannot be determined reliably from UHF calculations.

¹²In their study the interaction constant was $\lambda \approx 1.9$.

¹³In this fashion, RUAN ET AL. (1995) determine *magic numbers*, i.e. the fractional filling factors in the quantum Hall effect.

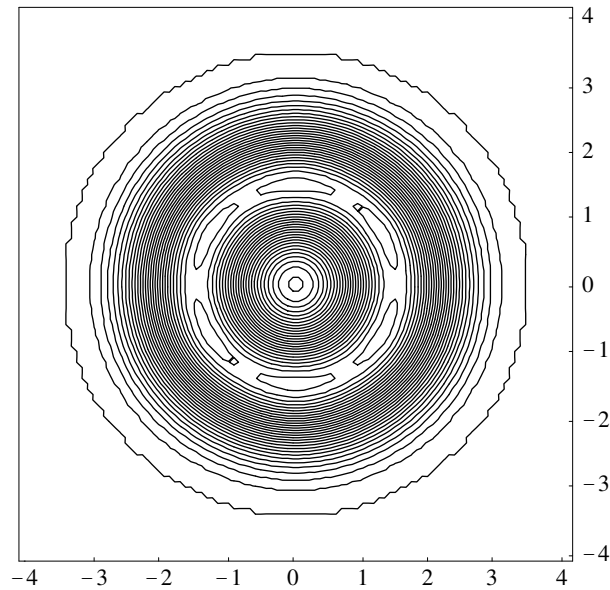


Fig. 4.11: UHF single-particle density n^{HF} for $N = 3$, $S_z = 3/2$ and $\lambda = 6$ as a contour plot with 30 contour lines.

4.3.3 Closer look at three electrons

For three electrons at strong interaction, we do not find the naively expected density with three maxima but a nearly round density. We want to study this further and show the case $N = 3$ of Fig. 4.10 once more with 30 contour lines in Fig. 4.11. A tiny sixfold modulation of the density is now discernible. This can be understood by going back to equation (4.22): After $M^{\text{tot}} = 0$ the next allowed total angular momentum values are $M^{\text{tot}} = \pm 3$, which give rise to a standing wave with six maxima. This becomes also clear from the densities of the single orbitals building the UHF single-particle density. In Fig. 4.12 we show the orbital densities for $\lambda = 4$ and $\lambda = 6$. We find a sixfold orbital, as well as two diametrically oriented threefold orbitals. One clearly recognizes how the sixfold density in Fig. 4.11 results from this. Note that the HF orbitals are not localized (for example at the angles of a triangle).

At this point we want to address a related issue, the uniqueness of the HF orbitals. One can easily show with the help of the HF equations (4.6) that HF orbitals with the same spin are no longer unique, if the corresponding one-particle energies ε_i are degenerate. In this case, any unitary transformation of degenerate orbitals also fulfills the HF equations. In Fig. 4.12, the respective energies ε_i are degenerate for the two states (b),(c) and (e),(f). Therefore these two orbitals are no longer uniquely determined, in addition to the orientational degeneracy of the total Slater determinant which is physically obvious.

Now, it is natural to presume that the degeneracies of the orbital energies are a

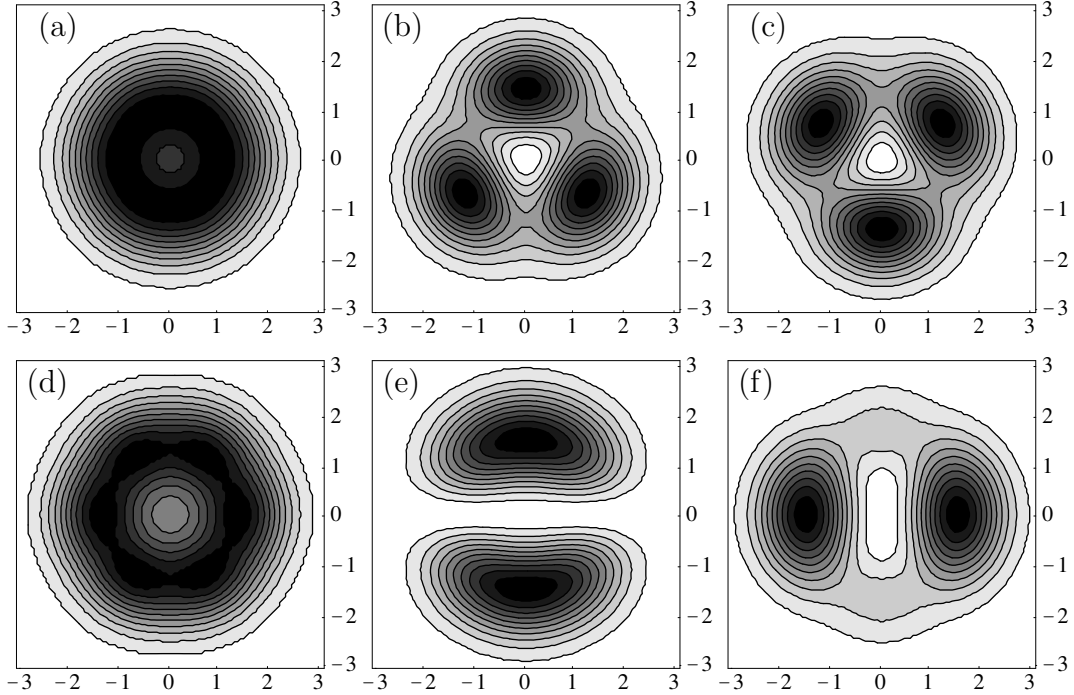


Fig. 4.12: UHF orbital densities $|\varphi_i|^2$ ($i = 1, 2, 3$) for $N = 3$ and $S_z = 3/2$. Upper row $\lambda = 4$, lower row $\lambda = 6$. For the single-particle energies we obtain (a) $\varepsilon_1 = 4.92$ and (b), (c) $\varepsilon_2 = \varepsilon_3 = 5.84$; (d) $\varepsilon_1 = 6.44$ and (e), (f) $\varepsilon_2 = \varepsilon_3 = 7.11$.

signature of Wigner crystallization, i.e. the geometry of the Wigner molecule. For strong interaction one should be able to represent the system as a lattice problem on an equilateral triangle. The corresponding Hamiltonian for $N = 3$, $S_z = 3/2$ then reads

$$H_3 = \begin{pmatrix} U & -t & -t \\ -t & U & -t \\ -t & -t & U \end{pmatrix}, \quad (4.23)$$

where U is the on-site energy and t is the tunneling matrix element between localized states. The eigenvalues of H_3 are in fact degenerate, $\varepsilon_1 = U - 2t$ and twice $\varepsilon_{2/3} = U + t$.

On the other hand, for $S_z = 1/2$ the tight-binding Hamiltonian involves tunneling only between the two spin up states and takes the form

$$H'_3 = \begin{pmatrix} U & -t & 0 \\ -t & U & 0 \\ 0 & 0 & U \end{pmatrix}. \quad (4.24)$$

The eigenvalues are $\varepsilon_{1/2} = U \pm t$ (spin up) and $\varepsilon_3 = U$ (spin down), with the same U , t as in Eq. (4.23). For instance, for $\lambda = 6$, we have $\varepsilon_1 = 6.65$, $\varepsilon_2 = 7.10$ and $\varepsilon_3 = 6.87$, which has to be compared with the orbital energies for the polarized state

given in Fig. 4.12 and yields $t \approx 0.22$. For higher λ the agreement still becomes better, e.g. for $\lambda = 12$ we find $\varepsilon_1 = 10.140$, $\varepsilon_2 = 10.309$ and $\varepsilon_3 = 10.224$ for $S_z = 1/2$, while $\varepsilon_1 = 10.06$ and $\varepsilon_{2/3} = 10.313$ for $S_z = 3/2$, which gives $t = 0.085$ in both cases.

4.3.4 Lattice Hamiltonian and localized orbitals

For large λ we find the same eigenvalues for a lattice Hamiltonian and the HF Hamiltonian. Thus, there must be a one-to-one correspondence between these two. Remember, however, that HF is a one-particle picture and thus the tight-binding Hamiltonian describes *one* particle hopping on a grid. The HF Hamiltonian is diagonal in the HF basis (4.2),

$$\langle i | h | j \rangle + \sum_k^N (ik | w | jk) = \varepsilon_i \delta_{ij} . \quad (4.25)$$

Now, if these eigenvalues coincide with those of a lattice Hamiltonian, e.g. H_3 in (4.23), this means that we have to transform the UHF orbitals with the inverse of the orthogonal transformation which diagonalizes the lattice Hamiltonian to pass over to localized orbitals. The Slater determinant (4.1) is not changed when we transform among occupied orbitals (EDMINDSTON and RUEDENBERG, 1963),

$$|p\rangle = \sum_i^N o_p^i |i\rangle . \quad (4.26)$$

In this new basis the HF equations read

$$\sum_q^N \{ \langle p | h | q \rangle + \sum_r^N (pr | w | qr) \} o_q^i = \varepsilon_i o_p^i . \quad (4.27)$$

Now, in the basis $|p\rangle$, we should have non-vanishing $\langle p | h | q \rangle$ only for nearest neighbors¹⁴, and the contribution of the two-particle matrix element should essentially be given by the direct term, i.e. diagonal elements of the Coulomb interaction. Then (4.27) reduces to

$$\sum_q^N \{ \langle p | h | q \rangle + \delta_{pq} \sum_r^N (pr | w | pr) \} o_q^i = \varepsilon_i o_p^i , \quad (4.28)$$

which is now of the form of a lattice Hamiltonian, we were looking for. According to EDMINDSTON and RUEDENBERG (1963), the transformation (4.26) leads to localized

¹⁴Note that in (4.26) we transform only among occupied orbitals with the same spin, $o_p^i \propto \delta_{\sigma_p \sigma_i}$ and thus $\langle p | h | q \rangle \propto \delta_{\sigma_p \sigma_q}$.

orbitals, which minimize the exchange energy. We do not perform this transformation explicitly, except in the case $N = 2$ in Sec. 4.2.4 and for $N = 4$ (see below), where we show that the tunneling matrix element for non-next neighbours really vanishes. For $N = 2$ we had seen that the orthogonal transformation leads us to orthogonal Hartree orbitals, i.e. to a vanishing exchange energy. However, the most important argument for this correspondence to localized orbitals is the near spin-independence of the HF energies, which is expected semiclassically. It was not obtained with RHF, which means that the RHF orbitals are not equivalent to localized orbitals.

We want to illustrate our strong numerical evidence for this connection between the UHF Hamiltonian and a lattice Hamiltonian for $N = 4$ and 5 which are the simplest cases of electrons on a ring. For $N = 4$, $S_z = 2$ we have

$$H_4 = \begin{pmatrix} U & -t & 0 & -t \\ -t & U & -t & 0 \\ 0 & -t & U & -t \\ -t & 0 & -t & U \end{pmatrix}, \quad (4.29)$$

with the eigenvalues $\varepsilon_1 = U - 2t$, $\varepsilon_{2/3} = U$ and $\varepsilon_4 = U + 2t$. The eigenvectors of H_4 determine the transformation (4.26). Applying this transformation to the HF Hamiltonian, as we did in (4.17), we obtain for $\lambda = 8$ an Hamiltonian of the form (4.29) with $U = 10.924$ and $t = 0.195$. The next-nearest-neighbor hopping matrix element (hopping along the diagonal of the square) is $t^* = 2\varepsilon_2 - \varepsilon_1 - \varepsilon_4 = 0.003$, which is indeed already very small.

Likewise we can determine the lattice Hamiltonians for other electron numbers and spin configurations and we have collected results for t and U for stronger interaction up to $\lambda = 20$. For $N = 4$, $S_z = 1$ the lattice Hamiltonian reads

$$H'_4 = \begin{pmatrix} U & -t & 0 & 0 \\ -t & U & -t & 0 \\ 0 & -t & U & 0 \\ 0 & 0 & 0 & U \end{pmatrix}, \quad (4.30)$$

with the eigenvalues $\varepsilon_1 = U - \sqrt{2}t$, $\varepsilon_2 = U$ and $\varepsilon_3 = U + \sqrt{2}t$ (spin up) and $\varepsilon_4 = U$ (spin down), while for $N = 4$, $S_z = 0$ we have

$$H''_4 = \begin{pmatrix} U & -t & 0 & 0 \\ -t & U & 0 & 0 \\ 0 & 0 & U & -t \\ 0 & 0 & -t & U \end{pmatrix}, \quad (4.31)$$

with $\varepsilon_{1/2} = U \pm t$ (spin up), $\varepsilon_{3/4} = U \pm t$ (spin down). Here, we have to assume that the four states are occupied with two pairs of nearest-neighbor parallel spins in order to obtain agreement with the UHF orbital energies. The values of t we obtain in this way for the three spins states $S_z = 0, 1, 2$ agree within 1% for $\lambda = 8$.

For $N = 5$, we have a pentagon and again three different spin states. For $S_z = 5/2$, the lattice Hamiltonian with nearest-neighbor hopping is

$$H_5 = \begin{pmatrix} U & -t & 0 & 0 & -t \\ -t & U & -t & 0 & 0 \\ 0 & -t & U & -t & 0 \\ 0 & 0 & -t & U & -t \\ -t & 0 & 0 & -t & U \end{pmatrix}, \quad (4.32)$$

with the eigenvalues $\varepsilon_1 = U - 2t$, $\varepsilon_{2/3} = U + t/2(1 - \sqrt{5})$ and $\varepsilon_{4/5} = U + t/2(1 + \sqrt{5})$, while for $S_z = 3/2$ we have

$$H'_5 = \begin{pmatrix} U & -t & 0 & 0 & 0 \\ -t & U & -t & 0 & 0 \\ 0 & -t & U & -t & 0 \\ 0 & 0 & -t & U & 0 \\ 0 & 0 & 0 & 0 & U \end{pmatrix}, \quad (4.33)$$

with $\varepsilon_{1/2} = U - t/2(\sqrt{5} \pm 1)$, $\varepsilon_{3/4} = U + t/2(\sqrt{5} \mp 1)$ (spin up) and $\varepsilon_5 = U$ (spin down). Finally for $S_z = 1/2$ we have

$$H''_5 = \begin{pmatrix} U & 0 & 0 & 0 & 0 \\ 0 & U & -t & 0 & 0 \\ 0 & -t & U & 0 & 0 \\ 0 & 0 & 0 & U & 0 \\ 0 & 0 & 0 & 0 & U \end{pmatrix}, \quad (4.34)$$

with the eigenvalues $\varepsilon_{1/3} = U \pm t$, $\varepsilon_2 = U$ (spin up) and $\varepsilon_{4/5} = U$ (spin down). Note that here the values of the UHF orbital energies suggest a model with only two nearest-neighbor parallel spins. For $\lambda = 6$ the values of t for all three spin states coincide within 1%.

Figure 4.13 summarizes our findings about the tunnel matrix elements. HÄUSLER (2000) predicted $t \propto \exp(-\sqrt{r_s})$, where r_s is the nearest-neighbor distance of the electrons measured in units of the effective Bohr radius. Since classically $r_s \propto \lambda^{4/3}$ (cf. Sec. 2.8), we plot $\ln t$ against $\lambda^{2/3}$. For $\lambda \gtrsim 8$ we find indeed a linear behavior. For lower λ , the tunneling matrix element is not really defined, since the lattice model is not appropriate. The tunneling matrix element is largest for $N = 2$ because two electrons are always closest (see Table Sec. 2.1). Three electrons always have the smallest value of t because the corresponding equilateral triangle has a longer side than the square and the pentagon. For higher electron numbers one electron enters the center of the dot, and the UHF spectra are more complicated though they still show the typical degeneracy. However, now the lattice Hamiltonian has various tunneling constants and on-site energies, which we cannot determine without further assumptions.

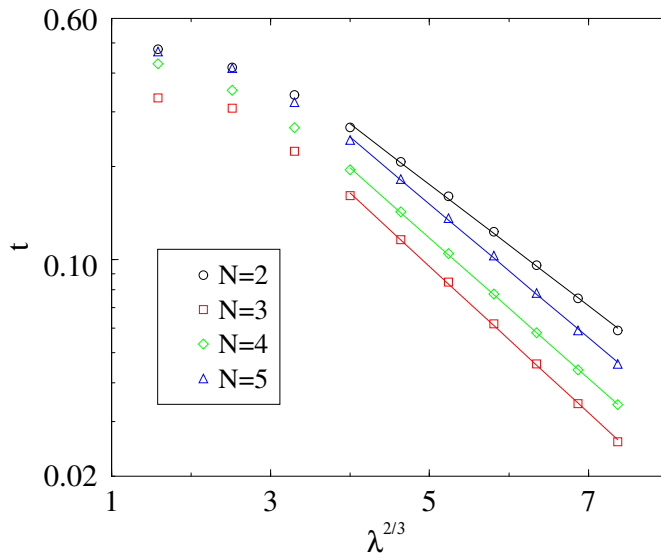


Fig. 4.13: Log-linear plot of tunnel matrix element t vs. $\lambda^{2/3}$ for various electron numbers. For $\lambda \geq 8$, the line of best fit is shown.

4.3.5 Geometric crossover for six electrons

In Fig. 4.14 we show how Wigner crystallization is mirrored by the UHF densities in the case $N = 6$ and $S_z = 0$. This unpolarized case is interesting because it depicts a crossover in the geometry from an equilateral hexagon to a pentagon with a central electron. Classically the pentagon is the most stable configuration for all λ (see Sec. 2.8). For weak interaction, six electrons are just the closure of the second shell. The six-electron molecule was also studied by REIMANN ET AL. (2000), who found by means of configuration-interaction calculations that the true ground-state is unpolarized with a sixfold symmetry up to at least $\lambda \approx 3.5$ (cf. Sec. 3.4.2). They stated by comparing with YANNOULEAS and LANDMAN (1999) that the crystallization occurs too early in the UHF approximation. We confirm this conclusion and find that within UHF the $S_z = 0$ state acquires a fivefold symmetry for $\lambda \geq 2.85$. For larger λ the UHF density is distorted [$\lambda = 4$ in Fig. 4.14(c)] and then apparently round for higher λ with a central maximum [$\lambda = 6$ in Fig. 4.14(d)]. Figure 4.14(b) shows the sixfold isomer for $\lambda = 4$, which is by 0.33 higher in energy¹⁵. Within UHF the $S_z = 0$ state is the ground state for weak interaction while one finds a spin-polarized ground state for $\lambda \geq 2.5$. On the other hand, for $N = 6$ and $\lambda = 8$, QMC gives a $S = 1$ ground state. The UHF spin-polarized state exhibits fivefold symmetry throughout the whole parameter range. In general, the polarized states

¹⁵Also the sixfold electron molecule shown in Fig. 2(c) of YANNOULEAS and LANDMAN (1999) for $\lambda = 3.2$ is an excited state. We are not able to reproduce the spin density in Fig. 2(a) of the same work.

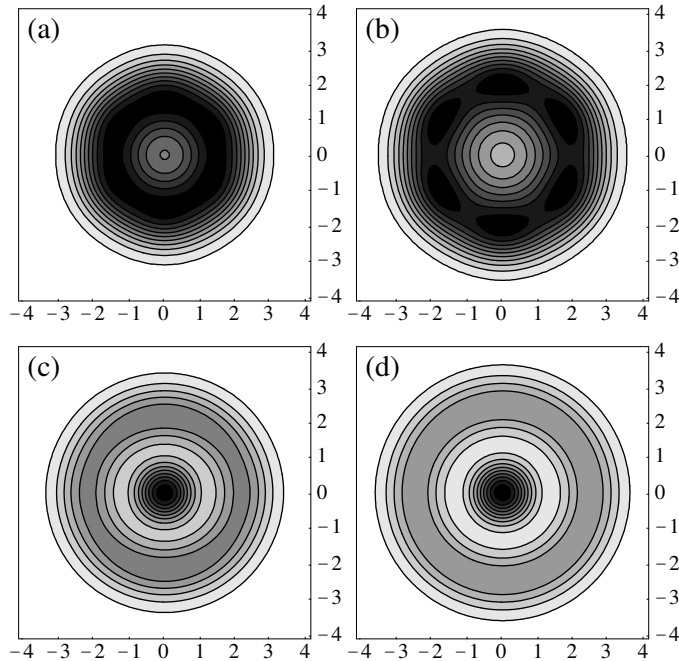


Fig. 4.14: UHF one-particle densities for $N = 6$ and $S_z = 0$. Rearrangement from a sixfold [(a) $\lambda = 2$] to a (deformed) fivefold geometry [(c) $\lambda = 4$ with energy $E = 41.509$, (d) $\lambda = 6$]. In (b), sixfold isomer at $\lambda = 4$ with energy $E^* = 41.838$.

show most clearly the classical crystalline filling, which can be understood because of the stronger correlation of electrons with parallel spins due to the Pauli principle.

4.3.6 Seven- and eight-electron Wigner molecules

Here we want to present the Wigner crystallization for a larger Wigner molecule, as shown by the UHF densities. Seven classical electrons form an equilateral hexagon with one central electron, which is a fragment of a hexagonal lattice. In Fig. 4.15 we start with a small λ , that is the quantum-mechanical limit of high density. The UHF ground state is $S_z = 1/2$ up to $\lambda \lesssim 3$, then spin-polarized. In Fig. 4.15(a) for $\lambda = 1$ we see a fourfold modulated density. How is that possible for seven electrons? The answer is that in this case the energy shell picture of the harmonic oscillator is still valid: Six electrons are just a shell closure and the next electron is put in the new shell in an orbital with maximal angular momentum (cf. Sec. 2.4). This angular momentum is $M = \pm 2$ and from the superposition one obtains a fourfold standing wave. Here the energy is basically the same as in RHF, but the Slater determinant breaks the symmetry. The same phenomenon can be found for weak interaction and $N = 3$ or 5 , which are also open-shell configurations. In this fashion, HIROSE and WINGREEN (1999) explain the deformed densities (*charge-density-waves*) in their

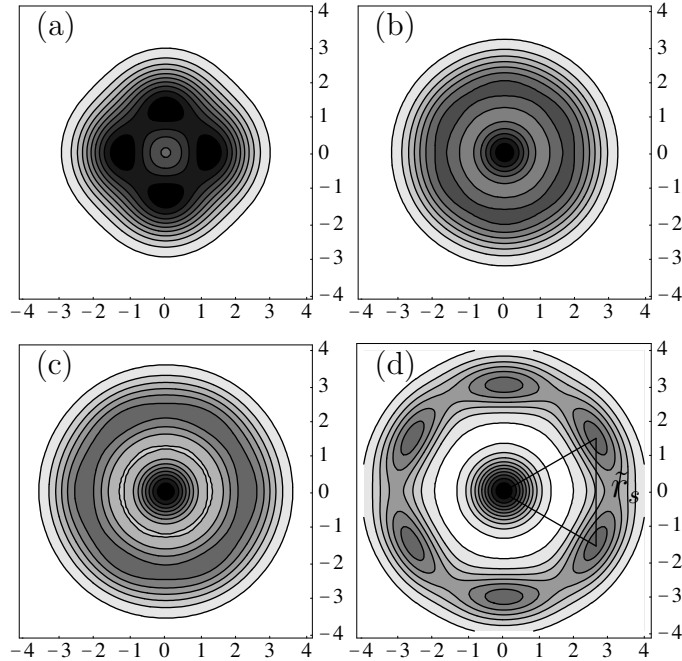


Fig. 4.15: One-particle densities for the UHF ground state of $N = 7$ electrons. (a) $\lambda = 1$, (b) $\lambda = 2$, both $S_z = 1/2$. (c) $\lambda = 4$, (d) $\lambda = 10$, both $S_z = 7/2$.

density-functional study with coupling constant $\lambda = 1.91$.

We want to emphasize that for high λ the UHF densities mirror the classical shell filling. This can even be quantified: The positions of the maxima (even in the 'round' densities) agree very well with the classical configurations in Sec. 2.8. From the UHF density the nearest-neighbor distance \tilde{r}_s can be determined. For example from Fig. 4.15(d) we find $\tilde{r}_s \approx 3.0$, which is also the classical value. Here we have to take into account that we measure length in oscillator units. Frequently, one is interested in the density parameter r_s given in effective Bohr radii. Then Fig. 4.15(d) gives $r_s = \tilde{r}_s l_0 / a_B^* = \lambda \tilde{r}_s \approx 30$. The r_s values we obtain in this way agree also well with the results of PIMC.

Finally, for $N = 8$ we want to confront the HF densities with the exact PIMC data. The UHF densities for eight spin-polarized electrons are nearly azimuthally symmetric and thus suggest a (1, 7) spatial shell filling, which is also expected classically (see Sec. 2.8). We therefore can naively compare radial charge densities for symmetry breaking UHF and symmetry preserving RHF and PIMC. This is shown for two different interaction strengths in Fig. 4.16. For $\lambda = 2$ UHF and RHF nearly coincide and agree rather well with the PIMC except for the small shoulder in the HF densities. For $\lambda = 8$ the radial ordering is clearly exaggerated by HF. Surprisingly UHF fits much worse to the exact data than RHF, which renders the outer peak and

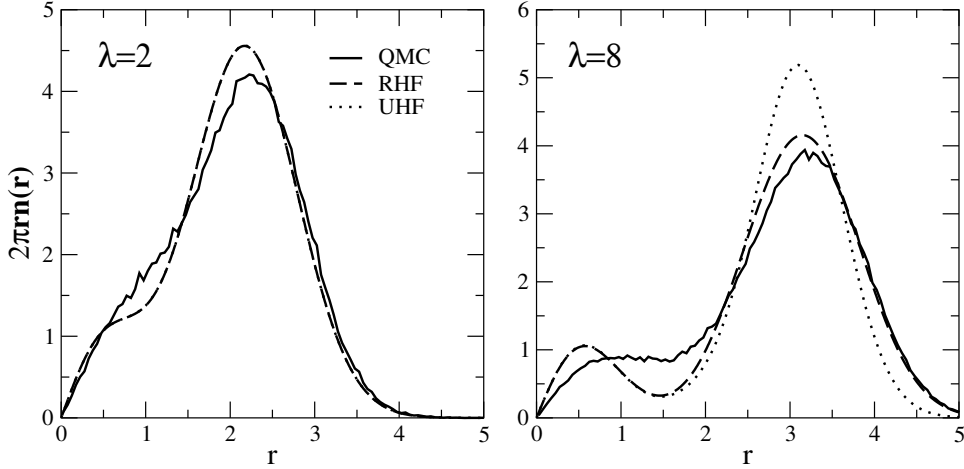


Fig. 4.16: Radial charge densities for $N = 8$ spin-polarized electrons and $\lambda = 2, 8$ as shown by RHF, UHF, and QMC.

the decay correctly. We therefore conclude that for an adequate comparison of UHF and exact densities one has to carry out the restoration of symmetry as mentioned in Sec. 4.2.5. This proceeding should give a much better agreement.

4.4 Unrestricted Hartree-Fock with a magnetic field

In this section we want to present some calculations with a magnetic field orthogonal to the plane of the quantum dot. This system has been discussed extensively in the literature, especially in connection with the quantum Hall effect. UHF calculations by MÜLLER and KOONIN (1996) have shown a *magnetic field induced Wigner crystallization*. However, they only considered the limiting case of a strong magnetic field and therefore included in the basis for expanding the UHF orbitals only states from the lowest Landau level (Fock-Darwin levels with $n = 0$). To study smaller magnetic fields, our basis is better adjusted to the problem. It is intuitively clear, that electrons are further localized by the magnetic field. Indeed we do not find an even-odd effect for UHF densities but molecule-like densities for all electron numbers.

4.4.1 Quantum dot energies with magnetic field

In Sec. 2.3 the Hamiltonian of the clean quantum dot with magnetic field was given in Eq. (2.6). It depends on the dimensionless cyclotron frequency $H = H(\Omega_c)$ and has the property

$$H(\Omega'_c) = H(\Omega_c) + \frac{1}{2}(\Omega_c - \Omega'_c)L_z^{\text{tot}}. \quad (4.35)$$

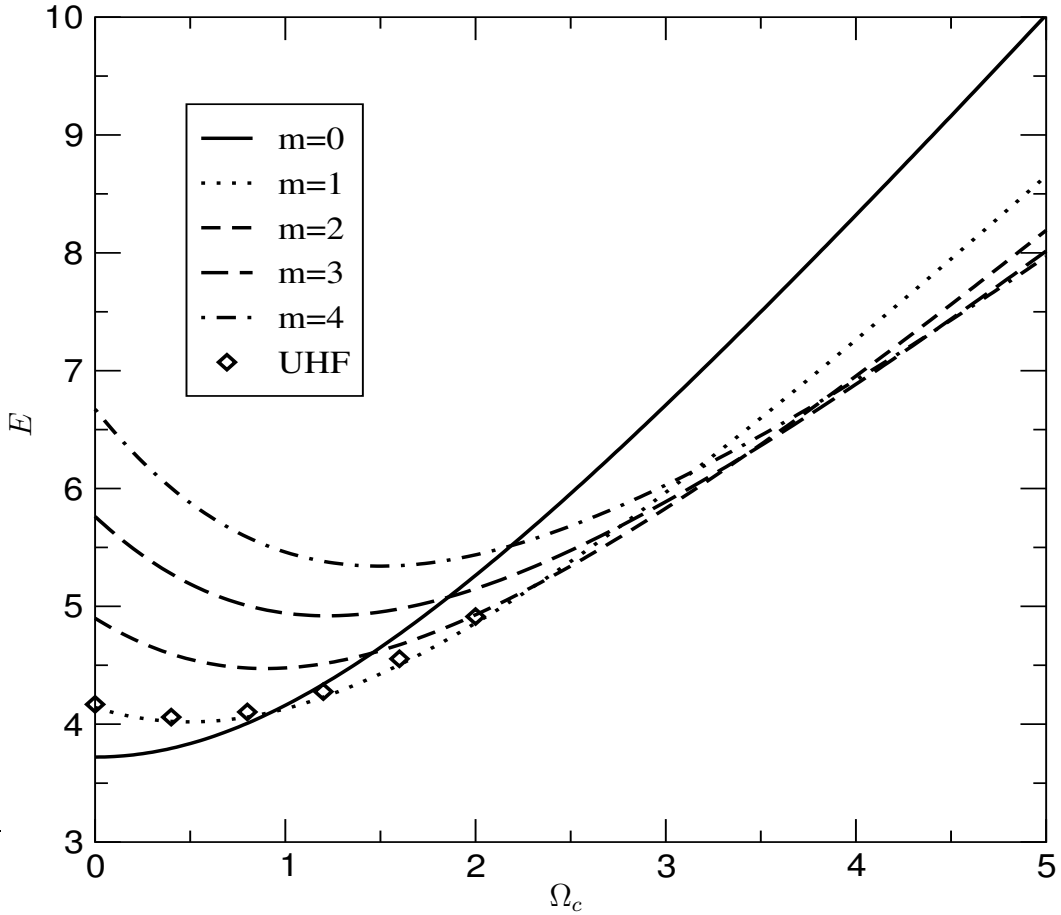


Fig. 4.17: Exact ground-state energies in units of $\hbar\omega_0$ for two electrons and $\lambda = 2$ vs. the cyclotron frequency Ω_c . The ground state is singlet or triplet, depending on whether the relative angular momentum is even or odd. Also shown UHF energies for $S = 1$.

This means that if we know the entire spectrum of H for one magnetic field, then we know the spectrum of H for any magnetic field. The eigenfunctions, which are also eigenfunctions of the total angular momentum, do not change. We want to take advantage of this property: In Fig. 4.17 we show the evolution of the ground state of two electrons with increasing magnetic field strength. For this we have used the spectrum of the exact diagonalization for $\Omega_c = 0$ (Sec. 3.2.1) and Eq. (4.35). With increasing magnetic field the ground state acquires higher and higher angular momentum. These crossings are accompanied by a change from singlet to triplet, depending on whether the relative angular momentum is even or odd. Singlet-triplet transitions have been identified in the experiment as cusps in the addition energies (ASHOORI ET AL., 1993; KOUWENHOVEN ET AL., 2001)¹⁶.

¹⁶ Recently, KYRIAKIDIS ET AL. (2002) have shown for a lateral dot that these transitions can also be engineered by deforming the external confinement potential at fixed magnetic field.

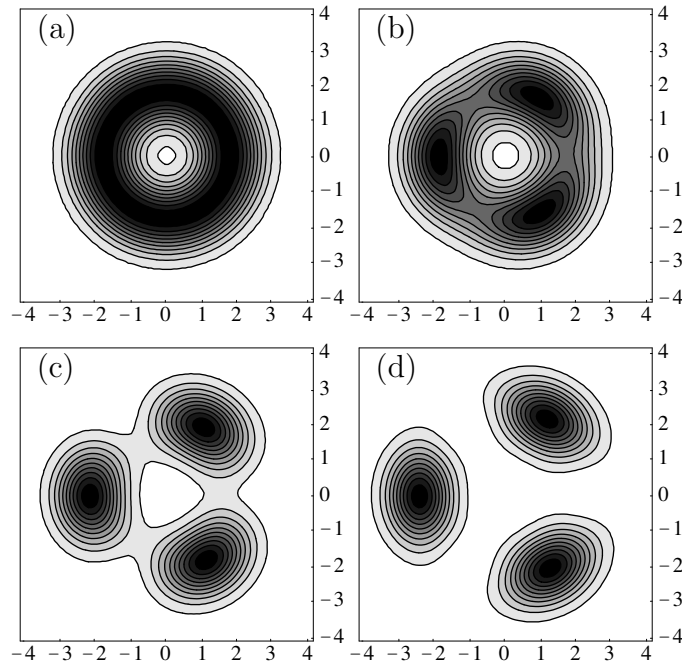


Fig. 4.18: Evolution of the UHF one-particle densities for $N = 3$, $S_z = 3/2$ and $\lambda = 10$ with increasing magnetic field strength $\tilde{\omega}_c = \omega_c/\omega_0$. (a) $\tilde{\omega}_c = 0$, (b) $\tilde{\omega}_c = 0.5$, (c) $\tilde{\omega}_c = 1.5$, (d) $\tilde{\omega}_c = 2.5$.

The property (4.35) does not help us for higher electron number, because we do not know the entire spectrum. With HF or QMC we only obtain a ground state¹⁷. The evolution of this state can be followed for a small range of magnetic fields, as we will show below.

Numerically, thanks to the similar form of the Hamiltonian (2.6) to the one without magnetic field, the generalization of our UHF code is straightforward. All we need are the matrix elements of the angular momentum, and we are already working in the angular momentum basis. However the magnetic field breaks time-reversal symmetry, and left and right turning solutions are no longer energetically degenerate. Therefore, in the expansion of the UHF orbitals (4.2), we have to use complex coefficients.

4.4.2 UHF densities with magnetic field

In this section we show the UHF one-particle densities with magnetic field. At higher magnetic field there is *no* even-odd effect and the densities are molecule-like for all electron numbers.

¹⁷For UHF we normally do not even have an eigenstate of angular momentum. Anyway, if we have good total angular momentum, (4.35) holds also for the HF Hamiltonian.

We first consider three electrons and a large interaction parameter $\lambda = 10$. This means that we have a shallow quantum dot where the Coulomb interaction dominates and the magnetic field is relatively weak [see footnote to Eq. (2.7)]. In Fig. 4.18 we display the evolution of the UHF one-particle densities with increasing magnetic field strength $\tilde{\omega}_c = \omega_c/\omega$ at fixed λ . This is not exactly the physical situation, corresponding to a quantum dot exposed to an increasing magnetic field, since the coupling constant λ becomes smaller with increasing field. Here we just want to show that a magnetic field does not have the same effect on the UHF density as a strong interaction.

In Fig. 4.18(d) we see three distinct, localized electrons in the UHF density. The three single orbital densities have nearly the same form. Thus, the orbitals are not localized, they are similar to the orbitals *chosen* by SZAFRAN ET AL. (2003) appositely for strong magnetic field. With *decreasing* magnetic field strength the maxima in azimuthal direction vanish slowly, until we have again a nearly round density for $\omega_c = 0$ as in Fig. 4.10. The density in Fig. 4.18(a) has been obtained from an initial guess with threefold symmetry. Therefore we can be sure that we have not obtained a local minimum but the true UHF ground state.

As a second example we show the evolution of the UHF density of six electrons at intermediate coupling strength¹⁸ $\lambda = 3.2$. Without magnetic field the density is round, Fig. 4.19(a), and with a weak magnetic field fivefold with a central electron, Figs. 4.19(b),(c).

Here we find an additional interesting phenomenon: For intermediate magnetic field $\tilde{\omega}_c \approx 1 \dots 1.5$, the UHF ground state has a perfectly round density, Fig. 4.19(d), and also a rotationally symmetric Slater determinant. This is the so-called maximum-density-droplet of MACDONALD ET AL. (1993), where the electrons occupy the lowest orbitals with increasing angular momentum. Here the orbitals with $M = 0 \dots 5$ are occupied, and the UHF solution is identical to the RHF solution with total angular momentum $M^{\text{tot}} = 15$. In this magnetic field range, the Slater determinant stays always the same and the HF energy evolves as given by Eq. (4.35).

Finally, in Fig. 4.19(e) for strong magnetic field we have a distinctly localized fivefold Wigner molecule. Figure 4.19(f) for $\tilde{\omega}_c = 2.5$ shows a sixfold isomer which is higher in energy by 0.009 than the fivefold ground state.

4.4.3 Relation to other results

We briefly want to comment on the discrepancies to YANNOULEAS and LANDMAN (1999, 2000b, 2002). We have found densities that differ from theirs (e.g. they do not find the even-odd effect and they find different conditional probability densities), this

¹⁸This corresponds to the value used by YANNOULEAS and LANDMAN (1999) to obtain the densities in Fig. 2(c) that supposedly were calculated without magnetic field but resemble our densities with field.

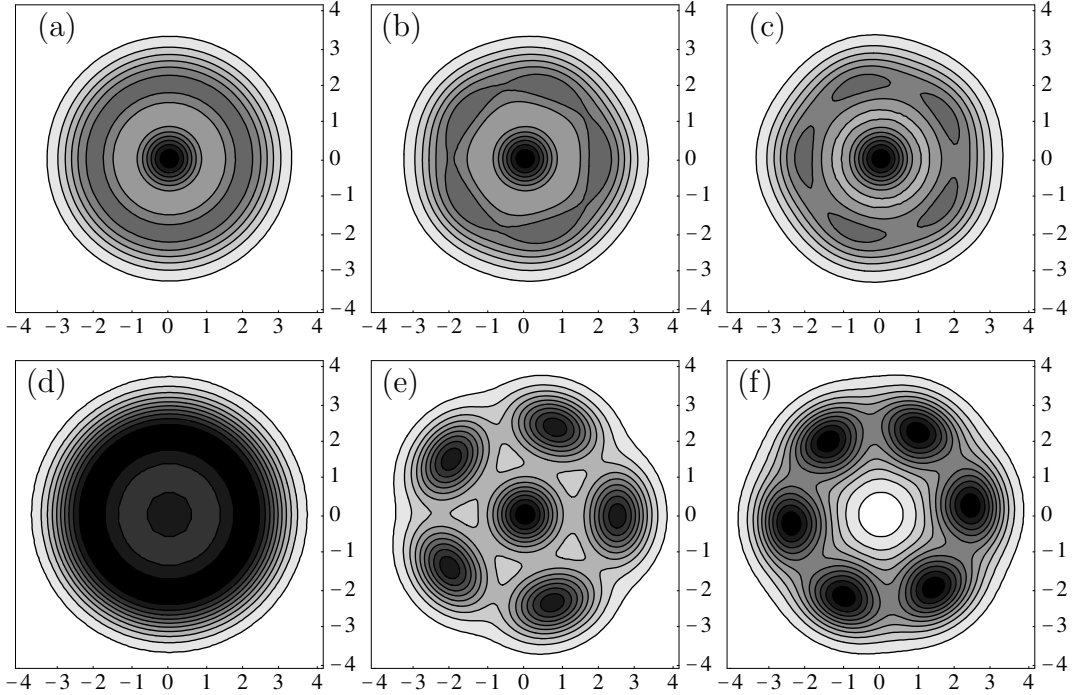


Fig. 4.19: Evolution of the UHF one-particle density for $N = 6$, $S_z = 3$ and $\lambda = 3.2$ with increasing magnetic field strength, (a) $\tilde{\omega}_c = 0$, (b) $\tilde{\omega}_c = 0.1$, (c) $\tilde{\omega}_c = 0.5$, (d) $\tilde{\omega}_c = 1$, (e) $\tilde{\omega}_c = 2$, (f) $\tilde{\omega}_c = 2.5$. In (f) sixfold isomer with energy $E_{\text{HF}}^* = 45.182$.

means that we have found different Slater determinants. This is mysterious because UHF is supposed to be a well-defined approximation. As a starting point to understand this it would have been interesting to compare our energies. Unfortunately, in their papers they give only very few explicit numerical values for the energy, e.g. they give two values for the RHF and UHF energies of quantum-dot Helium which we can reproduce. They did not comment on our UHF energies tabulated in REUSCH ET AL. (2001) and did not send us their numerical results when we courteously asked them to. A solution to this mystery could be that they use a-priori chosen orbitals (see also SZAFRAN ET AL., 2003; SUNDQVIST ET AL., 2002) and thus perform rather a variational approach (so-called variational HF) than the true self-consistent HF method. In certain regimes (strong interaction, high magnetic field) this variational method should lead to the same energy although coming from different Slater determinants. If they really self-consistently solved the UHF equations this would mean that there might be an ambiguity for the UHF solution¹⁹. However, we can only

¹⁹Similar to CSHF and RHF (or RHF and UHF) solutions which are different Slater determinants but give the same energies for (very) small interaction (cf. Secs. 4.2.2, 4.3.6). In this sense, HF is unambiguous only when exactly the same symmetries are preserved. Seemingly, our UHF

speculate but have no real hint that the UHF Slater determinant is not unique in the strong interaction limit apart from the orientational degeneracy, which is physically obvious.

4.5 Conclusion

In conclusion, we have discussed the properties of unrestricted Hartree-Fock (UHF) calculations for electrons in a quantum dot, focussing on the crossover to strong correlations, when electrons begin to form a Wigner molecule. The UHF energies are good estimates of the true ground-state energies, especially for the polarized states, even at strong interaction. However, the energy differences between different spin states cannot be resolved correctly, the polarized state is unphysically favored for stronger interaction. The UHF energies become nearly spin-independent in this regime, faster than it is the case for the true energies. UHF also fails to give correct addition energies for $\lambda \gtrsim 2$.

Regarding the interpretation of other quantities obtained from the UHF Slater determinant, we have shown that considerable caution must be taken: We find deformed densities in the regime of intermediate interaction $\lambda \approx 1 \dots 4$. For stronger interaction, the densities are azimuthally modulated for an even number of electrons per spatial shell, and round for an odd number per shell. The onset of this modulation is enhanced within UHF, so that UHF leads to an overestimation for the value of the critical density for the crossover to the Wigner molecule. This explains the discrepancies between YANNOULEAS and LANDMAN (1999) based on UHF and the exact QMC results of EGGER ET AL. (1999). We want to emphasize that the even-odd effect we found for the densities is an artifact of the symmetry-breaking of UHF and arises from a degeneracy of states with opposite total angular momentum.

For very strong interaction, we have shown that the UHF Hamiltonian corresponds to a tight-binding model of a particle hopping between the sites of the Wigner molecule. From the UHF orbital energies we have obtained the hopping matrix elements and on-site energies. This explains why the UHF energies become spin-independent, while this is not the case for restricted Hartree-Fock (RHF). The maxima of the UHF densities mirror the classical filling scheme with the electrons arranged in spatial shells. One has to pay attention to avoid isomers with slightly higher energy, that are local minima for the HF iteration. In contrast, the UHF two-particle density (conditional probability density) has no direct physical meaning, because the UHF method cannot take correlations properly into account. Finally, in a strong magnetic field, the UHF densities are always molecule-like and there is no even-odd effect.

solutions without magnetic field preserve time reversal symmetry (see Sec. 4.2.4). For some exact properties of HF theory, see references in BACH ET AL. (1994).

5 Conclusions

We have investigated correlations in few-electron quantum dots. We considered a model of interacting two-dimensional electrons confined by a harmonic isotropic potential. In these systems one can tune the electron-electron interaction. In the weakly interacting limit a one-particle description is valid, where electrons are accommodated in orbitals. This results in an energetic shell filling. In the other limit of very strong interaction the system behaves almost like classical electrons which form a small crystal, the Wigner molecule. In this work we focused on the crossover between these two limits. This intermediate regime is difficult to address numerically, it is yet the most interesting and least understood. We performed calculations by means of two methods: path-integral Monte Carlo (PIMC) simulations and unrestricted Hartree-Fock (UHF).

In the first part of this thesis we have given an introduction to the field of few-electron quantum dots and sketched the experiments which inspired our calculations. Atomlike properties with Hund's rule shell filling have been found for very small quantum dots. Experiments on larger and more disordered dots probed the localization-delocalization transition, i.e. the onset of Wigner crystallization. In this regime, bunching was observed, which means vanishing addition energies for special electron numbers.

In the second part we have presented a comprehensive PIMC simulation. This method is computationally very demanding but numerically exact and best adapted to study the whole range of interaction strengths. In this calculation we also included a single attractive impurity which breaks the symmetry of the isotropic two-dimensional oscillator potential. We have shown that by the Trotter extrapolation procedure we can obtain high-accuracy results which have benchmark character. The main difficulty is of course the fermion sign problem. Due to it, we had to restrict our calculations to $N \leq 10$ electrons. In turn, we were working at a very low temperature, so the spin contamination problem is very small and we are sure that we calculate essentially ground-state energies.

For the incipient Wigner molecule regime with a Brueckner parameter $r_s \approx 4$ ($\lambda = 4$), we made several exciting predictions. Despite of the rather strong interaction we still found remnants of the shell structure of weakly interacting dots (artificial atoms) in the addition energies. With impurity, the addition spectrum is profoundly altered. The cusps at the magic numbers of the clean dot disappear. Instead we found a new peak and a new ground-state spin for eight electrons. The sub-Hund's rule spin $S = 0$ at $N = 8$ is very unexpected because interactions normally drive the

system towards spin polarization. In this case (and less pronounced for $N = 3$) the defect depolarizes the ground state whereas for other electron numbers the spin gap is diminished and the ground-state spin is unchanged. We did not find the bunching phenomenon in our calculations. Maybe one has to include stronger disorder or other features not contained in our model or consider higher electron numbers to reproduce it numerically. The onset of Wigner crystallization is mirrored in the charge densities and this process is clearly amplified by the impurity. In the meantime, the spin order does not yet follow the charge order. Interestingly, this effect is also enhanced by the defect, which is probably due to the formation of a local momentum at the impurity. For six electrons we have shown quantitatively that the Wigner crystallization process is spin dependent, and that once again this dependency is reinforced by the impurity. We also considered the impurity's susceptibility as a function of temperature. Its behavior is indeed reminiscent of the Kondo effect. Altogether it is surprising that a single rather weak impurity leads to large effects. This is due to the breaking of rotational symmetry.

Finally, in the third part we performed unrestricted Hartree-Fock (UHF) calculations for rotationally symmetric clean quantum dots. This mean-field method is computationally less demanding, so it can be regarded as complementary to the PIMC simulations. However, we have shown that considerable caution has to be taken, when interpreting the results of UHF. The absolute values of the UHF energies are rather reliable estimates for the true ground-state energies. On the other hand, the method cannot resolve correctly the tiny energy differences which determine spin ordering and addition energies. For example, the energetic shell structure of the addition energies disappears too early within UHF when the interaction strength is increased. We found an even-odd artifact for the symmetry-breaking UHF densities. For an even number of electrons per spatial shell the densities are azimuthally modulated. This happens already for a very small interaction strength and might lead to underestimate the critical r_s parameter for the onset of Wigner crystallization. Conversely, for odd electron numbers the UHF densities are fairly round and thus mirror the Wigner crystallization only indirectly. We explained that the even-odd effect is determined by the ground-state angular momentum of the Wigner molecule. Furthermore, we have shown the equivalence of the UHF Hamiltonian to a tight-binding model for very strong interaction. Finally, with a small magnetic field, there is no even-odd effect. This indicates a different mechanism for the UHF symmetry breaking than in the strongly interacting case.

Quantum dots are and continue to be a fast-growing area of study in condensed-matter physics. While there is only a small number of experiments on few-electron quantum dots worldwide, many theoretical groups are investigating parabolic quantum dots (or similar models) with various methods. This makes it possible to compare with other results, often even quantitatively; this concurrence is very stimulating. In this sense, regarding the methods, our purpose was twofold. On the one hand, we have reconsidered the Hartree-Fock method. Its unrestricted version is the most

general form of the one-particle concept. By means of symmetry breaking it can incorporate correlations to some extent. However it remains an approximation and we have analyzed its properties and limitations for the full range of coupling constants. On the other hand, path-integral Monte Carlo is a state-of-the-art method, probably the only one which can give exact results in the crossover regime and for very strong interaction and higher electron number. In our simulation we focused on the regime of beginning Wigner crystallization, which has been reached recently in experiments. We have given numerical benchmark results in this regime and in the presence of a defect which deforms the ideal rotationally symmetric confinement.

Summarizing, we wanted to improve our understanding of the formation of Wigner molecules in few-electron quantum dots. This process can be regarded as a crossover from the quantum to the classical world. Coming from the classical limit it can also be viewed as (a finite-size analogue of) a quantum phase transition where fluctuations at zero temperature destroy the crystallized ordered state. Though we are dealing with a very small system, this transition appears to be a relatively sharp crossover. By studying Wigner crystallization in detail, we have gained much insight into how quantum effects interplay with Coulomb interactions in a few-particle confined system. The *symmetry* of the external confinement has a predominant effect on the electronic structure. *Correlations* strongly influence the energetic spectra, the stability and the charge ordering in real space. *Spin* has an important role in the crystallization process, and, conversely, interaction and confinement determine the ground-state spin in a nontrivial way. All together these ingredients add up to a fascinating mosaic which continues to be a challenging field for the physicist.

Parts of this work have been presented on the following conferences and workshops:

- 22nd International Conference on Low Temperature Physics, poster, see HÄUSLER ET AL. (2000), Espoo and Helsinki, Finland, August 1999
- Frühjahrstagung der Deutschen Physikalischen Gesellschaft, poster, Regensburg March 2000
- Arbeitsgruppenseminar Prof. Dr. U. Rössler, talk, Regensburg 18.07.2000
- Frühjahrstagung der Deutschen Physikalischen Gesellschaft, poster, Hamburg March 2001
- CECAM tutorial on *Quantum Monte Carlo*, talk, Lyon, France October 2001
- NIC Winter School on *Quantum simulation of Complex Many-Body Systems*, poster, Kerkrade, Netherlands February 2003

Bibliography

- ABRAHAMS, E., S. V. KRAVCHENKO and M. P. SARACHIK. *Metallic behavior and related phenomena in two dimensions*. Rev. Mod. Phys. **71**, 251, 2001.
- ALHASSID, Y. *The statistical theory of quantum dots*. Rev. Mod. Phys. **72**, 895, 2000.
- ASHOORI, R. C. *Electrons in artificial atoms*. Nature **379**, 413, 1996.
- ASHOORI, R. C., H. L. STORMER, J. S. WEINER, L. N. PFEIFFER, K. W. BALDWIN and K. W. WEST. *N-Electron Ground State Energies of a Quantum Dot in a Magnetic Field*. Phys. Rev. Lett. **71**, 613, 1993.
- ASHOORI, R. C., H. L. STORMER, J. S. WEINER, L. N. PFEIFFER, S. J. PEARTON, K. W. BALDWIN and K. W. WEST. *Single-Electron Capacitance Spectroscopy of Discrete Quantum Levels*. Phys. Rev. Lett. **68**, 3088, 1992.
- ASHOORI, R. C., N. B. ZHITENEV, L. PFEIFFER and K. WEST. *Paired additions of electrons into quantum dots: How and why does localization destroy Coulomb blockade to induce pairing?*. Physica E **3**, 15, 1998.
- BACH, V., E. H. LIEB, M. LOSS and J. P. SOLOVEJ. *There are no unfilled shells in Hartree-Fock theory*. Phys. Rev. Lett. **72**, 2981, 1994.
- BEDANOV, V. M. and F. M. PEETERS. *Ordering and phase transition of charged particles in a classical finite two-dimensional System*. Phys. Rev. B **49**, 2667, 1994.
- BEDNAREK, S., B. SZAFRAN and J. ADAMOWSKI. *Solution of the Poisson-Schrödinger problem for a single-electron transistor*. Phys. Rev. B **61**, 4461, 2000.
- BENENTI, G., G. CALDARA and D. L. SHEPELYANSKY. *Spin-Polarized Ground State for Interacting Electrons in Two Dimensions*. Phys. Rev. Lett. **86**, 5333, 2001.
- BERKOVITS, R. *Absence of Bimodal Peak Spacing Distribution in the Coulomb Blockade Regime*. Phys. Rev. Lett. **81**, 2128, 1998.

- BERNU, B., L. CÂNDIDO and D. M. CEPERLEY. *Exchange Frequencies in the 2D Wigner Crystal*. Phys. Rev. Lett. **86**, 870, 2001.
- BRODSKY, M., N. B. ZHITENEV, R. C. ASHOORI, L. N. PFEIFFER and K. W. WEST. *Localization in Artificial Disorder: Two coupled Quantum Dots*. Phys. Rev. Lett. **85**, 2356, 2000.
- BRYANT, G. W. *Electronic Structure of Ultrasmall Quantum-Well Boxes*. Phys. Rev. Lett. **59**, 1140, 1987.
- CANALI, C. M. *Disorder and Interaction-Induced Pairing in the Addition Spectra of Quantum Dots*. Phys. Rev. Lett. **84**, 3934, 2000.
- CEPERLEY, D. M. *Path integrals in the theory of condensed helium*. Rev. Mod. Phys. **67**, 279, 1995.
- CEPERLEY, D. M. *Path Integral Monte Carlo Methods for Fermions*. In K. Binder and G. Ciccotti, editors, *Monte Carlo and Molecular Dynamics of Condensed Matter Systems*. Editrice Compositori, Bologna, 1996.
- CHANDLER, D. and P. G. WOLYNES. *Exploiting the isomorphism between quantum theory and classical statistical mechanics of polyatomic fluids*. J. Chem. Phys **74**, 4078, 1981.
- CHUI, S. T. and B. TANATAR. *Impurity Effect on the Two-Dimensional-Electron Fluid-Solid Transition in Zero Field*. Phys. Rev. Lett. **74**, 458, 1995.
- CIORGA, M., A. S. SACHRAJDA, P. HAWRYLAK, C. GOULD, P. ZAWADZKI, S. JULLIAN, Y. FENG and Z. WASILEWSKI. *Addition spectrum of a lateral dot from Coulomb and spin-blockade spectroscopy*. Phys. Rev. B **61**, R16315, 2000.
- COHEN-TANNOUJJI, C., B. DIU and F. LALOË. *Quantum Mechanics*. John Wiley & Sons, 1977.
- CREFFIELD, C. E., W. HÄUSLER, J. H. JEFFERSON and S. SARKAR. *Interacting electrons in polygonal quantum dots*. Phys. Rev. B **59**, 10719, 1999.
- DARWIN, C. G. *The diamagnetism of the free electron*. Proc. Cambridge Philos. Soc. **27**, 86, 1930.
- DE RAEDT, H. and B. DE RAEDT. *Applications of the generalized Trotter formula*. Phys. Rev. A **28**, 3757, 1983.
- DIKOVSKY, M. V. and C. H. MAK. *Analysis of the multilevel blocking approach to the fermion sign problem: Accuracy, errors, and practice*. Phys. Rev. B **63**, 235105, 2001.

- EDMINDSTON, C. and K. RUEDENBERG. *Localized atomic and molecular orbitals*. Rev. Mod. Phys. **35**, 457, 1963.
- EGGER, R., W. HÄUSLER, C. H. MAK and H. GRABERT. *Crossover from Fermi liquid to Wigner molecule behaviour in quantum dots*. Phys. Rev. Lett. **82**, 3320, 1999. **83**, 462(E), 1999.
- FETTER, A. L. and J. D. WALECKA. *Quantum Theory of Many-Particle Systems*. McGraw-Hill, New York, 1971.
- FEYNMAN, R. P. *Statistical Mechanics: A Set of Lectures*. Benjamin/Cummings, Reading, 1972.
- FILINOV, A. V., M. BONITZ and Y. E. LOZOVIK. *Wigner crystallization in mesoscopic 2D electron systems*. Phys. Rev. Lett. **86**, 3851, 2001.
- FLYVBJERG, H. and H. G. PETERSEN. *Error Estimates on Averages of Correlated Data*. J. Chem. Phys **91**, 461, 1989.
- FOCK, V. *Bemerkung zur Quantelung des harmonischen Oszillators im Magnetfeld*. Z. Phys. **47**, 446, 1928.
- FOCK, V. *Näherungsmethode zur Lösung des quantenmechanischen Mehrkörperproblems*. Z. Phys. **61**, 126, 1930.
- FÖPPL, L. *Stabile Anordnungen von Elektronen im Atom*. Journal für die reine und angewandte Mathematik **141**, 251, 1912.
- FOULKES, W. M. C., L. MITAS, R. J. NEEDS and G. RAJAGOPAL. *Quantum Monte Carlo simulations of solids*. Rev. Mod. Phys. **73**, 33, 2001.
- FYE, R. M. *New results on Trotter-like approximations*. Phys. Rev. B **33**, 6271, 1986.
- GAMMON, D. and D. G. STEEL. *Optical studies of single quantum dots*. Physics Today **October**, 2002.
- GOVERNALE, M. *Quantum Dots with Rashba Spin-Orbit Coupling*. Phys. Rev. Lett. **89**, 206802, 2002.
- GRADSTEIN, I. and I. RYSHIK. *Table of Integrals, Series and Products*. Academic Press, New York, 1965.
- HALONEN, V., P. HYVÖNEN, P. PIETILÄNEN and T. CHAKRABORTY. *Effects of scattering centers on the energy spectrum of a quantum dot*. Phys. Rev. B **53**, 6971, 1996.

- HARTING, J., O. MÜLKEN and P. BORRMANN. *The interplay between shell effects and electron correlation in quantum dots*. Phys. Rev. B **62**, 10207, 2000.
- HATANO, N. and M. SUZUKI. *Quantum Monte Carlo and Related Methods*. In M. Suzuki, editor, *Quantum Monte Carlo Methods in Condensed Matter Physics*. World Scientific, Singapore, 1993.
- HÄUSLER, W. *Rotational levels in quantum dots*. Europhys. Lett. **49**, 231, 2000.
- HÄUSLER, W., B. REUSCH, R. EGGER and H. GRABERT. *Crossover from Fermi liquid to Wigner molecule behaviour in quantum dots*. Physica B **284**, 1772, 2000.
- HEINZE, H., P. BORRMANN, H. STAMMERJOHANN and E. HILF. *Temperature measurement from scattering spectra of clusters: theoretical treatment*. Z. Phys. D **40**, 190, 1997.
- HIROSE, K. and N. S. WINGREEN. *Spin-density-functional theory of circular and elliptical quantum dots*. Phys. Rev. B **59**, 4604, 1999.
- HIROSE, K. and N. S. WINGREEN. *Ground-state energy and spin in disordered quantum dots*. Phys. Rev. B **65**, 193305, 2002.
- HIROSE, K., F. ZHOU and N. S. WINGREEN. *Density-functional theory of spin-polarized disordered quantum dots*. Phys. Rev. B **63**, 075301, 2001.
- HIRSCHFELDER, J. O. *Classical and Quantum Mechanical Hypervirial Theorems*. J. Chem. Phys. **33**, 1462, 1960.
- JACAK, L., P. HAWRYLAK and A. WÓJS. *Quantum Dots*. Springer, Heidelberg, 1998.
- JACQUOD, P. and A. D. STONE. *Suppression of Ground-State Magnetization in Finite-Size Systems due to Off-Diagonal Interaction Fluctuations*. Phys. Rev. Lett. **84**, 3938, 2000.
- JANKE, W. *Statistical Analysis of Simulations: Data Correlations and Error Estimation*. In J. Grotendorst, D. Marx and A. Muramatsu, editors, *Quantum Simulation of Complex Many-Body Systems: From Theory to Algorithms*, pp. 423–445. J. von Neumann Institute for Computing, Jülich, 2002. Lecture Notes for the NIC Winter School.
- JIANG, H., H. U. BARANGER and W. YANG. *Spin and Conductance-Peak-Spacing Distributions in Large Quantum Dots: A Density-Functional Theory Study*. Phys. Rev. Lett. **90**, 026806, 2003.

- JONES, A. V. and G. J. PAPADOPOULOS. *On the exact propagator*. J. Phys. A **5**, L86, 1971.
- KASTNER, M. *The single-electron transistor*. Rev. Mod. Phys. **64**, 849, 1992.
- KASTNER, M. *Artificial Atoms*. Physics Today **46**, 24, 1993.
- KOSKINEN, M., M. MANNINEN, B. MOTTELSON and S. M. REIMANN. *Rotational and vibrational spectra of quantum rings*. Phys. Rev. B **63**, 205323, 2001.
- KOSKINEN, M., M. MANNINEN and S. M. REIMANN. *Hund's Rules and Spin Density Waves in Quantum Dots*. Phys. Rev. Lett. **79**, 1389, 1997.
- KOUWENHOVEN, L. P., D. G. AUSTING and S. TARUCHA. *Few-electron quantum dots*. Rep. Prog. Phys. **64**, 701, 2001.
- KOUWENHOVEN, L. P. and L. GLAZMAN. *Revival of the Kondo effect*. Physics World **January**, 22, 2001.
- KUMAR, A., S. E. LAUX and F. STERN. *Electron states in a GaAs quantum dot in a magnetic field*. Phys. Rev. B **42**, 5166, 1990.
- KYRIAKIDIS, J., M. PIORO-LADRIERE, M. CIORGA, A. S. SACHRAJDA and P. HAWRYLAK. *Voltage-tunable singlet-triplet transition in lateral quantum dots*. Phys. Rev. B **66**, 035320, 2002.
- LIPKIN, H. J. *Collective Motion in Many-Particle Systems*. Annals of Physics **9**, 272, 1960.
- LOH JR., E. Y., J. E. GUBERNATIS, R. T. SCALETTAR, S. WHITE, D. SCALAPINO and R. SUGAR. *Sign problem in the numerical simulation of many-electron systems*. Phys. Rev. B **41**, 9301, 1990.
- LORKE, A., R. J. LUYKEN, A. O. GOVOROV, J. P. KOTTHAUS, J. M. GARCIA and P. M. PETROFF. *Spectroscopy of Nanoscopic Semiconductor Rings*. Phys. Rev. Lett **84**, 2223, 2000.
- LOSS, D. and D. P. DIVINCENZO. *Quantum Computation with Quantum Dots*. Phys. Rev. A **57**, 120, 1998.
- LYUBARTSEV, A. P. and P. N. VORONTSOV-VELYAMINOV. *Path-integral Monte Carlo method in quantum statistics for a system of N identical fermions*. Phys. Rev. A **48**, 4075, 1993.
- MACDONALD, A. H., S. E. YANG and M. D. JOHNSON. *Quantum Dots in Strong Magnetic Fields: Stability Criteria for the Maximum Density Droplet*. Aust. J. Phys. **46**, 345, 1993. S.a. cond-mat/9301019.

- MAK, C. H., R. EGGER and H. WEBER-GOTTSCHICK. *Multilevel blocking approach to the fermion sign problem in path-integral Monte Carlo simulations*. Phys. Rev. Lett. **81**, 4533, 1998.
- MARLO, M., M. ALATALO, A. HARJU and R. M. NIEMINEN. *Lateral diatomic two-dimensional artificial molecules: Classical transitions and quantum-mechanical counterparts*. Phys. Rev. B **66**, 155322, 2002.
- MATAGNE, P., J. P. LEBURTON, D. G. AUSTING and S. TARUCHA. *Shell charging and spin-filling sequences in realistic vertical quantum dots*. Phys. Rev. B **65**, 085325, 2002.
- MAYER, A. *On the Morphological Laws of the Configurations formed by Magnets floating vertically and subjected to the Attraction of a superposed Magnet*. Am. Jour. Sci. **16**, 1878.
- MEIRAV, U., P. L. MCEUEN, M. A. KASTNER, E. B. FOXMAN, A. KUMAR and S. J. WIND. *Conductance Oscillations and Transport Spectroscopy of a Quantum Dot*. Z. Phys. B **85**, 357, 1991.
- MERKT, U., J. HUSER and M. WAGNER. *Energy Spectra of two electrons in a harmonic quantum dot*. Phys. Rev. B **43**, 7320, 1991.
- METROPOLIS, N., A. ROSENBLUTH, M. ROSENBLUTH, A. TELLER and E. TELLER. *Equation of State Calculations by Fast Computing Machines*. J. Chem. Phys. **21**, 1087, 1953.
- MIKHAILOV, S. A. *Quantum-dot lithium in zero magnetic field: Electronic properties, thermodynamics and a liquid-solid transition in the ground state*. Phys. Rev. B **65**, 115312, 2002a.
- MIKHAILOV, S. A. *Two ground-state modifications of quantum-dot beryllium*. Phys. Rev. B **66**, 153313, 2002b.
- MÜLLER, H.-M. and S. E. KOONIN. *Phase transitions in quantum dots*. Phys. Rev. B **54**, 14532, 1996.
- NEGELE, J. W. and H. ORLAND. *Quantum Many-Particle Systems*. Addison-Wesley, Redwood City, 1988.
- PEDERIVA, F., C. J. UMRIGAR and E. LIPPARINI. *Diffusion Monte Carlo study of circular quantum dots*. Phys. Rev. B **62**, 8120, 2000.
- PFANNKUCHE, D., V. GUDMUNDSSON and P. A. MAKSYM. *Comparison of a Hartree, Hartree-Fock, and an exact treatment of quantum-dot helium*. Phys. Rev. B **47**, 2244, 1993.

- PRESS, W. H., S. A. TEUKOLSKY, W. T. VETTERLING and B. P. FLANNERY. *Numerical Recipes in FORTRAN*. Cambridge University Press, 1992.
- PRESS, W. H., S. A. TEUKOLSKY, W. T. VETTERLING and B. P. FLANNERY. *Numerical Recipes in FORTRAN 90: The Art of PARALLEL Scientific Computing*. Cambridge University Press, 1996.
- PRIMAS, H. and U. MÜLLER-HEROLD. *Elementare Quantenchemie*. Teubner, Stuttgart, 1990.
- RAIKH, M. E., L. I. GLAZMAN and L. E. ZHUKOV. *Two-Electron State in a Disordered Island: Pairing Caused by the Coulomb Repulsion*. Phys. Rev. Lett. **77**, 1354, 1996.
- RÄSÄNEN, E., H. SAARIKOSKI, M. J. PUSKA and R. M. NIEMINEN. *Wigner molecules in polygonal quantum dots: A density functional study*. Phys. Rev. B **67**, 35326, 2003.
- REIMANN, S. M., M. KOSKINEN and M. MANNINEN. *On the formation of Wigner molecules in small quantum dots*. Phys. Rev. B **62**, 8108, 2000.
- REIMANN, S. M. and M. MANNINEN. *Electronic structure of quantum dots*. Rev. Mod. Phys. **74**, 1283, 2002.
- REUSCH, B. *Diploma thesis*. University of Freiburg, 1998.
- REUSCH, B. and R. BLÜMEL. *Crystallized vortex crystals*. Eur. Phys. J. D **3**, 123, 1998.
- REUSCH, B. and R. EGGER. *Impurity effects in few-electron quantum dots: Incipient Wigner molecule regime*. submitted to Europhys. Lett., s.a. cond-mat/0304625, 2003.
- REUSCH, B. and H. GRABERT. *Unrestricted Hartree-Fock for quantum dots*. to appear in Phys. Rev. B, s.a. cond-mat/0305623, 2003.
- REUSCH, B., W. HÄUSLER and H. GRABERT. *Wigner molecules in quantum dots*. Phys. Rev. B **63**, 113313, 2001.
- RING, P. and P. SCHUCK. *The Nuclear Many-Body Problem*. Springer-Verlag, New York, 1980.
- RÖMER, H. and T. FILK. *Statistische Mechanik*. VCH, Weinheim, 1994.
- RUAN, W. Y., Y. Y. LIU, C. G. BAO and Z. Q. ZHANG. *Origin of magic angular momenta in few-electron quantum dots*. Phys. Rev. B **51**, 7942, 1995.

- SAINT JEAN, M., C. EVEN and C. GUTHMANN. *Macroscopic 2D Wigner islands*. Europhys. Lett. **55**, 45, 2001.
- SCALETAR, R. T. *World-Line QMC*. In M. P. Nightingale and C. J. Umrigar, editors, *Quantum Monte Carlo Methods in Physics and Chemistry*, vol. 525 of *NATO-ASI Series C*, p. 65. Kluwer Academic Publishers, Dordrecht, 1999.
- SLATER, J. C. *Quantum Theory of Atomic Structure*, vol. I. McGraw-Hill, New York, 1960.
- SUNDQVIST, P. A., S. Y. VOLOKOV, Y. E. LOZOVIK and M. WILLANDER. *Phase transitions of a few-electron system in a spherical quantum dot*. Phys. Rev. B **66**, 075335, 2002.
- SZABO, A. and N. S. OSTLUND. *Modern Quantum Chemistry*. McMillan, New York, 1982.
- SZAFRAN, B., S. BEDNAREK and J. ADAMOWSKI. *Magnetic-field-induced transformations of Wigner molecule symmetry in quantum dots*. Phys. Rev. B **67**, 045311, 2003.
- SZE, S. M. *Physics of Semiconductor Devices*. John Wiley & Sons, New York, 2 edn., 1981.
- TANATAR, B. and D. M. CEPERLEY. *Ground state of the two-dimensional electron gas*. Phys. Rev. B **39**, 5005, 1989.
- TARUCHA, S., D. G. AUSTING, T. HONDA, R. J. VAN DER HAGE and L. P. KOUWENHOVEN. *Shell Filling and Spin Effects in a Few Electron Quantum Dot*. Phys. Rev. Lett. **77**, 3613, 1996.
- TAUT, M. *Two electrons in an external oscillator potential: Particular analytic solutions of a Coulomb correlation problem*. Phys. Rev. A **48**, 3561, 1993.
- THOMSON, J. J. *On the Structure of the Atom*. Phil. Mag. VIII p. 237, 1904.
- THOULESS, D. J. *Maximum Metallic Resistance in Thin Wires*. Phys. Rev. Lett. **39**, 1167, 1977.
- VORRATH, T. and R. BLÜMEL. *Thomson-Atome*. Physik in unserer Zeit **31**, 115, 2000.
- WALKER, P. N., Y. GEFEN and G. MONTAMBAUX. *Density Modulations and Addition Spectra of Interacting Electrons in Disordered Quantum Dots*. Phys. Rev. Lett. **82**, 5329, 2003.

- WAN, Y., G. ORTIZ and P. PHILLIPS. *Pair Tunneling in Semiconductor Quantum Dots*. Phys. Rev. Lett. **75**, 2879, 1995.
- WEINMANN, D., W. HÄUSLER and B. KRAMER. *Spin Blockades in Linear and Nonlinear Transport through Quantum Dots*. Phys. Rev. Lett. **74**, 984, 1995.
- WIGNER, E. P. *On the Interaction of Electrons in Metals*. Phys. Rev. **46**, 1002, 1934.
- WIGNER, E. P. *Effects on the Electron Interaction on the Energy Levels of Electrons in Metals*. Trans. Faraday Soc. **34**, 678, 1938.
- YANNOULEAS, C. and U. LANDMAN. *Spontaneous Symmetry Breaking in Single and Molecular Quantum Dots*. Phys. Rev. Lett. **82**, 5325, 1999. **85**, 2220(E), 2000.
- YANNOULEAS, C. and U. LANDMAN. *Collective and Independent-Particle Motion in Two-Electron Artificial Atoms*. Phys. Rev. Lett. **85**, 1726, 2000a.
- YANNOULEAS, C. and U. LANDMAN. *Formation and control of electron molecules in artificial atoms: Impurity and magnetic-field effects*. Phys. Rev. B **61**, 15895, 2000b.
- YANNOULEAS, C. and U. LANDMAN. *Strongly correlated wave functions for artificial atoms and molecules*. J. Phys. Condens. Matter **14**, L591, 2002.
- ZHITENEV, N. B., R. C. ASHOORI, L. N. PFEIFFER and K. W. WEST. *Periodic and Aperiodic Bunching in the Addition Spectra of Quantum Dots*. Phys. Rev. Lett. **79**, 2308, 1997.
- ZHITENEV, N. B., M. BRODSKY, R. C. ASHOORI, L. N. PFEIFFER and K. W. WEST. *Localization-Delocalization Transition in Quantum Dots*. Science **285**, 715, 1999.

Danksagung

Ich danke Herrn Prof. Dr. Reinhold Egger gleichermaßen für seine Schnelligkeit und seine Geduld bei der gemeinsamen Arbeit an einem spannenden Forschungsthema; für die Möglichkeit nach Düsseldorf zu kommen und hier sehr gute Bedingungen und eine angenehme, persönliche Atmosphäre zu erleben.

Ich danke Herrn Prof. Dr. Hermann Grabert für sein Interesse am Unrestricted Hartree-Fock und für die freundliche Aufnahme in seine Freiburger Gruppe, wo der erste Teil dieser Arbeit entstanden ist und ich mich sehr wohl gefühlt habe.

Großer Dank geht an meinen lieben Freund, Kollegen und Mitbewohner Dott. Alessandro De Martino: Unsere WG war ein herrlicher Stützpunkt, um sich zu stärken und Düsseldorf zu erobern, und ist Teil des Erfolges dieser Dissertation.

Ich danke Sascha Hügler, für verlässliche Kameradschaft als Physiker und Kollege und für den Aufbau und die Wartung unserer Computer, insbesondere des Micro Clusters, ohne den die Monte Carlo Rechnungen in diesem Umfang nicht möglich gewesen wären. Ringrazio il Dott. Francesco “Don Ciccio” Siano, per l’amabile ospitalità nel suo ufficio, per l’aiuto sia con il computer che con la fisica e per le molte saggezze del mondo battipagliese ‘translational invariant’. Und ich danke den anderen Mitgliedern unserer sympathischen Arbeitsgruppe: Dr. Chen Shu, unserem Neuzugang Vittorio Peano und Karin Wildhagen, die im Sekretariat kompetente Unterstützung leistete.

Ich danke den Kollegen in Freiburg für die gute Atmosphäre in der Arbeitsgruppe und auf den gemeinsamen Ausflügen: Allen voran meinem Freund und Zimmergenossen und Quantenpunktexperten Christoph Theis, insbesondere fürs Korrekturlesen. Für hilfreiche Diskussionen zu Monte Carlo und MLB danke ich Dr. Lothar Mühlbacher.

Ich freue mich, den Kollegen aus der Experimentalphysik zu danken: Luca Haiberger und Dr. Heiko Ganser, letzterem stellvertretend für die gesamte Trace-Gas Gruppe, wo ich in direkter Nachbarschaft immer Hilfe, einen Tee oder willkommene Ablenkung finden durfte.

Aus der Quantum-Dot Community danke ich für Anregungen und Diskussionen: Thomas Heinzl, Stephanie Reimann, Wolfgang Häusler, Charles Stafford, Andreas Wensauer und Ulrich Rössler, letzteren beiden für eine Einladung zum Seminar nach Regensburg.

Ich danke ganz herzlich meinen Korrekturlesern: Markus Horstjann, Victoria White und meinem alten Freund und Mitstreiter Till Vorrath.

Vier Jahre Doktorarbeit sind eine lange und abwechslungsreiche Zeit mit Durststrecken und vielen neuen Lebenserfahrungen. Ich danke allen Menschen, die mich in dieser Zeit begleitet haben. Ganz besonders danke ich meiner Familie für ihre Unterstützung, guten Zusammenhalt und gemeinsame Lebensfreude.